UNIVERSIDADE FEDERAL DE SANTA CATARINA
CENTRO TECNOLÓGICO
PROGRAMA DE PÓS-GRADUAÇÃO EM ENGENHARIA MECÂNICA

Douglas Fabris

Laser micropatterning of zirconia-based ceramics: effects on microstructure, wettability and mechanical strength

Florianópolis
2023

Douglas Fabris

Laser micropatterning of zirconia-based ceramics: effects on microstructure, wettability and mechanical strength

Tese submetida ao Programa de Pós-Graduação em Engenharia Mecânica da Universidade Federal de Santa Catarina como requisito parcial para a obtenção do título de Doutor em Engenharia Mecânica.

Orientador: Prof. Bruno Henriques, Dr.
Coorientador: Prof. Márcio C. Fredel, Dr.-Ing.
Coorientador: Prof. Andrés F. Lasagni, Dr.-Ing.

Florianópolis
2023

Fabris, Douglas
Laser micropatterning of zirconia-based ceramics: effects on microstructure, wettability and mechanical strength / Douglas Fabris ; orientador, Bruno Alexandre Pacheco de Castro Henriques, coorientador, Márcio Celso Fredel, coorientador, Andrés Fabián Lasagni, 2023.
142 p.

Tese (doutorado) - Universidade Federal de Santa Catarina, Centro Tecnológico, Programa de Pós-Graduação em Engenharia Mecânica, Florianópolis, 2023.

Inclui referências.

1. Engenharia Mecânica. 2. zirconia. 3. zirconia based-nanocomposite. 4. laser texturing. 5. mechanical reliability. I. Henriques, Bruno Alexandre Pacheco de Castro. II. Fredel, Márcio Celso. III. Lasagni, Andrés Fabián IV. Universidade Federal de Santa Catarina. Programa de Pós-Graduação em Engenharia Mecânica. V. Título.

Douglas Fabris

Laser micropatterning of zirconia-based ceramics: effects on microstructure, wettability and mechanical strength

O presente trabalho em nível de Doutorado foi avaliado e aprovado, em 12 de dezembro de 2023, pela banca examinadora composta pelos seguintes membros:

Prof. Milton Pereira, Dr.
Universidade Federal de Santa Catarina

Prof. Laurent Gremillard, Dr.
Institut national des sciences appliquées de Lyon

Prof. Óscar Samuel Novais Carvalho, Dr.
Universidade do Minho

Certificamos que esta é a versão original e final do trabalho de conclusão que foi julgado adequado para obtenção do título de Doutor em Engenharia Mecânica.

ICP-Edu
Documento assinado digitalmente
Henrique Simas
Data: 15/02/2024 17:27:49-0300
CPF: ***.194.639-**
Verifique as assinaturas em https://v.ufsc.br

Coordenação do Programa de Pós-Graduação

ICP-Edu
Documento assinado digitalmente
Bruno Alexandre Pacheco de Castro Henriques
Data: 15/02/2024 09:24:12-0300
CPF: ***.584.754-**
Verifique as assinaturas em https://v.ufsc.br

Prof. Bruno Alexandre Pacheco de Castro Henriques, Dr.
Orientador

Florianópolis, 2023.

À minha esposa Thiara e aos meus pais Elpídio e Margarete.

ACKNOWLEDGMENTS

I would like to express my sincere gratitude to my supervisors, Prof. Dr. Bruno Henriques, Prof. Dr. Márcio C. Fredel and Prof. Dr. Andrés F. Lasagni, for their guidance, support, and encouragement during my research journey and the development of this thesis. Their expertise and insights have been fundamental in shaping my work and have helped me to develop as a researcher.

I would also like to thank my wife, Thiara, for her unwavering love, patience, and support throughout my studies. Her encouragement and understanding have been a constant source of motivation and inspiration.

I am grateful to my parents, Elpídio and Margarete, for their love, support, and encouragement throughout my entire academic journey.

I would like to acknowledge the contributions of my colleagues from both CERMAT and LMO laboratories for their support, encouragement, laughter and supportive environment.

Finally, I would like to express my gratitude to the funding agencies, CAPES and CNPq, for their financial support, which has enabled me to pursue my research goals and aspirations. I would also like to thank the Universidade Federal de Santa Catarina, Technische Universität Dresden and POSMEC for providing me with the opportunity, resources, structure and support to pursue my PhD.

If I had six hours to chop down a tree, I'd spend the first four hours sharpening the axe.

(Abraham Lincoln)

RESUMO

A zircônia estabilizada com 3 mol% de ítria (3Y-TZP) apresenta alta resistência à flexão (> 1000 MPa) e tenacidade à fratura (~5 MPa$\sqrt{m}$), mas sua fragilidade intrínseca a torna vulnerável a falhas catastróficas devido a defeitos como poros e trincas. Para contornar esse problema, nanocompósitos com base em zircônia estabilizada com céria (Ce-TZP) têm sido estudados por apresentarem maior tenacidade. Um exemplo é o compósito Ce-TZP/Al_2O_3/$SrAl_{12}O_{19}$, que pode apresentar uma tenacidade à fratura acima de 10 MPa$\sqrt{m}$ e resistência flexural de >1100 MPa, resultando em um material de alta resistência e confiabilidade, mesmo na presença de defeitos. Além disso, esse nanocompósito é imune ao fenômeno de envelhecimento, que pode prejudicar a performance da zircônia 3Y-TZP. Para aprimorar a interação com tecidos vivos, a superfície do implante pode ser modificada estruturalmente, criando rugosidades controladas para facilitar a aderência e proliferação celular. Entre as técnicas de estruturação, destaca-se o processamento com laser, que permite um controle preciso para otimizar a resposta biológica. Assim, o objetivo desta tese é avaliar a texturização a laser em zircônia 3Y-TZP e no nanocompósito Ce-TZP/Al_2O_3/$SrAl_{12}O_{19}$ e a sua influência na morfologia, microestrutura, comportamento biológico e confiabilidade mecânica do material. Através da técnica convencional de *Direct Laser Writing* com uma fonte de laser picossegundo foi realizado um estudo paramétrico e avaliada a influência da energia do laser (fluência), frequência e velocidade na morfologia da superfície. Neste estudo, foi possível criar texturas no formato de linhas com até 12 µm de largura e 6 µm de profundidade para a 3Y-TZP e 30 µm de largura e 26 µm de profundidade para o nanocompósito. Outra técnica utilizada foi a *Direct Laser Interference Patterning* (DLIP) com lasers de nanossegundo e picossegundo para verificar as diferenças nos danos microestruturais para cada duração de pulso. Utilizando o laser picossegundo, foi possível fabricar um padrão homogêneo sobre toda a amostra de ambos os materiais no formato de linhas com periodicidade de 6 µm, sem defeitos microestruturais significativos. No entanto, a molhabilidade de ambos os materiais diminuiu após a texturização, com o ângulo de contato com água aumentando para ~140° para a zircônia e ~105° para o compósito, não sendo desejável em implantes, visto que a interação celular é aprimorada em superfícies hidrofílicas. Utilizando o laser nanossegundo também foi possível fabricar padrões semelhantes, no entanto foi observado defeitos significativos na microestrutura dos materiais, relacionados à maior energia térmica depositada pelo laser com maior duração de pulso. Por outro lado, o laser nanossegundo melhorou a molhabilidade dos materiais, diminuindo o ângulo de contato para ~50°. Considerando que apresentaram maior número de defeitos, ou seja, o pior cenário em relação à uma diminuição da resistência mecânica, as amostras texturizadas com laser nanossegundo foram submetidas a testes de flexão biaxial. Foi verificada apenas uma diminuição estatisticamente não significativa na resistência da 3Y-TZP, enquanto para o nanocompósito foi observada uma diminuição mais considerável, mas que pode estar relacionada a tensões compressivas no grupo controle. No entanto, ambos os materiais exibiram menor variabilidade na resistência mecânica após a texturização, indicando maior confiabilidade. Testes de ciclagem mecânica e envelhecimento não afetaram a resistência mecânica. Portanto, a partir da correta parametrização do processamento, é possível produzir texturas controladas utilizando tecnologias de fabricação a laser em ambos os cerâmicos 3Y-TZP e Ce-TZP/Al_2O_3/$SrAl_{12}O_{19}$. O processo não compromete significativamente a confiabilidade mecânica dos materiais e, portanto, pode ser uma abordagem promissora para melhorar a interação com tecidos vivos em implantes cerâmicos.

Palavras-chave: Zircônia, nanocompósito a base de zircônia, texturização a laser, confiabilidade mecânica.

RESUMO EXPANDIDO

Introdução

Biomateriais são materiais que podem ser utilizados, de maneira segura, para substituir ou melhorar alguma função biológica, sendo utilizados para fabricar dispositivos que substituam parte de um organismo vivo ou interajam diretamente com o tecido vivo. Alguns exemplos desses dispositivos incluem curativos, agulhas, restaurações dentárias e implantes ortopédicos. Em implantes, o biomaterial, além de ser farmacologicamente aceitável, não sendo tóxico, cancerígeno, alergênico, etc., ele também deve possuir propriedades mecânicas adequadas e resistência à fadiga e ao desgaste. Tradicionalmente, materiais metálicos, especialmente titânio, têm sido utilizados em implantes ortopédicos e dentários. Mas devido a questões estéticas e potencial liberação de íons metálicos no corpo humano por parte dos metais, materiais cerâmicos estruturais, como zircônia e alumina, têm sido estudados como potenciais alternativas. Esses materiais são biocompatíveis e inertes, não causando reações indesejadas por parte do tecido vivo, ao mesmo tempo que apresentam adequada resistência mecânica. Em relação à estética, titânio tem uma cor acinzentada, que pode comprometer a estética de implantes dentários, enquanto a zircônia possui coloração e opacidade próximos ao dente natural.

A zircônia estabilizada com 3 mol% de ítria (3Y-TZP) é atualmente a mais utilizada em implantes devido a suas ótimas propriedades mecânicas, como alta resistência à flexão (~1000 MPa). No entanto, como a maioria das cerâmicas, é um material frágil, com um valor moderado de tenacidade a fratura (4~6 MPa/√m). Portanto, é susceptível à fratura frágil, e defeitos, como trincas e poros, podem reduzir significativamente a sua resistência mecânica. Além disso, a zircônia 3Y-TZP é susceptível ao fenômeno de degradação a baixas temperaturas, que é uma mudança de fase espontânea que ocorre na presença de água e pode prejudicar a sua resistência mecânica e as características da superfície. Por outro lado, estudos têm mostrado que a zircônia estabilizada com céria (Ce-TZP), especialmente na forma de compósito, com fases secundárias e terciárias, podem apresentar altos valores de tenacidade a fratura (15~20 MPa/√m), mantendo a boa resistência a flexão. Além disso, esses materiais são imunes ao envelhecimento, sendo, portanto, uma potencial alternativa para aumentar a confiabilidade mecânica de implantes.

A topografia dos implantes tem grande influência na interação com o meio biológico. Por exemplo, uma microrugosidade cria um efeito de ancoragem mecânica com o osso, melhorando a estabilização primária e ao longo-prazo de implantes. Uma rugosidade controlada pode promover a proliferação celular ou diminuir a adesão de bactérias no implante. Atualmente técnicas como jateamento e ataque ácido são utilizados para gerar topografias mais adequadas em implantes. No entanto, essas técnicas geram texturas aleatórias, sem controle de forma ou de dimensões. Em contraste, técnicas de texturização a laser têm sido estudadas em biomateriais pela sua alta precisão, controle e repetibilidade, permitindo a criação de micro- e nanotopografias com controle sobre o tamanho, geometria e direção das texturas. A texturização a laser remove material localmente por ablação, permitindo a criação de padrões geométricos como linhas, pontos e lamelas.

Entre as técnicas de texturização a laser, a Direct Laser Interference Patterning (DLIP) tem ganhado destaque pela sua capacidade de produzir texturas na escala micrométrica com alta velocidade de processamento. Essa técnica utiliza o fenômeno de interferência da luz ao combinar dois ou mais feixes de laser, criando um padrão de interferência que é transferido para a topografia do material. No entanto, o processo de ablação da texturização a laser gera um aumento de temperatura na vizinhança do material removido, o que pode gerar defeitos como ressolidificação, recristalização, poros e trincas, portanto esta técnica deve ser cuidadosamente estudada. Por outro lado, estes defeitos realçam a necessidade de um biomaterial cuja resistência mecânica seja menos sensível à sua presença, o que é o caso do nanocompósito a base de zircônia estabilizada com céria. Portanto, este trabalho explora o potencial da técnica DLIP para criar texturas na superfície da zircônia tradicional e do novo nanocompósito.

Objetivos

O objetivo desta tese é criar e avaliar texturas micrométricas com alto controle dimensional utilizando tecnologias de texturização a laser na superfície de zircônia e um compósito a base de zircônia estabilizada com ítria, para melhorar a resposta biológica de implantes. Este projeto utiliza a versatilidade das técnicas *Direct Laser Writing* e *Direct Laser Interference Patterning* para produzir texturas nas escalas micro- e submicrométricas buscando minimizar o dano na microestrutura dos materiais testados.

Os objetivos específicos são: fabricar amostras densas de zircônia estabilizada com ítria (3Y-TZP) e do nanocompósito a base de zircônia estabilizada com céria; avaliar o processamento de ambos os materiais e ambas as técnicas de processamento a laser, utilizando diferentes parâmetros, como duração do pulso, fluência e comprimento de onda; otimizar os parâmetros para minimizar danos na microestrutura e obter uma superfície texturizada homogênea; caracterizar as superfícies em termos de topografia, microestrutura, molhabilidade, comportamento biológico e resistência mecânica; e avaliar a influência do envelhecimento e ciclagem mecânica na microestrutura e resistência mecânica das amostras.

Metodologia

Primeiramente, substratos de zircônia estabilizada com 3 mol% de ítria (TZ-3YSB, Tosoh, Ja) e do nanocompósito composto de 84 vol% ZrO_2 (11 mol% CeO_2), 8 vol% de Al_2O_3 e 8 vol% de $SrAl_{12}O_{19}$ (chamado de $ZA_8Sr_8Ce_{11}$) (DOCERAM, Alemanha) foram fabricados a partir da técnica de prensagem e sinterização. Os pós cerâmicos foram prensados uniaxialmente em uma matriz cilíndrica durante 60 segundos em uma pressão de 100 MPa (zircônia) e 70 MPa (compósito) para obter discos compactados. Em seguida, os compactos a verde foram sinterizados a 1500 °C por 2 h (zircônia) e 1450 °C por 1 h (compósito). As dimensões finais dos discos sinterizados foram 16,9 mm de diâmetro e 1,6 mm de espessura. As amostras foram lixadas e polidas para alcançar uma superfície plana e sem riscos/defeitos.

Parte das amostras foram submetidas a um teste paramétrico utilizando a técnica *Direct Laser Writing* para verificar o comportamento de ambos os materiais na interação com o laser. Matrizes de processamento, utilizando diversos valores de fluência, frequência e velocidade de varredura, foram fabricadas para cada material. Para cada condição, um conjunto de linhas foi fabricado por ablação. O sistema de laser consistiu em uma fonte de laser com 10 picossegundos de duração de pulso, no comprimento de onda da luz verde (532 nm) (Edgewave PX200). As regiões texturizadas pelo laser foram analisadas utilizando microscópio eletrônico de varredura (TM-3030, Hitachi) e microscópio confocal (S Neox, Sensofar).

Para a técnica *Direct Interference Patterning* foram utilizados duas diferentes fontes de laser, uma nanossegundo e outra picossegundo. O laser nanossegundo consiste em uma fonte de laser com duração de pulso de 10 ns, frequência de 5 kHz e comprimento de onda de 1064 nm (Edwave InnoSlab – IS400-3-GH). A fonte do laser picossegundo tem uma duração de pulso de 10 ps, frequência de 10 kHz e comprimento de onda de 1064 nm. A configuração ótica de ambos os lasers resultou em uma textura no formato de linhas com periodicidade de 6 μm. Para ambos os lasers, foram realizados testes para alcançar uma textura na superfície homogênea, minimizando defeitos, utilizando diversos valores de fluência, distância entre pulsos e distância entre linhas subsequentes. As superfícies texturizadas por ambos os lasers foram caracterizados por microscopia eletrônica de varredura, microscopia confocal, difratometria de raios X e molhabilidade por ângulo de contato com água. Além disso, as amostras texturizadas com o laser nanossegundo foram submetidas a um teste preliminar biológico e a testes mecânicos. Ensaios de flexão biaxial foram realizados em amostras texturizadas e polidas, antes e após ensaios de ciclagem mecânica e envelhecimento acelerado, para verificar a influência da texturização na resistência mecânica de cada material.

Resultados e discussão

Ambos os materiais foram texturizados com sucesso utilizando a técnica *Direct Laser Writing* com sucesso, mas a morfologia e a geometria das ranhuras formadas foram altamente dependentes dos parâmetros utilizados. Enquanto para níveis baixos de energia (baixa fluência, baixa frequência e/ou alta velocidade) resultou em ranhuras incompletas e pouco profundas, níveis altos de energia (alta fluência, alta frequência e/ou baixa velocidade) resultou em uma camada de ressolidificação encobrindo a região de ablação e a formação de trincas. Comparando ambos os materiais, para um mesmo conjunto de parâmetros, o nanocompósito apresenta uma maior taxa de ablação, com ranhuras mais profundas e largas. Esse fato pode estar ligado às propriedades térmicas, ópticas e eletrônicas de cada materiais, influenciando a interação entre laser e matéria. Para as condições testadas, foi possível alcançar ranhuras de até 30 µm de largura e 26 µm de profundidade para o nanocompósito e 12 µm de largura e 6 µm de profundidade para a zircônia estabilizada com ítria, considerando apenas condições sem a presença de defeitos.

Padrões no formato de linhas com periodicidade de 6 µm foram texturizadas com sucesso utilizando a técnica *Direct Laser Interference Patterning* em ambos os materiais. Através do ajuste dos parâmetros do laser, superfícies relativamente homogêneas foram fabricadas utilizando a fonte de laser nanossegundo. No entanto, devido ao maior tempo de interação entre laser e matéria, uma grande quantidade de defeitos térmicos pôde ser observada na microestrutura de ambos os materiais, incluindo porosidade, trincas e transformação de fases. Por outro lado, o laser picossegundo resultou em uma textura muito mais homogênea, com ausência de defeitos significativos na microestrutura. Em relação à molhabilidade, foi observado um aumento na hidrofobicidade das amostras após a texturização com o laser picossegundo, enquanto o laser nanossegundo diminuiu o ângulo de molhamento com a água. O teste preliminar biológico mostrou que as células se alinham com a direção da textura, ou seja, o laser pode ser usado para guiar o crescimento celular.

Considerando o maior número de defeitos na microestrutura, as amostras texturizadas com o laser nanossegundo foram selecionadas para serem submetidas a ensaios de flexão biaxial, antes e após ensaios de ciclagem mecânica e envelhecimento acelerado. Os resultados mostraram que não houve diminuição significativa na resistência mecânica da zircônia 3Y-TZP após a texturização em comparação com amostras polidas, apresentando inclusive uma diminuição no desvio padrão entre as amostras, o que pode indicar maior confiabilidade. Por outro lado, a texturização diminuiu em aproximadamente 40% a resistência no nanocompósito, a qual pode ser atribuída à defeitos induzidos pelo laser e à uma possível camada com tensões compressivas formada durante o processo de polimento no grupo controle. Apesar de ter sido observada um aumento considerável na quantidade de fase monoclínica na zircônia 3Y-TZP após os ensaios de ciclagem mecânica e envelhecimento acelerado, isso não resultou em uma alteração significativa na resistência mecânica do material. Os ensaios também não alteraram a microestrutura e a resistência mecânica do compósito.

Considerações finais

A texturização a laser é uma potencial alternativa para melhorar a interação entre implantes e tecido vivo através da criação da alteração da sua topografia em implantes baseados em zircônia. Devido às características da tecnologia laser, o tamanho, formato, espaçamento e direção das texturas podem ser facilmente controlados, permitindo a otimização da superfície

para cada tipo de célula e indivíduo. No entanto os parâmetros do laser devem ser corretamente escolhidos para evitar defeitos relacionados ao excesso ou falta de energia, como heterogeneidades, porosidade, trincas e mudança de fase. A técnica *Direct Laser Writing* permitiu maior flexibilidade em relação ao tamanho das ranhuras produzidas através da seleção de parâmetros, o que possibilitaria uma maior variação no tamanho e forma dos padrões texturizados. Através desta técnica também foi possível verificar a maior taxa de remoção de material por ablação do nanocompósito em comparação com a zircônia convencional.

Por outro lado, a técnica *Direct Laser Interference Patterning* permitiu uma maior resolução do padrão de texturização, com periodicidade de apenas 6 µm. Utilizando o laser nanossegundo, uma maior quantidade de defeitos, como poros e trincas, foi observada nos materiais em comparação com o laser picossegundo. No entanto, esses defeitos não causaram mudanças significativas na resistência mecânica da zircônia estabilizada com ítria. Portanto, esse trabalho traz novas percepções da texturização a laser de zircônia e do nanocompósito $\mathrm{ZA_8Sr_8Ce_{11}}$ e dos seus efeitos na microestrutura e confiabilidade mecânica dos materiais. Esses resultados podem contribuir para o desenvolvimento de novos implantes a base de zircônia com melhor interação com tecidos vivos e confiabilidade a longo prazo.

Palavras-chave: Zircônia, nanocompósito a base de zircônia, texturização a laser, confiabilidade mecânica.

ABSTRACT

Zirconia stabilised with 3 mol% yttria (3Y-TZP) has one of the highest flexural strengths (>1000 MPa) and toughness (~5 MPa√m) among ceramic materials. However, its brittleness renders it vulnerable to catastrophic failure in the presence of defects such as pores and cracks. To address this issue, nanocomposites based on ceria-stabilized zirconia (Ce-TZP) have been investigated due their high toughness. One such example is the Ce-TZP/Al_2O_3/$SrAl_{12}O_{19}$ composite, which can achieve a fracture toughness of over 10 MPa√m and flexural strength of >1100 MPa, resulting in a highly resistant and reliable material, even in the presence of intrinsic defects. Moreover, this nanocomposite is immune to the ageing phenomenon, which can impair the performance of 3Y-TZP zirconia. To enhance interaction with living tissues, the implant surface can be structurally modified to create controlled roughness that facilitates cell adhesion and proliferation. Among the structuring techniques, laser processing stands out as it allows precise control to optimize the biological response. Therefore, this thesis aims to evaluate the influence of laser texturing on 3Y-TZP zirconia and the Ce-TZP/Al_2O_3/$SrAl_{12}O_{19}$ nanocomposite on morphology, microstructure, biological behavior, and mechanical reliability of the material using different parameters. By employing the conventional Direct Laser Writing technique with a picosecond laser source, we conducted a parametric study to evaluate the influence of laser energy (fluence), laser frequency, and laser speed on surface morphology. Our study allowed us to create textures in the form of lines up to 12 μm wide and 6 μm deep for 3Y-TZP and 30 μm wide and 26 μm deep for the nanocomposite, provided the processing parameters were appropriate. Furthermore, in this study, Direct Laser Interference Patterning (DLIP) was employed using both nanosecond and picosecond lasers to investigate the differences in microstructural damage for each pulse duration. The picosecond laser produced a homogeneous pattern over the entire sample of both materials in the form of lines with a periodicity of 6 μm, with no significant microstructural defects. However, the wettability of both materials was reduced after texturization, presenting a water contact angle of ~140°(3Y-TZP) e ~105° (composite), which is undesirable for biomedical applications. The nanosecond laser also produced similar patterns, but a greater number of defects were observed in the microstructure and morphology of the materials, which can be attributed to the greater thermal energy deposited by the laser with the longer pulse duration. On the other hand, the nanosecond laser improved the wettability of both materials, decreasing the water contact angle to ~50°. Considering the greater number of defects, which is the worst-case scenario in terms of impairment of mechanical strength, samples texturized with the nanosecond laser were subjected to biaxial bending tests. The strength of 3Y-TZP decreased only slightly and was statistically non-significant, while a more considerable decrease was observed for the nanocomposite, which may be related to compressive stresses in the control group. However, both materials exhibited less variability in mechanical strength, indicating greater reliability. Mechanical cycling and ageing tests did not affect mechanical strength. Therefore, with the correct processing parameterization, it is possible to produce controlled textures using laser manufacturing technologies in both 3Y-TZP and Ce-TZP/Al_2O_3/$SrAl_{12}O_{19}$. The process does not significantly compromise the mechanical reliability of the materials and could therefore be a promising approach to improving interaction with living tissue in ceramic implants.

Keywords: zirconia, zirconia-based nanocomposite, laser texturing, mechanical reliability.

LIST OF FIGURES

LIST OF TABLES

LIST OF ABBREVIATIONS AND ACRONYMS

BFS	Biaxial Flexure Strength
DLIP	Direct Laser Interference Patterning
DLW	Direct Laser Writing
FIB	Focused Ion Beam
HA	Hydroxyapatite
HAZ	Heat-affected zone
LTD	Low-Temperature Degradation
$Nd:YVO_4$	Neodymium-doped Yttrium Orthovanadate
Nd:YGA	Neodymium-Doped Yttrium Aluminum Garnet
SEM	Scanning Electron Microscope
WCA	Water Contact Angle
XRD	X-Ray Diffraction
$ZA_8Sr_8Ce_{11}$	84 vol% ZrO_2 (stabilized with 11 mol% CeO_2), 8 vol% Al_2O_3 and 8 vol% $SrAl_{12}O_{19}$ composite

LIST OF SYMBOLS

λ	Laser wavelength
Λ	Laser pattern periodicity
θ	Half angle between beams
A_p	Spot area
3Y-TZP	3 mol% yttria-stabilized tetragonal zirconia polycrystal
Al_2O_3	Alumina
Ce-TZP	Ceria stabilized tetragonal zirconia polycrystal
CeO_2	Ceria
d	Beam diameter
E_p	Pulse energy
f	Laser repetition rate
F_{acc}	Accumulated fluence
F_p	Pulse fluence
Hd	Hatch distance
Ho	Hatch overlap
Ov	Overlap between pulses
P	Laser power
PtPd	Pulse-to-pulse distance
Ra	Average roughness
s	Scanning speed
Sq	Root mean square height
$SrAl_{12}O_{19}$	Strontium aluminate
Y-TZP	Yttria-stabilized tetragonal zirconia polycrystal
ZrO_2	Zirconia

SUMMARY

1 INTRODUCTION

Metallic materials, especially titanium, have been traditionally used for orthopedic and dental implants. However, structural ceramic materials, such as zirconia (ZrO_2), have gained increasing attention in recent years due to some drawbacks of titanium, such as metal ion release and aesthetic issues (Lorusso *et al.*, 2020; Messous *et al.*, 2021). Titanium, although regarded as the "gold standard" for implant applications, has a greyish color that can compromise the appearance of dental implants, as well as a corrosion potential that can affect the surrounding tissue (Karoussis *et al.*, 2003; Mareci *et al.*, 2016). Zirconia, on the other hand, in addition to its excellent mechanical strength for a ceramic material and biocompatibility, it also has a coloration and opacity that resemble natural teeth (Stadlinger *et al.*, 2010). Zirconia exhibits a phase transformation that enhances its fracture toughness by increasing the energy required for crack propagation. A tetragonal metastable phase is transformed into monoclinic when a critical stress is applied, which is accompanied by a volume change and generates compressive stresses that slow the crack propagation. This mechanism, which depends only on the presence of a metastable tetragonal phase, enabled by the addition of a phase-stabilizing dopant, significantly improves its mechanical properties, earning it the label of "ceramic steel" (Garvie; Hannink; Pascoe, 1975).

Yttria-stabilized zirconia (Y-TZP) is the most common type of zirconia used in implants nowadays, as it exhibits good mechanical properties, such as a high flexural strength value (~1000 MPa). At room temperature, it is formed almost completely by submicrometric metastable tetragonal grains. However, it still is a brittle material, with only a moderate fracture toughness value (4-6 MPa/√m). This implies that the material is susceptible to brittle fracture, and defects such as cracks and pores can significantly reduce its mechanical strength and cause premature failure. Moreover, brittle materials have a large variation in mechanical strength values due to the presence of intrinsic flaws in the material, so statistical tools are required to properly evaluate their failure probability. On the other hand, recent studies have demonstrated that ceria-stabilized zirconia (Ce-TZP) and its composites can achieve a high fracture toughness value (15-20 MPa/√m), and even exhibit some plastic behavior (Chevalier *et al.*, 2020). Therefore, this material can be more reliable in terms of mechanical strength values and more suitable for applications where flaws are inevitable. Furthermore, ceria-stabilized zirconia is more resistant to the phenomenon of low-temperature degradation (LTD), which can occur with zirconia in the presence of water and impair its surface characteristics and mechanical properties.

Surface topography modifications of both metallic and ceramic implants have been investigated in the last few decades to enhance their osseointegration and long-term performance. Studies indicate that increasing implant surface roughness can improve primary and long-term stabilization due to a mechanical interlocking effect with the bone (Buser *et al.*, 1991). Controlled roughness can also promote cell proliferation and protein synthesis, as well as reduce bacterial adhesion around the implant (Cunha *et al.*, 2016; Groessner-Schreiber; Tuanf, 1992). Various techniques are employed to generate roughness on the surface of implants, such as sandblasting, acid etching, and anodizing (Le Guéhennec *et al.*, 2007). However, these techniques only create random structures with poor dimensional control. In contrast, laser texturing techniques have been studied and applied to biomaterials due to their capability of producing micro- and nano-topographies with control over the size and orientation of the texture patterns. Laser texturing consists of removing layers of material through laser ablation with micrometric precision and almost perfect repeatability, creating controlled patterns, such as dimples and grooves. Laser-textured implants can have an enhanced biological and mechanical adaptation to human tissue (Palmquist *et al.*, 2010).

Among the laser techniques, Direct Laser Interference Patterning (DLIP) is a prominent texturing method that offers high resolution and processing speed. DLIP takes advantage of the light interferometry phenomenon by superposing two or more laser beams, creating an interference region with a pattern of energy that varies periodically. Where the energy is high, the material is ablated, and where the energy is low, the material is left intact. This technique can potentially enhance the performance of implants by improving their primary stabilization and reducing their rejection rates, thereby extending their durability and patient comfort. However, it is important to acknowledge that any texturing technique (such as sandblasting, acid etching, laser, etc.) can introduce defects on the surface of the material, which can compromise its mechanical properties. This underscores the need for developing ceramic materials that are more resistant to flaws.

DLIP has been successfully applied in a wide range of materials, especially metals and polymers. However, bioceramics have received limited attention in the literature regarding the application of DLIP patterning, as indicated by a short review conducted by the author (Fabris *et al.*, 2019). Therefore, this study aims to fill this gap by investigating the effect of laser texturing on the microstructure, wettability, biological behavior, and mechanical strength of zirconia using different laser parameters. Moreover, this research explores the potential of DLIP to create micropatterns on Ce-TZP composites, which has not been reported before.

1.1 OBJECTIVES

This work aims to create novel surfaces with micrometric textures on zirconia, both yttria-stabilized and ceria-stabilized, for enhancing the biological response of implants. The project utilizes the versatility of Direct Laser Writing and Direct Laser Interference Patterning laser technologies to produce micro- and nanoscale textures on zirconia surfaces with minimal damage. The specific objectives of this project are to:

- Fabricate non-porous samples of dental-grade zirconia (3Y-TZP) and a novel ceria-stabilized zirconia-based nanocomposite by the processing method of pressing and sintering.
- Evaluate the laser processing of both materials using the conventional Direct Laser Writing technique and the Direct Laser Interference Patterning with different laser parameters, such as fluence, pulse duration, and wavelength.
- Optimize the laser parameters to obtain homogeneous and defect-free textured surfaces.
- Characterize the textured samples in terms of topography, microstructure, wettability, biological behavior, and mechanical strength.
- Assess the effect of accelerated aging and mechanical cycling on the microstructure and the mechanical strength of the textured samples.

1.2 THESIS STRUCTURE

The present work is organized as a compilation of research articles that are planned to be published. Before the articles, two chapters are included: Chapter 1 (current), which introduces the problem and the objectives of this thesis, and Chapter 2, which provides some fundamentals of biomaterials and laser texturing theory and a literature review. The four research chapters are as follows:

- Chapter 3 – a parametric study of Direct Laser Writing with varying values of fluence, scan speed, and repetition rate using a picosecond 532 nm laser source to assess the effect of each parameter on the ablation of 3Y-TZP and Ce-TZP/Al_2O_3/$SrAl_{12}O_{19}$ nanocomposite.
- Chapter 4 – an analysis of the influence of Direct Laser Interference Patterning with a nanosecond 1064 nm laser source using different laser parameters on

the microstructure, wettability, and biological behavior of 3Y-TZP and Ce-TZP/Al_2O_3/$SrAl_{12}O_{19}$ nanocomposite.

- Chapter 5 – an analysis of the influence of Direct Laser Interference Patterning with a picosecond 1064 nm laser source using different laser parameters on the microstructure and wettability of 3Y-TZP and Ce-TZP/Al_2O_3/$SrAl_{12}O_{19}$ nanocomposite.
- Chapter 6 – an evaluation of the influence of laser patterning, accelerated aging, and mechanical cycling on the mechanical behavior of both materials, correlating with the microstructural changes.

Each research chapter is presented as a self-contained paper, which includes the research problem, a brief literature review and the literature gap it addresses, its objectives, methodology, results, discussion, and conclusions. The final chapter (Chapter 7) summarizes the general conclusions and suggests future directions based on the findings of the four research papers. The references are listed together at the end of this document.

2 LITERATURE REVIEW

2.1 BIOMATERIALS

According to Park and Lakes (Park; Lakes, 2007), biomaterials are materials that can be safely, reliably, economically, and physiologically integrated into living systems for the purpose of replacing or enhancing a biological function. These materials can be used to fabricate devices that either substitute a part of a living organism or interact directly with living tissue. Examples of such devices include sutures, needles, dental restorations, orthopedic implants, and so on. This work will focus on the application of biomaterials as implants, which are biomedical devices that aim to replace or reinforce a bone, joint, or tooth.

Living tissues are complex and delicate environments that impose several requirements on biomaterials that come into contact with them. The biomaterial should be chemically inert and stable, avoiding corrosion or ion release into the body. It should also be pharmacologically acceptable, exhibiting no toxicity, allergy, immunogenicity, or carcinogenicity. Moreover, it should have adequate mechanical properties for its intended use and good resistance to fatigue and wear. Other factors such as topological features, design, and weight can also affect the clinical success of an implant (Smith, 1993). For example, in hip implants, there are essentially four factors that lead to their failure: infection, wear, fracture, and loosening, which are directly related to the characteristics of the biomaterial, as shown in Figure 2.1. It can be observed that biological compatibility is more critical in the short term due to the infection risk, while mechanical factors are the main cause of long-term failure.

Figure 2.1 - Probability of failure for different causes versus implant period for hip joint replacements

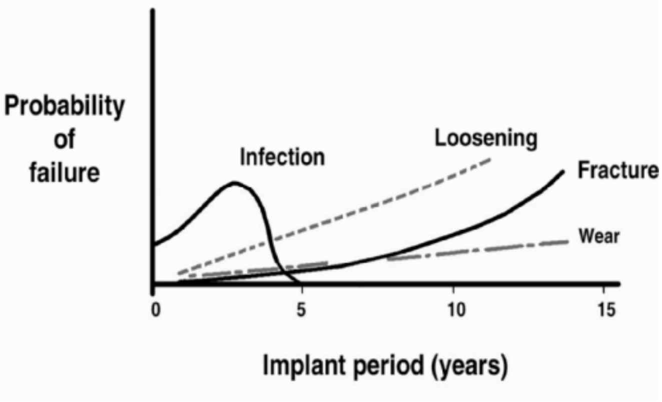

Source: Adapted from (Park; Lakes, 2007).

Metallic materials have been widely used for implant applications due to their biocompatibility and mechanical strength. However, corrosion of metallic implants can result in the release of harmful ions that trigger inflammatory responses and compromise implant stability and tissue integrity (Staiger *et al.*, 2006). Among the metallic materials, stainless steel alloys, especially the austenitic 316 and 316L grades, are commonly employed because of their low cost and tunable properties through different processing methods. Nevertheless, stainless steel alloys are prone to corrosion under certain conditions, such as low oxygen levels and high-stress concentrations, and are therefore only suitable for temporary implants, such as plates and screws (Park; Lakes, 2007).

Biomedical applications have benefited from the use of titanium alloys as an alternative to steel. Titanium is a widely used material for both dental and orthopedic implants, due to its superior mechanical properties and biocompatibility. The formation of a passive titania (TiO_2) layer on the surface of titanium protects it from corrosion and prevents the release of harmful ions into the human body. Titanium-based implants can be fabricated from commercially pure titanium or one of its alloys, such as titanium-aluminum-vanadium (Ti-6Al-4V). This alloy exhibits excellent mechanical performance and allows the production of components with thinner sections and lower weight. Titanium also has a lower density than steel. Titanium is still regarded as the gold standard for dental implants, with more than 10 years of follow-up studies (Karoussis *et al.*, 2003). However, the grayish color of this material can compromise the aesthetics of the dental crown, as it may be visible through the translucent material. Moreover, there are some concerns about the long-term effects of this material, especially the release of aluminum and vanadium into the body, which has been linked to diseases such as Alzheimer’s and some neuropathies (Banerjee; Nag; Fraser, 2005).

The biomedical field has also greatly benefited from the use of polymeric materials. Initially, they were employed as suture materials, but their ease of fabrication and shape versatility have allowed them to find various biomedical applications, such as catheters, stents, and implants (Griffith, 2000; Park; Lakes, 2007). Some polymers have structures that resemble natural tissue components, such as collagen, and can even facilitate tissue integration with the biomaterial. Ultra-high molecular weight polyethylene (UHMWPE) is one of the polymers used in implants, as it possesses good mechanical properties and is suitable for applications that involve sliding between surfaces, such as hip and knee implants. Another polymer that has attracted attention as a material with interesting properties is polyether ether ketone (PEEK), which exhibits high mechanical, wear, and fatigue resistance, biocompatibility, high toughness, and easy processing (Hallmann *et al.*, 2012; Henriques *et al.*, 2018a, 2019).

Ceramic materials, especially zirconia and alumina, have attracted the attention of researchers for implant applications, due to their excellent biocompatibility and low friction wear. Alumina exhibits good mechanical strength, reasonable fracture toughness, and high corrosion and wear resistance. However, its *in vivo* performance is limited by slow crack growth which leads to a high failure rate (De Aza *et al.*, 2002). Zirconia, on the other hand, is a promising alternative for ceramic implants, as it possesses good mechanical strength and outstanding fracture toughness (higher than any other monolithic ceramic) in its tetragonal form, as well as corrosion and wear resistance and greater affinity to bone tissue than most other bioceramics (Bona; Pecho; Alessandretti, 2015; De Aza *et al.*, 2002; Zhang, 2012). Zirconia implants have shown similar biocompatibility and osseointegration results as titanium implants in *in vitro* and *in vivo* studies (Depprich *et al.*, 2008; Gahlert *et al.*, 2012). Moreover, zirconia has a white color that mimics the natural appearance of teeth, which makes it suitable for dental implants, where aesthetic is also important, unlike titanium, which has a grayish color (Stadlinger *et al.*, 2010). Zirconia also has low bacterial colonization, which reduces the risk of infections and improves integration with soft tissues (Nascimento *et al.*, 2014).

The phase transformation of zirconia during crack propagation is responsible for its high fracture toughness. Zirconia can exist in three different crystalline phases: monoclinic (M), cubic (C), and tetragonal (T). Pure zirconia is monoclinic at room temperature and transforms to tetragonal at 1170 °C and to cubic at 2370 °C. The transformation tetragonal ↔ monoclinic (T ↔ M) is martensitic and accompanied by a volume change of ~4%, which can lead to catastrophic failure of undoped zirconia upon cooling. However, the addition of certain oxides, such as CaO, MgO, CeO_2, and Y_2O_3, can retain the T and C phases at room temperature. The T phase at room temperature is metastable and undergoes a mechanical stress-induced transformation to the M phase, which has a larger volume. This volume expansion of constrained grains induces a compressive stress field at the crack tip, which inhibits crack propagation and enhances the fracture toughness of zirconia (Garvie; Hannink; Pascoe, 1975; Piconi; Maccauro, 1999). This mechanism, called “transformation toughening”, is responsible for the favorable mechanical properties of zirconia. Figure 2.2 shows the phase change induced by a crack.

Figure 2.2 - Crack growth inducing the tetragonal to monoclinic phase transformation. This change generates volume increase (red arrow) and compressive stresses (blue arrow) that slow crack propagation.

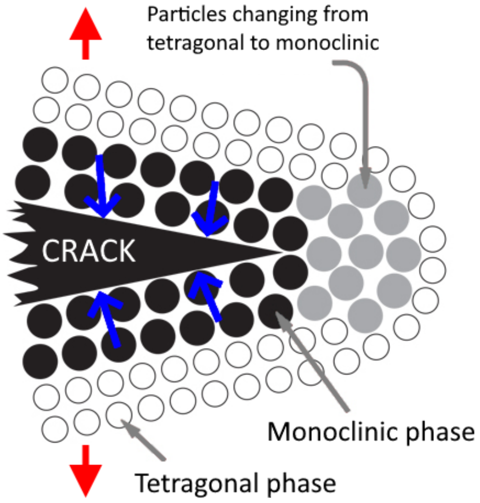

Source: Adapted from (Ćorić; Majić Renjo; Ćurković, 2017).

Yttria-stabilized tetragonal zirconia polycrystal (Y-TZP) is a widely used zirconia material for implants, owing to its excellent mechanical and tribological properties. It consists of submicrometric grains of tetragonal zirconia phase that are stabilized by yttria (Y_2O_3) doping, which enhances its fracture toughness (4-6 MPa/√m) and flexural strength (>1000 MPa). Y-TZP has been employed in the fabrication of the femoral head of hip implants, as it exhibits low friction and wear rates compared to other metallic and ceramic materials, due to its fine-grained and low-porosity microstructure (Park; Lakes, 2007). The addition of Y_2O_3 gives origin to oxygen vacancies by charge compensation, introducing also crystal distortions that stabilize the tetragonal phase. Y-TZP can be obtained with low concentrations of Y_2O_3 (typically 2~3% mol%), as illustrated in the ZrO_2-Y_2O_3 phase diagram in Figure 2.3. At the sintering temperature (~1500 °C) of 3Y-TZP (3 mol% of yttria), the sample consists mostly of a tetragonal phase, with a small amount of cubic phase. Upon cooling, the diffusion rate of yttrium ions is too slow to allow any phase transformation under typical cooling conditions, resulting in a metastable tetragonal phase at room temperature. A more detailed discussion on the stabilization and transformation kinetics of the tetragonal phase can be found in (Chevalier *et al.*, 2009). Other yttria-stabilized zirconia compositions, such as Y_2O_3 8 mol%, which produce a mixture of cubic and metastable tetragonal phases with different properties, have been used for various applications such as electrolytes and thermal barrier coatings. Nevertheless, 3Y-TZP offers the best balance between the strength and toughness of any stabilized zirconia.

Figure 2.3 - ZrO_2-Y_2O_3 metastable phase diagram.

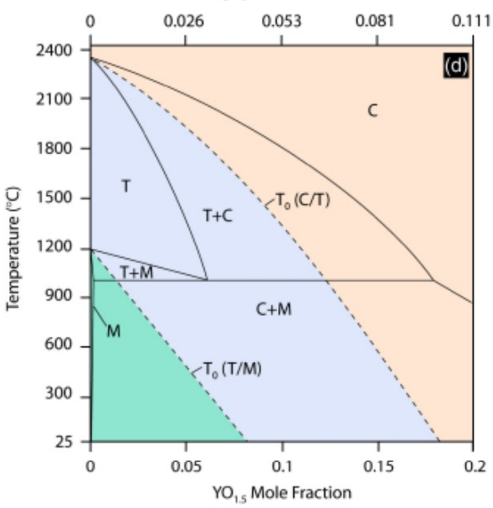

Source: (Chevalier *et al.*, 2009)

However, zirconia is prone to aging in the presence of water, due to the metastability of the tetragonal phase (Lawson, 1995). This phenomenon, known as low-temperature degradation (LTD), involves the transformation of the metastable tetragonal phase to the monoclinic phase in the presence of water molecules, even at room temperature. Aging can result in surface roughness, micro-cracking, and grain pulling, which compromise the integrity of the material (Chevalier; Cales; Drouin, 1999). The aging process typically starts at the surface exposed to water molecules and propagates towards the interior of the material. Although not completely understood, the prevailing explanation of LTD is that water, in the form of OH^- ions, diffuses into the zirconia and occupies the oxygen vacancies. When the oxygen vacancy concentration is reduced below a critical level, the tetragonal phase becomes unstable and transforms into the monoclinic phase (Chevalier *et al.*, 2009). Y-TZP is more prone to LTD due to its higher number of vacancies caused by the trivalent character of Y_2O_3, which results in a higher diffusion rate of water molecules than other zirconia-based ceramics (e.g., CeO_2 stabilized ZrO_2) (Chevalier; Gremillard; Deville, 2007). In addition to the chemical composition, surface roughness and porosity also play an important role in LTD resistance. Porous and rough surfaces have a higher susceptibility to aging than polished ones due to the larger surface area in contact with water. Furthermore, open porosity can transport water to the bulk of the material (Chevalier *et al.*, 2011). Aging is typically characterized using X-ray diffractometry (XRD), which allows to detect and quantify the phases present in the sample.

The phase transformation caused by the aging phenomenon usually has two consequences: surface roughening and microcracking. The former can impact the wear performance where a smooth surface is needed, such as in hip joint heads. Surface roughening increases the friction and wear rate between contacting parts, resulting in the detachment of zirconia grains, which can cause inflammatory reactions in the body and implant loosening (Chevalier; Gremillard; Deville, 2007). Microcracking can generate high-stress concentrations at the crack tips and potentially lead to catastrophic failure. Furthermore, zirconia is susceptible to slow crack growth, which is a stress-assisted corrosion process in the presence of water at the crack tip. The interaction between water and ceramic can break interatomic bonds and, in combination with an applied stress, cause a gradual and continuous crack propagation, which can lead to rupture when the crack reaches a critical size (Chevalier; Olagnon; Fantozzi, 1999). Although a series of failures of zirconia femoral heads in the 2000s due to an accelerated t→m transformation has negatively impacted the application of zirconia in orthopedics, some studies reported good clinical outcomes and low wear rate associated with zirconia implants (Chevalier; Gremillard; Deville, 2007; Wroblewski *et al.*, 2004). Despite the uncertainties about the impact of LTD on the long-term performance of Y-TZP implants, current research is exploring alternative zirconia-based materials to ensure the microstructural stability in contact with body fluids.

Despite the increased toughness due to phase transformation, stabilized zirconia (including Y-TZP) still fractures at low deformations in the presence of defects or cracks due to its brittle behavior. This causes a large variation in the mechanical strength values of the material, which requires statistical tools such as Weibull analysis to describe its mechanical behavior. Ceramics and composites based on ceria-stabilized zirconia (Ce-TZP) have demonstrated a certain plastic behavior due to the phase transformation mechanism, which results in low variation of mechanical strength values and, consequently, higher reliability (Palmero *et al.*, 2015; Reveron *et al.*, 2017).

Ceria-stabilized zirconia (Ce-TZP) consists of metastable tetragonal grains doped with typically 10-12 mol% of CeO_2. Compared to Y-TZP, it has a lower critical transformation stress and a larger transformation zone around a crack, resulting in an outstanding toughness of about 15-20 MPa/√m. However, Ce-TZP has a lower flexural strength (< 600 MPa) as a result of the larger grain size after sintering (1.5-2.0 µm) in contrast to the nanometric grains of Y-TZP (Chevalier *et al.*, 2020). Ce-TZP also exhibits a transformation-induced plasticity, which means that it can behave as a “ductile” ceramic under certain conditions (Grathwohl; Liu, 1991; Rauchs *et al.*, 2001). Figure 2.4 illustrates this behavior, showing the stress-strain diagram of Ce-TZP samples sintered under different conditions. Therefore, Ce-TZP has a high flaw tolerance and a lower scatter in the strength values. These properties make Ce-TZP a suitable candidate for biomedical applications, especially when there are intrinsic flaws due to the fabrication process.

Figure 2.4 - The mechanical behavior of ceria-stabilized zirconia for different sintering cycles, compared with an ideal plastic behavior.

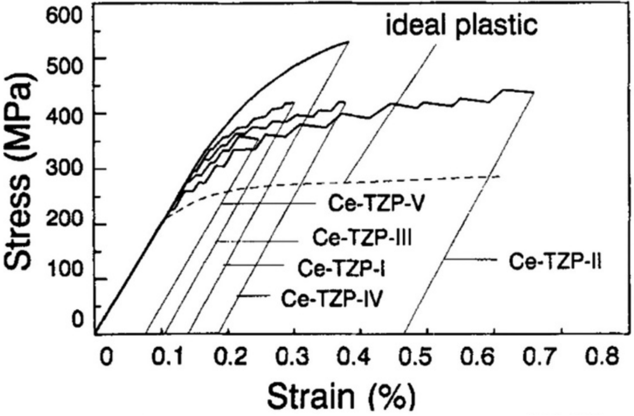

Source: Adapted from (Grathwohl; Liu, 1991).

Ce-TZP also has a higher stability in the presence of water, minimizing the aging phenomenon (Chevalier *et al.*, 2009). The tetragonal zirconia is stabilized with the tetravalent Ce^{4+} ion, which leaves no oxygen vacancies in the crystal structure, which is the prevailing cause of LTD in Y-TZP. When the CeO_2 content is above 12 mol%, the ceramic presents negligible phase transformation, as shown in Figure 2.5, in contrast to more than 60% of monoclinic content observed in Y-TZP after 150h at 150°C in water vapor (Lughi; Sergo, 2010). Despite some disadvantages, such as the yellowish color that limits its aesthetic appeal for dental applications, Ce-TZP has a great balance between strength, toughness, and resistance to LTD, and a further improvement of its properties is a major area of interest.

Figure 2.5 - Monoclinic fraction as function of aging time for Y-TZP and Ce-TZP.

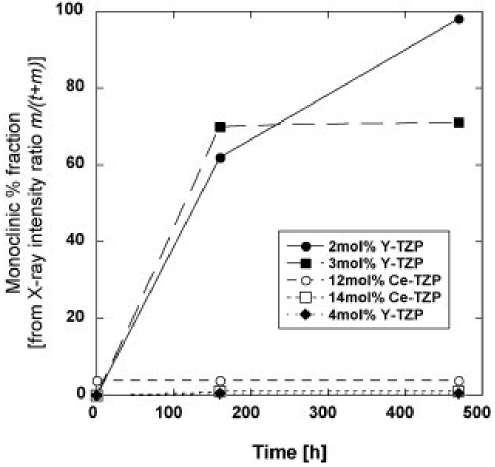

Source: (Lughi; Sergo, 2010).

Nanocomposites based on Ce-TZP have been developed to enhance the mechanical strength to a level comparable to Y-TZP. Adding an immiscible second phase can pin the grain boundaries and control the grain growth of zirconia, which is the main limitation of Ce-TZP. For instance, adding 30 vol% of alumina can reduce the zirconia grain size to ~0.60 µm and increase the flexural strength to ~1400 MPa (Ban *et al.*, 2008). The addition of elongated third phases (such as $SrAl_{12}O_{19}$) can also inhibit grain growth and further improve toughness by crack-bridging and deflection. However, refining the microstructure also decreases the transformability under stress and, consequently, the toughness. Therefore, the amount of ceria should be tailored to achieve the optimal balance between toughness and strength. Recently, the nanocomposite Ce-TZP/$SrAl_{12}O_{19}$/Al_2O_3 has been developed, showing excellent mechanical properties and resistance to LTD (Palmero *et al.*, 2015; Reveron *et al.*, 2017). The strontium aluminate, in addition to the crack-bridging mechanism mentioned above, also induces tensile stresses in the matrix, which facilitate the t → m transformation and maintain the high fracture toughness value. Doping the zirconia phase of this composite with 10.5 mol% of ceria can result in a bending strength of up to 1.1 GPa and a fracture toughness of >10 MPa√m. This composite also exhibited transformation-induced plasticity and almost no dispersion in strength data. Increasing the ceria content to >11 mol% can result in typical brittle behavior, decreasing the biaxial strength to ~800 MPa and the fracture toughness to ~9 MPa√m (Reveron *et al.*, 2017). The relation between ceria content and mechanical properties of the composite is shown in Figure 2.6. With such high toughness, the strength of this composite is not significantly affected by even large processing defects (~100 µm) and exhibits a high Weibull modulus up to ~30 in flexural test, in contrast to a value of 12 found in 3Y-TZP

(Chevalier *et al.*, 2020). Therefore, this nanocomposite has great potential for biomedical applications, as it combines high mechanical strength and high fracture toughness.

Figure 2.6 - Biaxial strength and fracture toughness of the Ce-TZP/$SrAl_{12}O_{19}$/Al_2O_3 composite for different values of ceria.

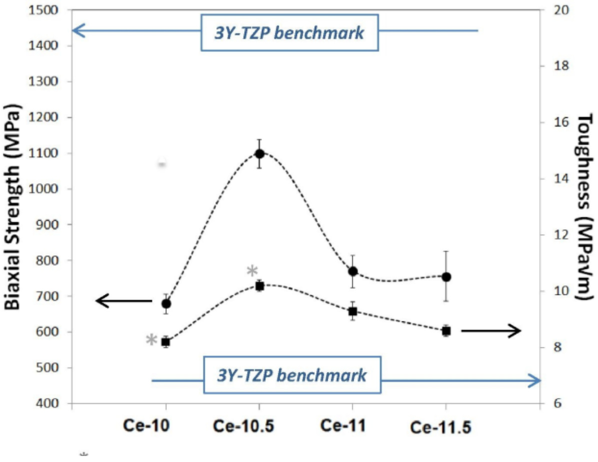

Source: Adapted from (Reveron *et al.*, 2017).

The biological behavior and performance of implants are greatly influenced by their surface topography, in addition to their chemical composition. Increasing the roughness of the biomaterial surface can enhance the primary and long-term stability, due to a mechanical interlocking effect with the bone (Buser *et al.*, 1991). Moreover, controlled roughness can promote cell proliferation and improve protein synthesis on implants, compared to a smooth surface (Groessner-Schreiber; Tuanf, 1992). Implant technology has aimed to modify the bioinert surface of zirconia to a bioactive one, which is favorable for adequate cell proliferation and attachment, facilitating the integration of the bone implant (Pardun *et al.*, 2015; Yin *et al.*, 2017). Therefore, various physical and chemical methods have been applied to improve the properties of the zirconia surface, such as acid etching, sandblasting, laser treatment, coating, and modifying the zirconia into a material with a functional gradient of properties to enhance its bioactivity and biological and mechanical compatibility with the host tissues (Moura *et al.*, 2017).

2.2 INTERACTION BETWEEN IMPLANT AND BONE

Before discussing the interactions between bone and implant, we will briefly introduce the biological structures and processes involved in implantation, starting with bone. Figure 2.7 shows the structure of bone, which is a material composed of organic and inorganic components. The organic components are mainly collagen fibers, which are composed of tropocollagen and provide bone with some toughness. The inorganic components are mainly hydroxyapatite crystals, which contain calcium and phosphorus, as well as some other elements, such as sodium, potassium, and magnesium, and are responsible for the rigidity of bone (Gao *et al.*, 2017). Bone can be classified into cortical bone and trabecular bone, based on its structure. Cortical bone is located on the surface of the bone and contains most of the calcium and phosphate in the human body. It has a high density (5%-10% porosity) and relatively high mechanical strength (Nguyen *et al.*, 2012). The trabecular bone is located in the center of the bone and consists of lamellae of trabeculae, where adipose tissue, blood vessels, and bone marrow are present. Trabecular bone has a spongy shape, with a high porosity (50%-90%) and a large surface area (up to 20 times larger than that of cortical bone) (McKittrick *et al.*, 2010). However, the structure and composition of bone can vary depending on the location of the bone and the age, genetics, and lifestyle of the patient, which implies different requirements for implants. Therefore, developing biomaterials with optimal properties for bone implants is still a major challenge.

Figure 2.7 - Multi-scale structure of the bone and its chemical composition.

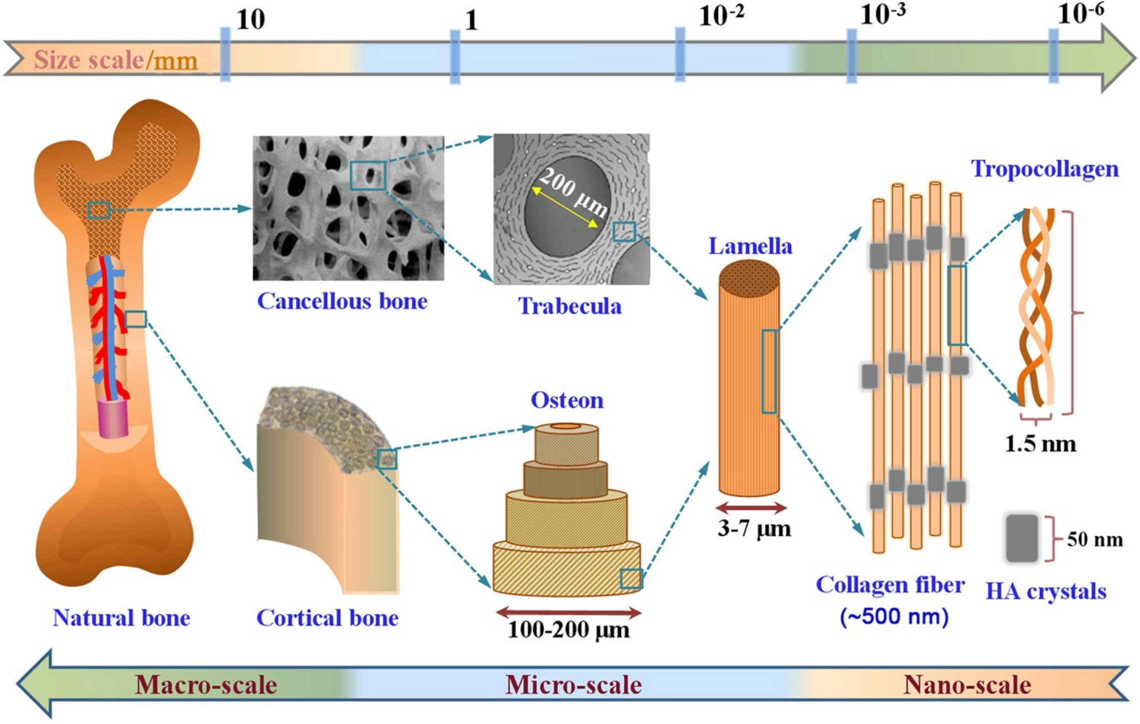

Source: (Gao *et al.*, 2017).

Bone growth around an implant is dependent on three phenomena that occur in the bone: osteoinduction, osteoconduction, and osseointegration. Osteoinduction is the process of inducing osteogenesis, which is the formation of new bone from primitive, undifferentiated, and pluripotent cells that are stimulated to develop into prosteoblasts, which then generate differentiated bone cells (osteoblasts and osteocytes) (Albrektsson; Johansson, 2001). This process is initiated soon after a fracture or an implant insertion, through the release of an inducing glycoprotein, and is the main factor responsible for the formation of new bone. Osteoinduction can also be stimulated by physical factors, such as electrical signals and tension applied to the bone (Dealler, 1981). Osteoconduction is the process of bone growth on the surface of the implant, which is influenced by the differentiated cells derived from osteoinduction. This process is also related to the biomaterial used in the implant, as some materials, such as copper and silver, do not support osteoconduction, while others, such as titanium and zirconia, have high biocompatibility and promote osteoconduction (Albrektsson; Johansson, 2001).

The process of osseointegration, which is a direct and functional connection between the bone tissue and the implant that requires fracture to separate, was first described by Brånemark et al. (Brånemark *et al.*, 1969). This phenomenon is dependent on adequate osteoinduction and osteoconduction. The process of osseointegration can be compared to the healing of bone fractures, as they both involve immune response, angiogenesis, and progenitor cell recruitment. However, when an implant is inserted, the adjacent tissue faces a situation that is not prepared for, considering the evolutionary and adaptive processes of biological systems. Unlike fractures, the implant occupies the entire region where the bone is removed, reducing the gap between the fractured bone surfaces and contributing to the primary stability between bone and implant (Shah; Thomsen; Palmquist, 2019). However, the insertion of a foreign body also triggers cellular reactions that are often unpredictable and related to the surface properties of the implant. The process of implant adaptation and osseointegration has been extensively studied and discussed in recent decades, but its mechanism is still not fully elucidated, as detailed in (Shah; Thomsen; Palmquist, 2019).

Osseointegration occurs at two levels: primary and secondary. Primary osseointegration, or primary stability, refers to the mechanical bond between the implant and the adjacent bone tissue right after implantation. It can be defined as the absence of implant mobility, and it is directly related to its success rate, as even small micromovements can adversely affect the osseointegration process (Javed; Romanos, 2010). Secondary osseointegration, or secondary stability, relates to bone regeneration and remodeling after implantation, and it is directly influenced by primary stability (Swami; Vijayaraghavan; Swami, 2016).

Various methods, mainly involving modifications of the implant surface, have been investigated to improve its osseointegration rate, as mentioned earlier. The use of bioactive materials, either as the implant material itself or as a coating, enhances the biological response of the body and accelerates bone growth. Some examples of bioactive materials are hydroxyapatite and bioactive glass, which have calcium phosphate in their composition and form a chemical bond with the bone surface (Elias; Meirelles, 2010). In contrast, bioinert materials form a fibrous capsule around the implant and have minimal chemical interaction with adjacent tissues. Another important factor that has been shown to influence the osseointegration process is the topography of the implant. Cells respond differently depending on whether the implant has a smooth or rough surface. Fibroblasts and epithelial cells adhere better to smooth surfaces, while osteoblast proliferation and collagen synthesis are higher on rough surfaces (Boyan *et al.*, 2001). It is generally accepted that a certain roughness is beneficial for the osseointegration process, but there is no consensus on the optimal standard for roughness in the literature (Elias; Meirelles, 2010).

The possibility of surface contamination by bacteria, which can lead to infection and implant removal, is another important aspect of the implantation process, in addition to osseointegration. Bacteria form a type of colony on the implant surface called a biofilm, where the microorganisms are protected by a polymeric matrix and are highly resistant (Karunakaran *et al.*, 2011). Bacterial colonization and biofilm formation can occur during or after the implantation surgery, and infection can cause tissue damage or implant failure, as well as prevent bone tissue attachment (Liu *et al.*, 2015). The biofilm becomes resistant to antibiotics and the patient’s immune system, and even to chemical, mechanical, or physical actions, such as ultraviolet (UV) radiation and scraping, once formed. Therefore, preventing bacterial adhesion and biofilm formation on the implant is more effective than treating them afterward. Various bactericidal treatments have been developed in recent years, mainly involving the use of antimicrobial substances on the implant surface (Hasan; Crawford; Ivanova, 2013). However, these treatments have the main disadvantage of decreasing efficiency over time, as these substances are released, and also have potential toxicity. Moreover, another concern is the increased resistance of bacteria to antibiotic treatment, which further reduces its effectiveness.

2.3 EFFECT OF TOPOGRAPHY ON THE BIOLOGICAL BEHAVIOR

From a topographical point of view, the implant surface should promote the adhesion, proliferation, and/or differentiation of living tissue cells, while preventing the adhesion and proliferation of bacteria (Gallo; Holinka; Moucha, 2014). Recent studies suggest that roughness with micro- and nanoscale structures and controlled orientation can improve osseointegration by mimicking the natural environment of cells (Dumas *et al.*, 2012; Lim; Donahue, 2007). The direction of surface texturing can also influence cell growth (Lukaszewska-Kuska *et al.*, 2018). Microtopography aims to create a structure at the cellular scale, while nanotopography simulates the subcellular and molecular scale, including elements of the cytoskeleton, interactions between antibodies and antigens, and protein synthesis (Fernandez-Yague *et al.*, 2015). Cells actively sense the physical properties of the surface through focal adhesions, which are proteins that connect cells with the extracellular matrix (Biggs; Richards; Dalby, 2010). The size, number, and organization of focal adhesions can vary depending on the topography, which can affect the arrangement and distribution of cells and their functional differentiation processes. For instance, mesenchymal cells on surfaces with random roughness tend to have more elongated adhesion and higher tension in the cytoskeleton than on surfaces with ordered roughness (Günther *et al.*, 2016). Tension in the cytoskeleton is directly related to cell differentiation (high tension leads to osteogenesis, while low tension leads to adipogenic differentiation). Therefore, cell lineage is strongly dependent on topographical features (McBeath *et al.*, 2004). Surface characteristics can also be used to selectively influence cell adhesion, in addition to influencing cell differentiation. For instance, fibroblasts and epithelial cells adhere better to smooth surfaces, while osteoblast adhesion is enhanced on rough surfaces (Boyan *et al.*, 2001). This may allow implants to be optimized for specific applications. The influence of the topography on the cell adhesion is represented in Figure 2.8, which shows the higher number of cells on rough surfaces (acid-etched or grit-blasted) in comparison to the control as-machined sample.

Figure 2.8 - Cell adhesion in different surfaces. More cells are observed in the rougher surfaces (acid etched and grit-blasted)

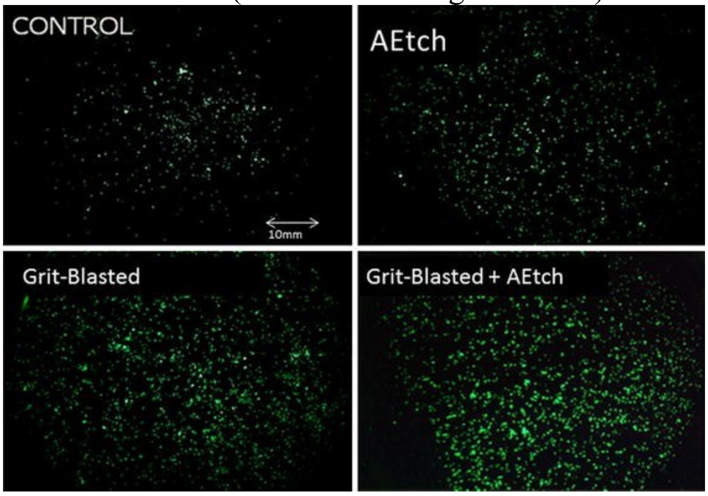

Source: (Herrero-Climent *et al.*, 2013).

Regarding microbial infection, the topography of implants can have a significant influence on the adhesion and proliferation of bacteria. Surfaces with microroughness (random structure) can promote bacterial proliferation (Bohinc *et al.*, 2014), while nanostructured surfaces can reduce bacterial adhesion and biofilm formation (Cunha *et al.*, 2016). Figure 2.9 shows the effect of laser nanotexturing on bacterial adhesion in titanium. Generally, for titanium surfaces, roughness greater than Ra=0.2 µm increases bacterial adhesion, while values below 0.2 µm do not produce significant changes (Bollenl; Lambrechts; Quirynen, 1997). However, Wang et al. showed that an increase in the roughness of ceramic materials does not result in increased microbial adhesion, with low biofilm formation (Wang; Shen; Haapasalo, 2014). The interaction between the mechanisms of bacterial adhesion and biofilm formation and nanostructured surfaces is still not fully understood and is a major subject of study, especially with the advancement of manufacturing techniques that allow for controlled nanostructuring.

Figure 2.9 - Bacterial attachment after 48h in polished (a,b) and laser textures (c,d) surfaces.

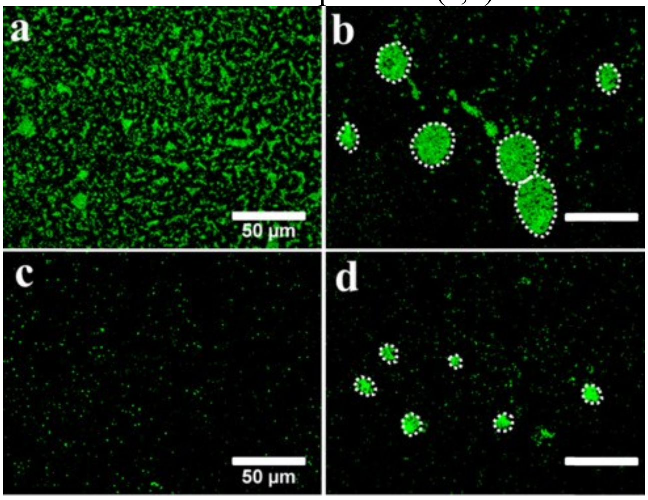

Source: Adapted from (Cunha *et al.*, 2016).

The influence of surface treatments on osseointegration and biofilm formation has been investigated for zirconia in several studies (Schünemann *et al.*, 2019). Generally, it has been observed that increasing the roughness of the zirconia surface by sandblasting and acid etching enhances osseointegration. However, sandblasting can induce stresses on the surface and cause a phase transformation from tetragonal to monoclinic, which deteriorates its mechanical properties (Aurélio *et al.*, 2016). Laser texturing of zirconia has shown good results in this context, as it improves the topographical characteristics of zirconia without necessarily affecting its mechanical properties (Roitero *et al.*, 2018a). The use of bioactive materials on its surface has also shown good results, as it improves bioactivity and reduces biofilm formation on implants, but more clinical studies are still needed to evaluate its efficiency (Schünemann *et al.*, 2019).

Creating micro- or nanoscale structures with controlled features to optimize osseointegration and minimize biofilm formation on implants can be a major challenge, especially for bioceramics, which have high hardness and low fracture toughness. In this context, laser texturing is a fast and precise method of generating controlled patterns, which allows the production of micro- and nanotopography on the implant surface (Palmquist *et al.*, 2010). In particular, the technique known as Direct Laser Interference Patterning (DLIP) is a promising approach that allows the fabrication of periodic structures in a wide range of materials (metals, polymers, and ceramics) in a single-step process (Alamri; Lasagni, 2017).

2.4 LASER SURFACER STRUCTURING

2.4.1 Fundamentals of laser processing

Laser stands for light amplification by stimulated emission of radiation, which is a process that generates an electromagnetic beam with high coherence, convergence, and monochromaticity. The laser beam can have a wide range of wavelengths, from ultraviolet to infrared, depending on the type and configuration of the laser source. Lasers have been widely used in various fields, such as materials processing, medicine, electronics, etc., due to their advantages of flexibility, precision, and speed.

Compared to conventional processing techniques, laser processing techniques offer several benefits. Lasers can achieve high energy density and precision, enabling localized processing with a spatial resolution of less than 10 nm. The monochromaticity of the laser allows for controlling the depth of processing on the material surface by simply varying its wavelength. Moreover, the laser beam can move much faster than any mechanical tool or conventional heat source. The laser is also free from wear or breakage, unlike mechanical tools, and prevents contamination of the processed material. As it does not contact the part, the laser can be used in sterile components, which is an important factor for biomedical applications (Bäuerle, 2011).

The active medium, power, wavelength, and temporal behavior (continuous or pulsed) are the main characteristics of the laser. The beam can be continuous or pulsed, with pulse durations ranging from femtoseconds (10^{-15} s) to milliseconds (10^{-6} s). Generally, shorter pulses result in smaller affected areas and higher process control. The fluence, which is the energy of a single pulse per unit area (usually expressed in J/cm^2), is another important parameter for pulsed lasers. The active medium is where the radiation is generated by the excitation of electrons by a source, such as gases (CO_2, Argon), solid-state materials with dopants (Nd:YAG), diodes, etc. Different active media produce lasers with different power and wavelengths (Poprawe, 2011).

Laser-matter interaction involves the interaction of photons from the laser beam with particles from the material (molecules, atoms, and subatomic particles). In a crystalline solid, the main interaction is between the electromagnetic field of the laser beam and the electrons of the material. The beam can be absorbed, transmitted, and/or reflected, depending on the electronic configuration of the material. The absorption of energy causes the excitation of electrons, which can lead to localized heating (photothermal effect) and/or chemical transformations (photochemical effect). These phenomena are influenced by both the laser parameters (power and pulse duration) and the optical, thermal, and electronic properties of the material.

2.4.2 Laser machining and structuring

The thermal and chemical effects of the laser beam can cause microstructural changes, phase transformation, and thermal residual stresses in the material. These changes can be exploited for material processing, especially for machining. Ceramics are difficult to machine by conventional methods due to their high hardness and low toughness, which lead to high tool wear, low material removal rates, and mechanical and thermal damage to the workpiece. Laser machining can overcome these challenges by using a high-density laser beam to remove material from the interaction region by fusion, dissociation, evaporation, and expulsion (Samant; Dahotre, 2009).

To produce micro- and nano-textures on the surface of materials, the ablation process is used, which basically consists of localized vaporization of the region of incidence of the laser focus on the surface of the material. The quality and dimensional control of the ablated region depends on both the laser parameters (such as radius, focus, pulse duration, and wavelength) and the material properties, such as reflectivity, absorptivity, thermal conductivity, melting temperature, etc. (Poprawe, 2011).

Photochemical ablation and thermal ablation are the two main types of ablation. Thermal ablation happens at lower fluence values when the material is locally heated evaporated and/or sublimated. This process affects not only the region under the laser beam but also the surrounding area due to heat conduction, creating a thermally affected zone (HAZ). This mechanism reduces the precision of the process. Photochemical ablation occurs at higher laser energy and shorter excitation time when the material does not have time to increase its temperature. In this process, the material undergoes ionization and direct bond breaking, leading to disintegration and expulsion of the material by electronic repulsion. This process is more precise, as it mainly affects the region under the laser beam (Brown; Arnold, 2010; Poprawe, 2011). These two processes usually coexist.

The pulse duration of the laser has a significant influence on the ablation process. The ablation in short pulsed lasers (nanosecond or longer) is largely based on thermal ablation, where the surface absorbs the laser energy increasing its temperature up to a level where it vaporizes or melts, resulting in the removal of material. As the pulse is delivered over a relatively longer time, more heat accumulates in the material, causing alterations also in the surroundings of the ablated zone, such as resolidified layer, phase change, and microcracking. Ultra-short pulsed lasers (picosecond or shorter), on the other hand, deliver the high-peak energy to the material in an ultra-short time frame, causing rapid material expulsion. This reduces the heat transfer to the adjacent region, resulting in a smaller thermally affected zone. The high peak power leads to a non-linear interaction with matter, resulting in a highly localized energy deposition that can lead to photochemical ablation. Therefore, the ablation region is more precise and there is less residual heat in the rest of the material (Brown; Arnold, 2010). Figure 2.10(a) illustrates this effect, showing a large amount of resolidified material around the ablation region for a nanosecond laser, while Figure 2.10(b) shows a much more precise ablation for a femtosecond laser.

Figure 2.10 - Laser ablation of steel using a (a) nanosecond laser and a (b) femtosecond laser.

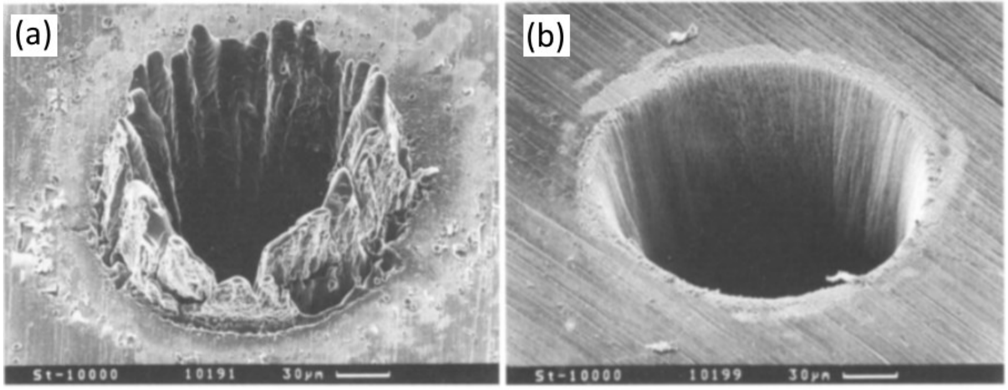

Source: Adapted from (Chichkov *et al.*, 1996).

Zirconia's microstructure and mechanical properties can be affected by surface treatments, such as sandblasting, acid etching, or laser processing. Zirconia relies on the stress-induced transformation of the metastable tetragonal phase to the monoclinic phase for its tenacification mechanism. Therefore, zirconia is highly susceptible to microstructural changes, such as grain size variation, residual stress generation, and stabilizing element alteration, even locally (Chevalier *et al.*, 2009). Laser treatment can induce severe damage to the surface and microstructure of the material, as well as cause compositional changes, due to the high thermal energy involved in the laser-matter interaction. Hence, it is crucial to evaluate the impact of laser treatment on the material and its optimal parameterization.

Several studies have demonstrated the successful use of lasers for zirconia processing. Li *et al.* (2016) created high-quality blind holes (⌀=500 µm) and micro-sized steps (100 µm height) in zirconia bodies (Y-TZP) using a nanosecond solid-state laser (wavelength 532 nm). They did not observe any phase transformation of zirconia or microcracking after laser machining. Berger *et al.* (2016) used a microlens array (MLA) with a nanosecond Nd:YAG laser (wavelength 355 nm) to texture alumina, zirconia, and hydroxyapatite (HA). They achieved successful machining of all three materials fabricating dimples with a diameter of ~20 μm and a spatial distance of 150 μm. The HA samples showed greater texture depth, which can be attributed to its lower decomposition and melting temperature, while the smallest structures were obtained in alumina, probably due to its high thermal conductivity. On the textured region of zirconia, defects related to laser processing, such as porosity and microcracking, were observed. Delgado-Ruiz *et al.* used a femtosecond laser to create grooves 30 μm wide and 70 μm deep on zirconia implants, which were implanted in dogs' mandibles. By using an ultra-short pulsed laser, the authors reported no significant damage to the microstructure. Indeed, the laser texturing removed contaminants and microstructural defects incorporated in previous stages of manufacturing. They also observed greater bone-implant contact and bone density in the implant periphery compared to titanium and zirconia implants treated by sandblasting and acid etching (Delgado-Ruíz *et al.*, 2011, 2015).

Hirota *et al.* (2019) investigated the effects of nanosecond pulsed Nd:YAG laser (1064 nm) texturing on yttria-stabilised zirconia (Y-TZP) and ceria-stabilised zirconia (Ce-TZP) implants containing 30% alumina. They compared the bone response of laser-textured implants with acid-etched implants after implantation. The laser texturing was successfully performed on both materials without inducing cracks, but the Ce-TZP implants turned black, possibly due to oxygen depletion by the laser (Sinhamahapatra *et al.*, 2016). This phenomenon might have been more pronounced in Ce-TZP because of the higher thermal conductivity of alumina, which could increase the temperature during laser treatment (Hostaša; Pabst; Matějíček, 2011). The oxygen depletion might have also affected the biological response of Ce-TZP, which showed a lower bone response than Y-TZP. The authors did not evaluate the phase changes induced by the laser in this study. Goyos-Ball *et al.* (2018) also studied the laser texturing of Ce-TZP and alumina nanocomposites using a nanosecond pulsed fiber laser (515 nm). They achieved successful texturing of the nanocomposites, but they also observed some discoloration and surface micro-cracks. The micro-cracks did not propagate into the bulk of the material and did not compromise its mechanical strength, probably because of the high fracture toughness of the material. The authors also detected some phase transformation from monoclinic to tetragonal zirconia. They performed in-vitro tests to assess the biological response of the samples and concluded that the laser-textured surface was favorable for cell differentiation.

Holthaus, Treccani, and Rezwan (2011) evaluated the performance of different texturing techniques (microtransfer molding, modified micromolding, Aerosol-Jet® printing, CNC machining, laser ablation, and Direct Laser Interference Patterning (DLIP)) on various ceramic surfaces (zirconia, alumina, silica, and hydroxyapatite). They used a nanosecond Nd:YAG laser (1064 nm wavelength) to perform ablation on the ceramics with features size down to 30 μm and obtained satisfactory results, but the ablation regions had imprecise edges and high surface roughness compared to the other techniques. They also applied the DLIP technique using the same Nd:YAG laser but with a wavelength of 266 nm, achieved by harmonic generation. This technique produced better-defined edges and much lower roughness than the conventional laser ablation technique, in addition to a smaller feature size (10 μm). The authors attributed this improvement to the shorter wavelength, which increased the absorption of laser radiation and the occurrence of photochemical ablation. The DLIP method also showed higher speed in texturing large areas than the other methods studied. Thorough literature reviews on laser modification of zirconia surfaces can be found in (Cunha, Welson *et al.*, 2022; Han *et al.*, 2021).

2.4.3 Direct Laser Interference Patterning (DLIP)

The DLIP technique involves splitting the laser beam into two or more beams and superimposing them on the material surface. The superposition of the beams creates regions of constructive and destructive interference, resulting in a periodic distribution of laser energy over the exposed area. The regions of constructive interference have high energy and cause ablation, while the regions of destructive interference have low energy and leave the material intact. Thus, an interference pattern is formed and transferred to the material as a well-defined texture. For instance, the superposition of two laser beams (Figure 2.11(a)) produces a periodic pattern of lines (with spatial period Λ), as shown in Figure 2.11(b). The period can be adjusted by changing the angle of incidence between the two beams, as given by Equation (2.1) (Dahotre; Harimkar, 2008):

$$\Lambda = \frac{\lambda}{2\sin(\theta)} \tag{2.1}$$

where λ is the laser wavelength and θ is half the angle formed between the interfering beams. By adjusting the number, intensity, and polarisation of the beams, different texturing patterns can be created, such as dots and lamellae. The DLIP technique allows the fabrication of structures in the order of magnitude of the laser wavelength, which is at least one order of magnitude smaller than what can be achieved by conventional laser optical setups at their focus. Moreover, the texture is engraved over the entire area exposed to the interference region simultaneously, unlike the conventional laser, where the beam has to scan the whole geometry (Roitero *et al.*, 2017b). However, as most laser techniques, in addition to ablation, the high energy generated at the maxima positions can also produce unwanted modifications, such as phase transformation, oxidation, melting, and microcracking.

Figure 2.11 - Illustrations showing (a) the interference of two laser beams and (b) the calculated energy distribution.

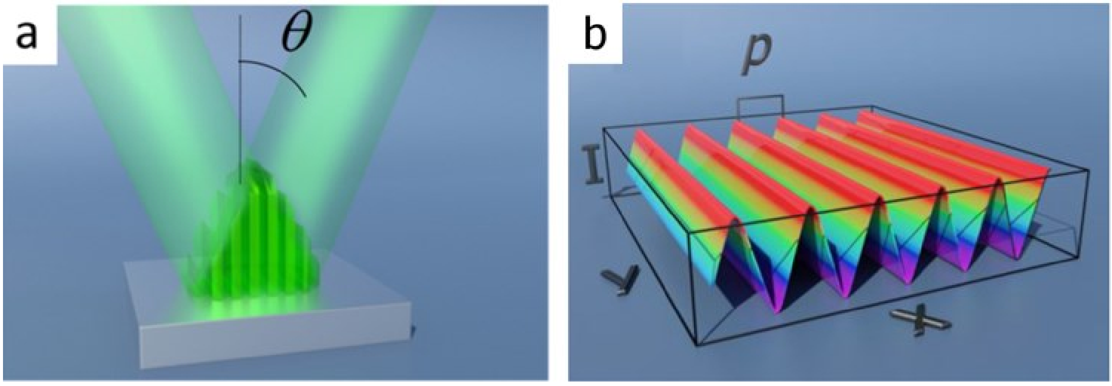

Source: Adapted from (Lasagni, 2017).

The DLIP technique requires the incident beams to have temporal and spatial coherence to produce the interference phenomenon. Therefore, instead of using multiple laser sources, a single laser source is used and its beam is split into two or more beams. Different optical configurations can be employed to split and superimpose the laser beams, the most common one being a beam splitter (Figure 2.12). In this configuration, the laser beam passes through a half-mirror (beam splitter), which divides it into two beams, which are then reflected by mirrors towards the material. For configurations with more than two beams, more half-mirrors are used. Diffractive Optical Elements (DOE) can also be used to split the laser beam into an array of sub-beams by diffraction. Other optical elements, such as collimating lenses and polarisers, can be used to improve the quality and focus of the laser beam. More details on the fundamentals of direct laser interference patterning can be found in (Lasagni, 2017).

Figure 2.12 - DLIP optical setup using a half-mirror to split the initial beam.

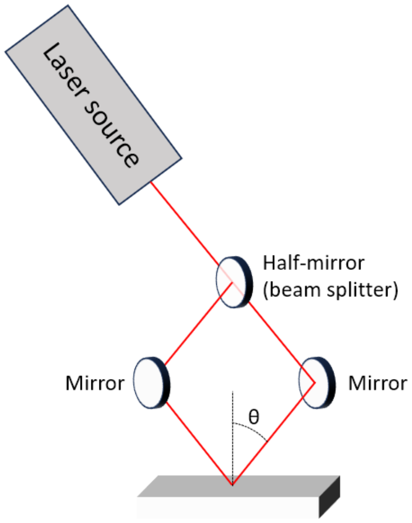

Source: Author.

Micro and nanotextures can be created on biomaterials by selective ablation using laser irradiation. These textures can enhance the surface roughness and improve the performance of the implant by facilitating osseointegration, guiding cell proliferation, or inhibiting biofilm formation. Direct Laser Interference Patterning (DLIP) is a technique that enables precise control of the texturing dimensions by adjusting the laser parameters (Dahotre; Harimkar, 2008). DLIP has been applied to various biomaterials, such as polymers and metals, and has shown promising results.

The effect of laser-induced surface topography on bacterial adhesion and cell growth in polymeric materials was investigated by Guenter et al. using direct laser interference patterning (DLIP). They applied DLIP to polyamide and polystyrene substrates to produce lines, pillars, and lamellae patterns with spatial periods between 0.5 and 5.0 µm and tested their antibacterial properties *in vitro* and *in vivo*. They found that linear patterns enhanced bacterial attachment, while complex lamellar patterns inhibited biofilm formation (Guenther *et al.*, 2016). Valle *et al.* (2015) obtained similar results using DLIP on different polymers, showing that line and pillar structures with spatial periods between 1 and 5 µm increased bacterial adhesion, while irregular lamellar structures reduced it. Langheinrich *et al.* (2012) used DLIP to create line-like patterns on polyamide and studied their effect on cell alignment. They observed that the cells oriented themselves along the direction of the patterns, demonstrating the ability of laser texturization to influence cell behavior in biomedical applications. Zwahr *et al.* (2017) compared the performance of DLIP with conventional surface treatments such as acid etching and sandblasting on titanium implants. They showed that DLIP improved cell viability and metabolism, which could enhance bone healing and implant stability. These studies suggest that DLIP is a promising technique for creating functional surfaces with tailored topographies for various applications.

Direct laser interference patterning (DLIP) has been already applied to create surface textures on zirconia substrates without altering their microstructure or compromising their mechanical strength (Fabris *et al.*, 2019). Daniel et al. produced linear patterns on zirconia stabilized with 5 mol% yttria with a spatial period of 3.3 μm with a nanosecond laser system. They observed a porous surface and a recrystallization layer with nanometric grains, resulting in an improved flexural resistance (Daniel *et al.*, 2008; Daniel; Drummond; Giordano, 2008). However, the quality of the textures depends on the careful selection of the laser parameters, such as the number of pulses and the energy density. High values of these parameters can increase the depth of the textures but also cause surface defects such as pores, cracks, recrystallization, and phase transformation (Roitero *et al.*, 2017b). Figure 2.13 shows the surface and cross-sectional images of zirconia samples textured by DLIP using two different laser wavelengths: 532 nm and 355 nm. The authors used different optical setups with a nanosecond laser to produce linear patterns with different periods (4-10-15 μm). They observed intergranular cracks with a depth of up to 1 μm on all samples, regardless of the wavelength or period. They also detected recrystallized grains with an elongated shape perpendicular to the surface and a phase change from tetragonal to monoclinic around the cracks. These results indicate that DLIP can induce thermal stress and damage on zirconia surfaces, which can affect their performance and functionality. Therefore, optimization of the laser parameters is essential to achieve high-quality textures with DLIP. The same authors also examined the influence of DLIP on the mechanical strength and low-temperature degradation of 3Y-TZP. They reported that laser patterning slightly decreased the biaxial strength of the material, but improved its reliability, as indicated by a higher value of Weibull parameter *m*. Moreover, DLIP samples were also more susceptible to LTD, but a subsequent annealing thermal treatment can enhance again the aging resistance (Roitero *et al.*, 2018b, 2018a).

Figure 2.13 - Surface and cross-section of zirconia samples textured with wavelengths of 532 nm (a, b) and 355 nm (c, d).

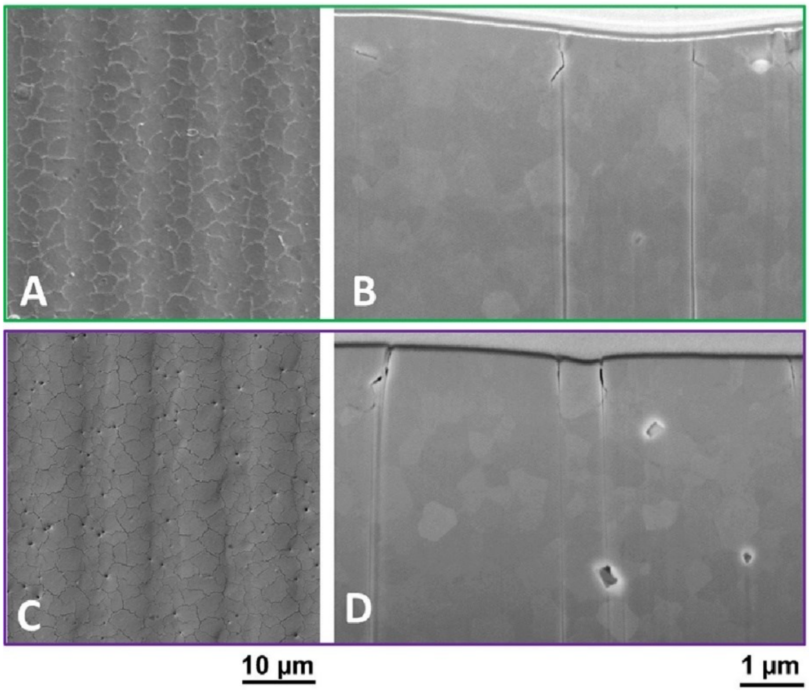

Source: Adapted from (Roitero *et al.*, 2017b).

In more recent studies, ultra-short pulsed lasers have been applied to zirconia with minimal microstructural damage and enhanced resolution. Müller et al. applied a femtosecond laser to texture line-like patterns with a periodicity of 3 µm on 3Y-TZP. They achieved an excellent texture definition, with a clear distinction between ridges and grooves. The ablated grooves exhibited some sub-micrometric porosity and cracking (Müller *et al.*, 2020). Similarly, our research group reported a series of linear structures on zirconia produced by a picosecond laser with a DLIP setup, varying the laser parameters such as fluence and pulse overlap. For low laser energy levels (low fluence and/or overlap) the linear structures are not completely developed, while for excessive energy (high fluence and/or overlap) the pattern is destroyed, with no clear distinction between ridges and grooves. However, for an optimal range of fluence and pulse overlap, well-defined and defectless grooves were obtained, and their dimensions (depth and width) could be tuned by varying the laser parameters. The only defects found in the microstructure were some open porosities, microcracking, and melting droplets, also in the sub-micrometric and nanometric scale (Henriques *et al.*, 2023a, 2023b). Figure 2.14 shows the topography and morphology of the laser-patterned samples using a picosecond source. In comparison to previous studies using nanosecond lasers (as shown in Figure 2.13), the pattern is more defined and homogeneous and presents fewer microstructural defects.

Figure 2.14 – Topography (a, b) and microstructure (c, d) of the structures fabricated on zirconia using a picosecond DLIP.

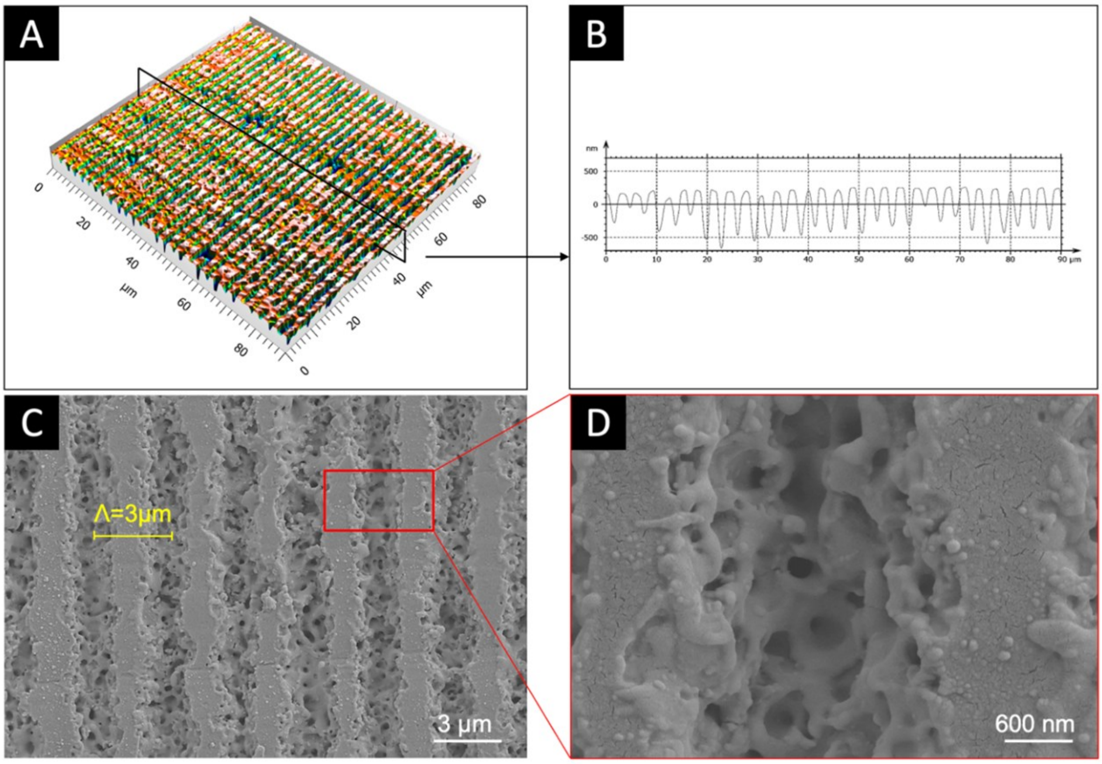

Source: (Henriques *et al.*, 2023b).

This work is the first to apply direct laser interference patterning (DLIP) to Ce-TZP nanocomposite samples. No previous studies have reported on the use of this technique for this type of material. However, the existing literature suggests that DLIP can be successfully applied to other ceramic-based implants by adjusting the laser parameters to achieve optimal mechanical and biological properties. Furthermore, this work aims to provide a thorough investigation on the effects of laser texturing on the microstructure and mechanical reliability of both dental grade zirconia and nanocomposite.

3 INFLUENCE OF LASER PARAMETERS ON TEXTURING OF 3Y-TZP AND Ce-TZP/Al_2O_3/$SrAl_{12}O_{19}$ COMPOSITE

3.1 ABSTRACT

The development of new materials and surface functionalization processes has been extensively studied to further improve the performance of implants. A novel zirconia-based nanocomposite (Ce-TZP/Al_2O_3/$SrAl_{12}O_{19}$) has been showing promising results regarding its mechanical properties, with high strength, toughness, and low susceptibility to low-temperature degradation. This work aimed to explore the laser ablation technique as a potential alternative to produce controlled textures on the surface of traditional 3Y-TZP and the novel composite. A 532 nm picosecond Direct Laser Writing (DLW) system was used to produce lines in compact sintered samples of both materials. Laser pulse fluence, repetition rate, and scanning speed were varied to evaluate the influence of each of these parameters on the ablation characteristics of each material. The resulting textured samples were analyzed using confocal and scanning electron microscopes. Both materials were successfully textured using the laser technique, but the groove morphology and geometry are highly dependent on the parameters used. While low energy levels (low fluence, low repetition rate, and/or high speed) result in shallow and irregular grooves, high energy (high fluence, high repetition rate, and/or low speed) can result in crack and resolidification layer. Overall, for the same set of parameters, the laser produced wider and deeper grooves in the nanocomposite (up to 30 μm wide and 26 μm deep) than in the 3Y-TZP (up to 12 μm wide and 6 μm deep), considering good-quality grooves only. Hence, this work showed the feasibility of laser texturing of traditional 3Y-TZP and the novel Ce-TZP/Al_2O_3/$SrAl_{12}O_{19}$ that can be further explored to functionalize their surfaces for biomedical applications, for example.

3.2 INTRODUCTION

Zirconia (ZrO_2) is a ceramic material that has attracted significant interest due to its unique properties, such as high strength, toughness, hardness, and wear resistance, as well as its ability to withstand high temperatures and corrosive environments. These properties make zirconia a versatile material for a variety of high-performance applications, such as load-bearing and wear applications (Parveez; Wani, 2021), thermal barrier coatings (Liu; Huang; He, 2019) and biomedical applications (Bona; Pecho; Alessandretti, 2015; Chevalier; Gremillard, 2017).

Among the different zirconia compositions, 3 mol% Y_2O_3 stabilized tetragonal polycrystalline zirconia (3Y-TZP) is the most widely used and studied for biomedical applications due to its outstanding strength (up to 1200 MPa), higher than any other single-phase oxide ceramic. However, 3Y-TZP has some limitations, such as its moderate toughness (~6 MPa·√m), which leads to a large scatter in strength data and requires the use of statistical failure approaches (Chevalier *et al.*, 2020), and its susceptibility to low-temperature degradation (LTD), which can compromise its long-term reliability (Lughi; Sergo, 2010). On the other hand, zirconia stabilized with ceria (Ce-TZP) and its composites exhibit a significant amount of transformation-induced plasticity, with toughness values reaching 20 MPa·√m, and substantially reduced sensitivity to LTD (Chevalier *et al.*, 2009). In recent years, researchers have focused on developing Ce-TZP-based composites to enhance their mechanical strength, by adding an immiscible second phase, such as alumina, to decrease zirconia-grain size, and/or introducing another toughening phase, such as elongated aluminate phases (Li *et al.*, 2023). Among the novel zirconia composites, the 84 vol% Ce-TZP/8 vol% Al_2O_3/8vol% $SrAl_{12}O_{19}$ nanocomposite stands out for its high strength (~800 MPa), high toughness (~10 MPa·√m) and almost no susceptibility to LTD (Chevalier *et al.*, 2020; Reveron *et al.*, 2017).

Surface modifications can alter the behavior and interactions of materials with their environment, and thus enhance their performance in engineering applications. Surface modifications can improve various properties of materials, such as wear resistance, wettability, adhesion to other materials, and biocompatibility, while preserving the desirable bulk properties of the material (Pu *et al.*, 2020; Soon *et al.*, 2016; Wei; Gremillard, 2019). For biomedical applications, surface treatments have been applied to zirconia to improve the bonding between the zirconia implant and dental cement and porcelain (Henriques *et al.*, 2018b, 2020), and to accelerate the osseointegration process and decrease bacterial biofilm formation (Kligman *et al.*, 2021). These treatments seek a chemical modification, such as coating with bioactive materials, and/or physical modification, through the surface roughening. Conventional methods for surface roughening in zirconia include surface grinding, airborne particle abrasion (grit-blasting), or acid etching (Schünemann *et al.*, 2019). However, these techniques produce only random surface patterns with low dimensional control of feature size. Studies have demonstrated that topography with controlled micro- and nanofeatures with specific orientations can improve osseointegration by mimicking the natural environment of cells (Dumas *et al.*, 2012; Lim; Donahue, 2007). Texture direction can also guide cell growth (Lukaszewska-Kuska *et al.*, 2018). To achieve such geometric control of the topographic features, laser texturing has emerged as an excellent alternative to fabricate controlled micro- and nanotopographies in a wide range of materials, including zirconia.

In the laser processing technique, high-density optical energy is incident on the surface of the workpiece, and material is locally removed by melting, dissociation, and/or evaporation (Samant; Dahotre, 2009). Laser technology is an ideal tool for surface treatment of extremely hard materials, such as zirconia, as it can remove material by these phenomena. Moreover, as a contactless method, it can be used when strict control of surface contamination is required, such as implant surfaces. However, laser treatment should be carefully applied to zirconia, as some limitations can arise, such as excessive heating that can cause remelted layers and crack formation, laser-induced phase transformation, and unwanted chemical changes (Hirota *et al.*, 2019; Noda *et al.*, 2010; Roitero *et al.*, 2018b). Therefore, the laser parameters should be appropriate to ensure a defect-free and efficient material removal. The pulse duration, for example, is directly related to the final quality of the textured surface. The ablation using relatively long pulse duration lasers (ns or ms) involves mainly thermal mechanisms, resulting in excessive heating, melting, and evaporation of the material, which may induce the issues mentioned above (Zhou *et al.*, 2018). On the other hand, for ultra-short pulsed lasers (ps or fs), non-thermal ablation mechanisms prevail, allowing the ablation of very thin surface layers, resulting in less thermal damage to the surface and higher quality of the produced features (Abu Ruja; De Souza; Finer, 2019).

The morphological and geometric features of the ablated surface can also be manipulated by using different types of lasers, intensity, wavelength, repetition rate, and scan speed. Several studies have successfully analyzed the influence of laser parameters on 3Y-TZP (Han *et al.*, 2021), but no studies were found regarding laser texturing of the nanocomposite Ce-TZP/Al_2O_3/$SrAl_{12}O_{19}$. Therefore, this study aimed to investigate the influence of laser parameters on the ablation of traditional 3Y-TZP and the novel nanocomposite Ce-TZP/Al_2O_3/$SrAl_{12}O_{19}$ using an ultra-short pulsed laser source (10 ps) working at a wavelength of 532 nm. Laser energy, repetition rate, and scanning speed were varied to evaluate the effect of each of these parameters on the geometry and morphology of the ablated features.

3.3 MATERIALS AND METHODS

3.3.1 Substrates fabrication

Commercial zirconia powder stabilized with 3 mol% yttria (TZ-3YSB, Tosoh, Japan) and composite powder with composition of 84 vol% ZrO_2 (11 mol% CeO_2), 8 vol% of Al_2O_3 and 8 vol% of $SrAl_{12}O_{19}$ (referred as $ZA_8Sr_8Ce_{11}$ from now on) (DOCERAM, Germany) were used. The powders were uniaxially pressed in steel dies at 100 MPa for zirconia samples and 70 MPa for composite samples for 60 s to obtain the green compacts. Afterward, the green compacts were sintered in a high-temperature furnace (Sinter F-1800 10P, EDG) in air at 1500°C for 2h (zirconia) and 1450°C for 1h ($ZA_8Sr_8Ce_{11}$). The sintered samples had a dimension of 16.9 mm diameter and 1.6 mm thickness. Samples were ground using sandpaper (grit size from #120 up to #1500) and polished (down to grit size of 1 μm of diamond particles) to achieve a flat surface and a mirror-like finish.

3.3.2 Laser texturing

Direct Laser Writing (DLW) technique was used to ablate 1 mm long lines at the surface of the samples through a single-pass. The laser system consists of a solid-state pulsed $Nd:YVO_4$ source (Edgewave PX200) that emits 532 nm (green) wavelength with a 10 ps pulse duration, maximum output power of 50 W and beam quality $M^2=1.1$. The laser beam was positioned and focused at the sample surface using a galvanometer scanner system (Miniscan, Raylase) with a scan area of 100 x 100 mm^2, resulting in a Gaussian beam with a spot size of 30 μm. The laser processing is illustrated in Figure 3.1, along with the processing matrix, where the scanning speed and laser fluence (pulse energy density) were varied in the horizontal and vertical axis, respectively. This matrix was processed for different repetition rates. The repetition rate (number of pulses emitted per second) and the laser speed determine the pulse overlap and, consequently, the number of pulses that hit the same area, i.e., a higher repetition rate and/or lower speed result in more pulses (and more accumulated energy) hitting the same spot. All laser parameters are summarized in Table 3.1. The laser fluence was calculated using equation (3.1):

$$F_p = \frac{E_p}{A_p} = \frac{P}{f * A_p} \qquad (3.1)$$

Where F_p is pulse fluence, E_p is the pulse energy, A_p is the irradiated area at the focal point, P is the laser power and f is the repetition rate. Especially for low speeds and high repetition rates, more than one pulse can irradiate the same area, so the accumulated laser fluence (accumulated energy per surface area) was also calculated by the following equation (3.2):

$$F_{acc} = F_p * \frac{d*f}{s} \tag{3.2}$$

Where F_{acc} is the accumulated fluence, d is the beam diameter and s is the scanning speed.

Figure 3.1 - Illustration of the laser processing and the parametric study.

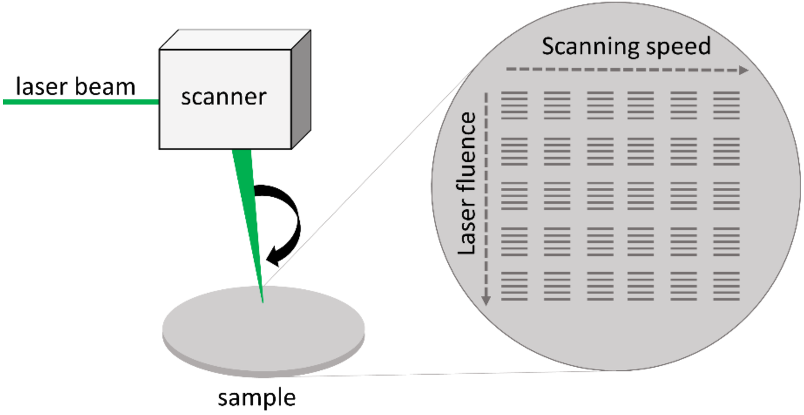

Source: Author.

Table 3.1 - Summary of the processing parameters.

Wavelength	532 nm
Pulse duration	10 ps
Beam spot size (diameter)	30 µm
Fluence	0 ~ 3.1 J/cm²
Repetition rate	1 ~ 100 kHz
Scanning speed	1 ~ 200 mm/s

Source: Author

3.3.3 Topographic analysis

The topography of the ablated grooves was examined using a confocal microscope (S Neox, Sensofar) with 50x and 150x objectives, resulting in vertical and lateral resolutions of 2 nm and 140 nm, respectively. The morphology of the treated regions was analyzed using a Scanning Electron Microscope (SEM, TM-3030, Hitachi) at an operating voltage of 15.0 kV.

3.4 RESULTS

3.4.1 Morphology

Figure 3.2 shows SEM images of the laser-textured samples for both materials and the different conditions tested. Grooves were successfully fabricated through laser ablation of the material for most conditions tested. In the empty spaces of the figure (mainly for low fluence and high speeds), the laser energy was insufficient to ablate material significantly. The quality of the grooves was evaluated in terms of homogeneity, dimensions (depth and width), and the presence of defects, such as melting and cracks.

For the highest frequency (100 kHz), $ZA_8Sr_8Ce_{11}$ exhibited cracks and/or melting for every condition, even for accumulated fluence as low as 12 J/cm² (0.9 J/cm² fluence and 200 mm/s). For this same condition, 3Y-TZP presented a well-defined and homogeneous groove, despite defects appearing for more aggressive conditions. At a 50 kHz repetition rate, well-defined and defect-free grooves were obtained only at high speeds (>100 mm/s, i.e., less than 15 pulses irradiating the same area), while for low speeds, melting and cracking occurred. Indeed, at lower speeds (< 10 mm/s), defects are present for every condition, irrespective of repetition rate or laser fluence, indicating that a large number of pulses generates excessive heat and damages the material. For a lower number of pulses (between 3 and 6 pulses per area), the largest number of well-defined and defectless grooves were achieved, regardless of the laser fluence. These areas are marked by a red border. Although both materials followed a similar trend, the zirconia 3Y-TZP presented ablation at lower values of fluence compared to the $ZA_8Sr_8Ce_{11}$, indicating a lower ablation threshold. On the other hand, when the fluence exceeds the threshold, more material is removed from the composite, which can be seen by its wider grooves. Moreover, for low frequency (1 kHz) and high speed (50 mm/s), larger individual pulses can be observed for the composite.

Figure 3.2 - SEM images of the laser-ablated grooves for the different conditions tested (repetition rate, fluence, and scan speed). Conditions marked in red resulted in good-quality grooves.

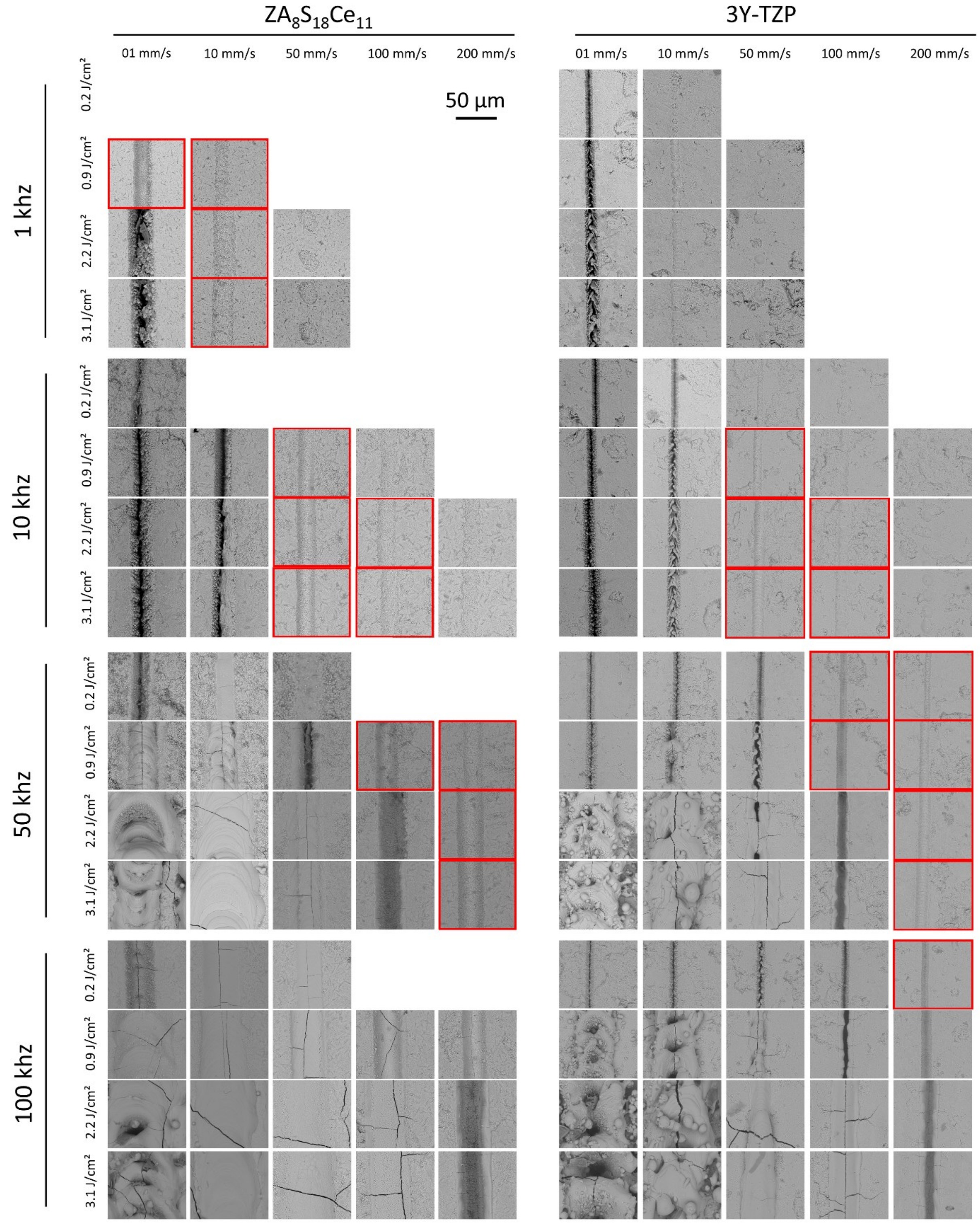

Source: Author.

The laser parameters have a significant influence on the quality of the textured grooves, as shown in detail in Figure 3.3(a-c) for the 3Y-TZP and Figure 3.3(d-f) for the

$ZA_8Sr_8Ce_{11}$. For low values of accumulated fluence (low fluence, repetition rate, and/or high speeds), shallows and incomplete structures are produced, as shown in Figure 3.3(a) and Figure 3.3(d) for the following conditions: fluence 0.9 J/cm², speed 100 mm/s and frequency rate 10 kHz. Conversely, for high accumulated fluence (Figure 3.3(b) and Figure 3.3(e), fluence 2.2 J/cm², speed 50 mm/s and frequency rate 50 kHz), the high energy leads to an excessive increase in the surface temperature and melting of the surrounding region, which accumulates inside the grooves. Cracking can also be observed parallel and perpendicular to the groove, extending to the surrounding material. Good quality grooves, as shown in Figure 3.3(c) and Figure 3.3(f), are obtained for medium values of accumulated fluence (2.2 J/cm², 50 mm/s, 10 kHz). For these conditions, the groove is well-defined, homogeneous, and almost defect-free (cracks and/or excessive remelting) for both materials, although some signs of remelting can be observed for the 3Y-TZP. Comparing the materials, it is clear that for the same energy conditions, the composite presents wider grooves, but the geometric size will be analyzed in more detail in the next section based on the confocal images.

Figure 3.3 - SEM images of three conditions for ZrO_2 (a, b, and c) and $ZA_8Sr_8Ce_{11}$ (d, e and f).

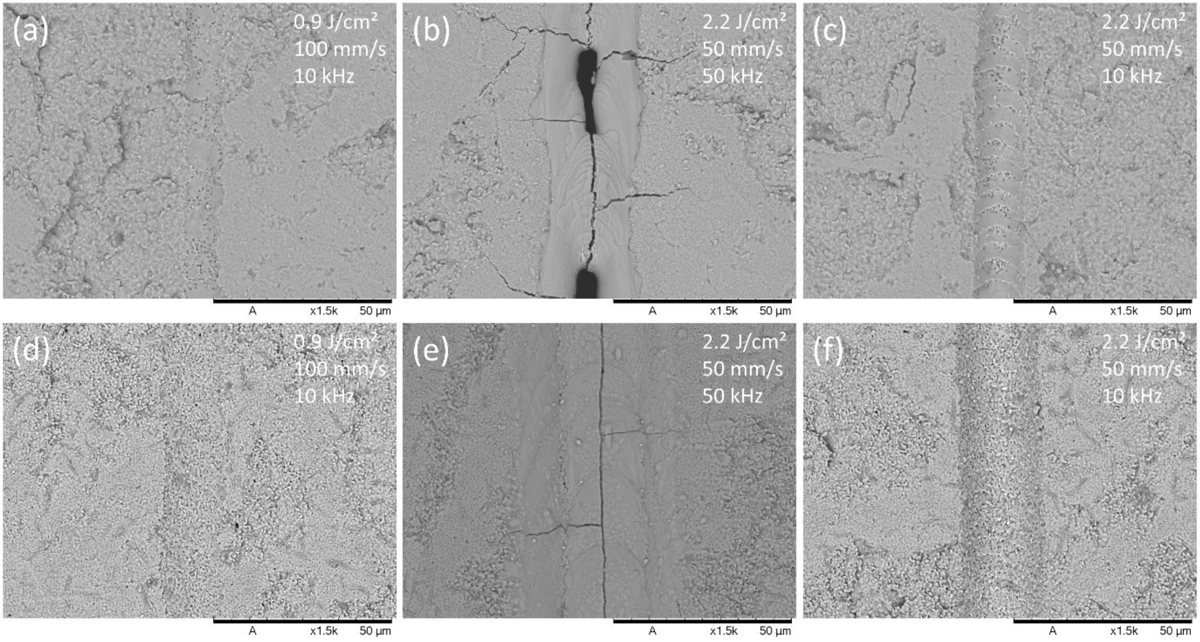

Source: Author.

3.4.2 Topography

The confocal images confirmed the observations obtained by the SEM analysis, as shown in Figure 3.4, which presents the same conditions as Figure 3.3. Figure 3.4(a-c) shows the topography of the 3Y-TZP samples and Figure 3.4(d-f) shows the ZA$_8$Sr$_8$Ce$_{11}$ for the same energy conditions represented in Figure 3.3. For the low energy condition (Figure 3.4(a) and Figure 3.4(d)), the groove's width and height are not uniform for both materials, although the groove is somewhat deeper (2.8 μm) and wider (19.1 μm) for the composite compared to zirconia (1.7 μm deep and 10.3 μm wide). For the high energy level, zirconia (Figure 3.4(b)) presented a ridge, indicating that the material has melted and accumulated inside the groove. On the other hand, the ZA$_8$Sr$_8$Ce$_{11}$ composite (Figure 3.4(e)) presented an irregular and shallow (up to 5.2 μm deep) groove for the same condition. As seen in Figure 3.3, this condition also leads to cracking at the groove and the surrounding region. For the moderate energy condition (2.2 J/cm^2, 50 mm/s, 10 kHz), both materials presented a homogeneous and well-defined structure. However, the composite presented again a much deeper (8.0 μm) and wider (23.6 μm) structure compared to zirconia 3Y-TZP (4.1 μm deep and 10.7 μm wide). From the confocal images, it is also possible to observe the V-shape from the grooves due to the Gaussian nature of intensity distribution.

Figure 3.4 - Topography of the textured grooves of 3Y-TZP (a, b and c) and ZA$_8$Sr$_8$Ce$_{11}$ (d, e and f) for three different conditions: 0.9 J/cm^2, 100 mm/s and 10 kHz (a, d); 2.2 J/cm^2, 50 mm/s and 50 kHz (b, e); and 2.2 J/cm^2, 50 mm/s and 10 kHz (c, f).

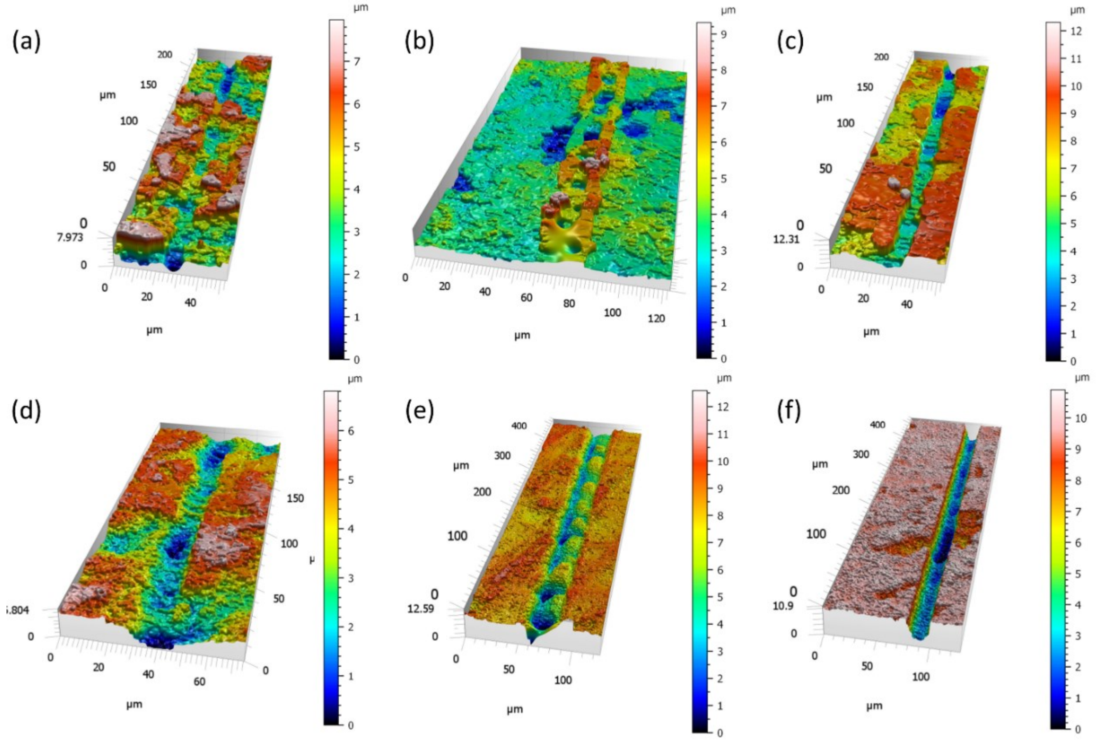

Source: Author.

Figure 3.5 shows the average depth and width of the grooves produced by the laser treatment on the 3Y-TZP for the different conditions tested. The depth is represented by the columns and the width by the scattered points. These geometric features were calculated based on the average depth and width of a region of 100 μm along the groove. Conditions that produced defects due to excessive energy are represented by the red patterned columns, while conditions that produced heterogeneous grooves due to insufficient energy are represented by the blue patterned columns. The numbers over the columns represent the accumulated fluence, in J/cm². The conditions that did not produce a continuous groove are not shown in the graphs, which means that energy levels below those shown in the graph did not produce a continuous groove, and energy levels above produced excessive remelting. Overall, good quality grooves were obtained for accumulated fluence between 2~17 J/cm², achieving depths up to 6 μm. Increasing the laser energy further can increase the depth (up to 17 μm in the tested conditions), but defects start to appear, as seen previously in Figure 3.2. For accumulated fluences in the optimal range, the quality of the grooves is highly dependent on the repetition rate and the scanning speed. For low repetition rates, as there is more time between subsequent pulses, more energy is necessary to ablate the material. For 1 kHz samples, even for an intermediate level of accumulated fluence (9.2 J/cm² at 10 mm/s), the groove is still incomplete, while at 10 kHz, for lower fluence and the same speed (6.3 J/cm² and 10 mm/s), a deep groove with signs of melting is produced. Regarding the scanning speed, lower speeds, i.e., a higher number of pulses hitting the same spot, result in lower quality grooves, with more melting and cracking. For example, at 10 kHz, the sample with accumulated fluence of 6.3 J/cm² at 10 mm/s presented melting, while increasing the speed to 50 mm/s, the groove quality is better even for higher fluence. Regarding the width of the ablated grooves, they ranged from 8 μm up to 16 μm, being directly related to the single pulse fluence. For example, for the speed of 50 mm/s and repetition rate of 10 kHz, increasing the fluence from 0.2 J/cm² to 3.1 J/cm² increases the width from 8 μm to 12.6 μm. On the other hand, the number of pulses, represented on the graphs by the accumulated fluence, had only a slight influence on the groove's width. This fact can be observed for the 100 kHz sample, where the width is almost constant for a pulse fluence of 0.2 J/cm², regardless of the laser speed and accumulated fluence, which changes from 3 J/cm² up to 600 J/cm².

Figure 3.5 - Average depth (bars) and width (points) of the ablated grooves for different values of repetition rate, fluence, and speed tested for the 3Y-TZP.

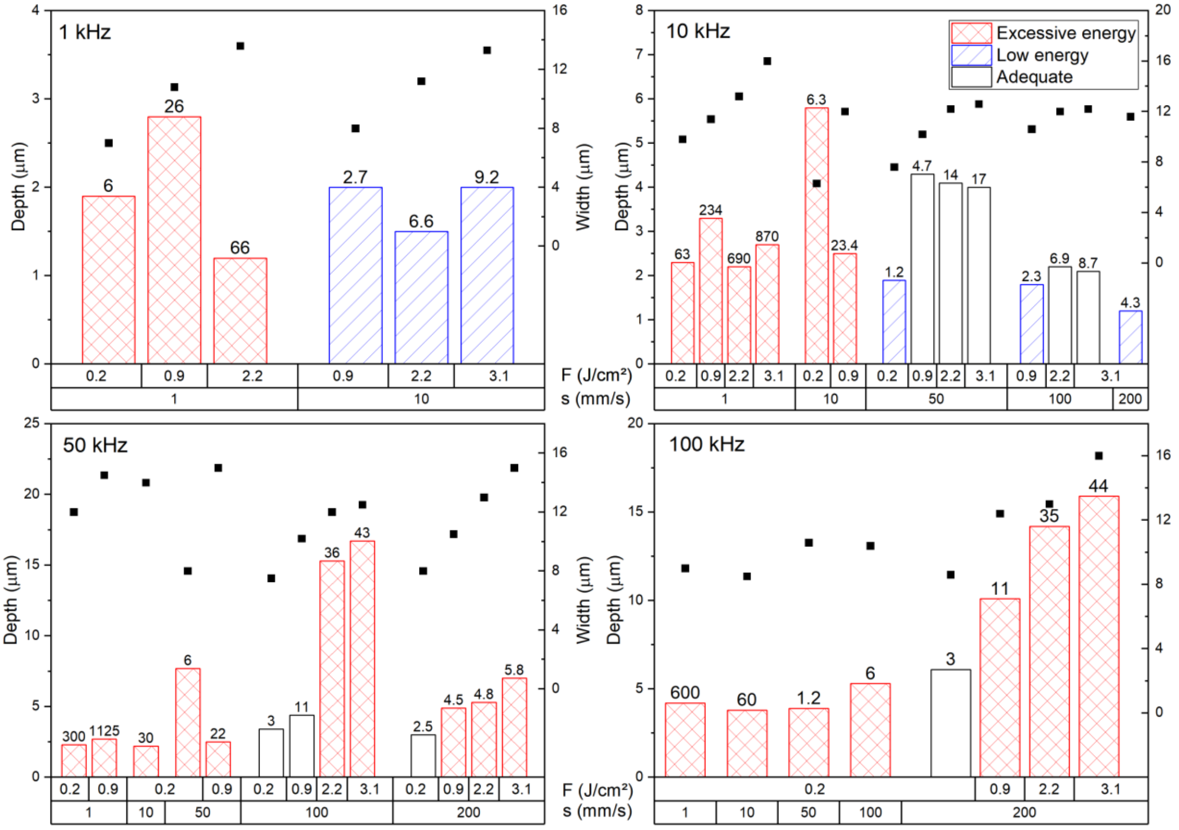

Source: Author.

Figure 3.6 shows the average depth and width of the grooves produced by laser processing for the $ZA_8Sr_8Ce_{11}$. The graphs' color and pattern follow the same scheme as Figure 3.5. As discussed earlier, although the composite has a higher ablation threshold than 3Y-TZP, it presents deeper and wider grooves when the threshold is exceeded, reaching depths up to ~26 µm and widths up to 30 µm for defect-free grooves. Overall, good quality grooves were achieved for accumulated fluence between 2 and 36 J/cm², depending on the laser speed and repetition rate. The relationships between groove quality and depth and laser parameters follow similar trends as the 3Y-TZP. For low frequencies, more energy is required to fully ablate the material, while for high frequencies, even low values of fluence can cause melting and cracking. However, laser processing of $ZA_8Sr_8Ce_{11}$ allowed the ablation of a wider range of depths (with different parameters) with no visible defects, varying from ~2 µm (1 kHz, 10 mm/s, 0.9 J/cm²) up to ~26 µm (50 kHz, 100 mm/s, 2.2 J/cm²). In general, $ZA_8Sr_8Ce_{11}$ was also less susceptible to melting and cracking for the same laser parameters. For example, the same conditions that produced the deepest good-quality groove on the composite (50 kHz, 100 mm/s, 2.2 J/cm²) generated a remelting layer and some microcracks on zirconia. Regarding the width of the grooves, the relation between fluence and width follows a similar trend as the 3Y-TZP, with wider grooves for high values of single pulse fluence. However, for the composite, the width also increases with the accumulated fluence. For example, for 100 kHz, the groove can reach ~70 µm wide for 0.9 J/cm² and 1 mm/s, while the same condition for 10 kHz, the groove is only 29 µm wide.

Figure 3.6 - Average depth (bars) and width (points) of the ablated grooves for different values of repetition rate, fluence, and speed tested for the $ZA_8Sr_8Ce_{11}$.

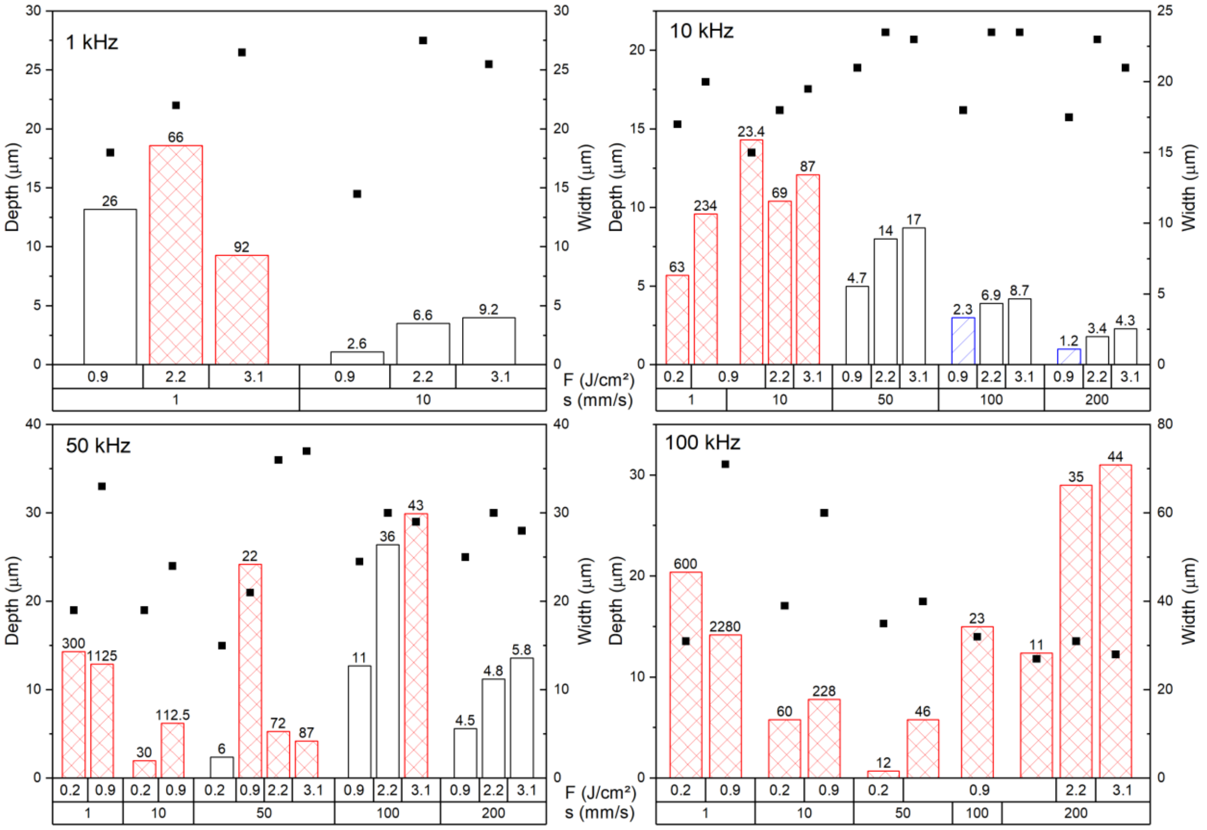

Source: Author.

Based on the transversal area and the laser speed, the removal rate, in mm³/s, for the conditions where good-quality grooves were achieved, could be calculated and it is shown in Figure 3.7(a) for the 3Y-TZP and Figure 3.7(b) for the $ZA_8Sr_8Ce_{11}$. As expected, the removal rate increases with higher values of fluence, laser speed, and repetition rate, regardless of the material. The 3Y-TZP presented a removal rate of up to 0.006 mm³/s, while the composite presented values up to 0.06 mm³/s when a high-frequency condition was used. Thus, for similar conditions, the composite presents a removal rate up to 10 times higher the conventional zirconia.

Figure 3.7 - Material removal rate, in mm³/s, for the conditions where good-quality grooves were achieved for (a) the 3Y-TZP and (b) $ZA_8Sr_8Ce_{11}$.

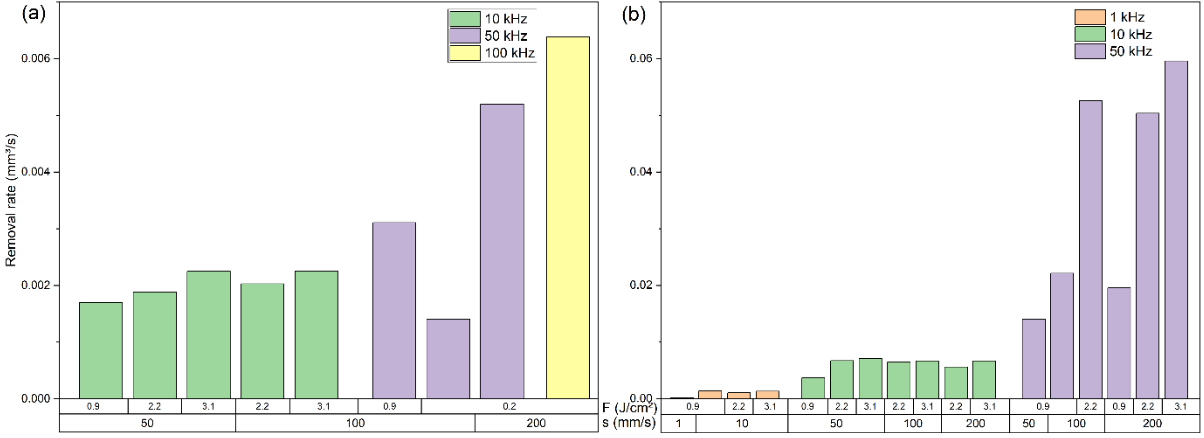

Source: Author.

3.5 DISCUSSION

In this study, grooves were successfully produced in both traditional 3Y-TZP and $ZA_8Sr_8Ce_{11}$ nanocomposite using direct laser writing (DLW) to ablate localized material, equipped with an ultra-short pulsed laser source (10 ps) working at a wavelength of 532 nm. The influence of different laser parameters, such as fluence, scan speed, and repetition rate, on the morphological, microstructural, and geometric features of the ablated grooves was successfully evaluated.

For most cases, the groove depth increased with an increase in the pulse fluence, repetition rate, and/or a decrease in scanning speed, i.e., any increase in the accumulated fluence. However, for large values of accumulated fluence, excessive remelting occurred, with material accumulating inside the grooves. This phenomenon can decrease the depth, as observed for the high repetition rate and low-speed conditions. The relationship between fluence and width observed in the results is due to the Gaussian nature of the laser beam. Increasing the pulse fluence increases the fraction of energy in the Gaussian beam that exceeds the ablation threshold, thus removing more material around the center of the beam and increasing the groove width (Ezhilmaran *et al.*, 2018). However, for some conditions, the groove width did not follow this trend, which could indicate that excessive heating had occurred, accumulating molten material inside the cavity and decreasing the width. Studies have shown that the optimal groove width for osteoblast cellular growth is around 30 µm (Delgado-Ruíz *et al.*, 2016; Webster, 2008), which is in line with the good-quality grooves produced for the composite. On the other hand, the 3Y-TZP presented smaller grooves, indicating that, for biological applications, it may need a different optical setup to achieve the optimal groove width, such as a top-hat beam profile (Bischoff *et al.*, 2019).

The scanning speed is directly related to pulse overlap (overlapping between subsequent pulses) and the average number of pulses hitting the same spot. When the repetition rate is fixed, decreasing the scanning speed results in more energy being applied to the same area, resulting, usually, in deeper grooves. However, for low values of speed (< 10 mm/s in this work), the energy density reaches an excessive level, leading to remelting and thermal damage. Regarding the groove width, the scanning speed did not significantly influence it, especially for 3Y-TZP. Han et al. showed similar results in their work, showing that increasing pulse energy increases both groove depth and width, but scanning speed only influences the depth (Han *et al.*, 2022b).

The repetition rate (number of pulses emitted per second) influences not only the number of pulses that hit the same area but also the rate of energy deposition. Lower repetition rates (< 10 kHz) are less efficient, since there is more time between pulses to dissipate heat, leading to less material being removed for the same level of energy. On the other hand, high repetition rates can lead to resolidification and thermal cracking, due to the accumulation of heat energy, as also seen in other works (Di Niso *et al.*, 2014; Salminen *et al.*, 2010). Thus, the repetition rate should be properly selected to allow good efficiency and productivity and, at the same time, yield a high level of precision and quality.

Under high repetition rates and/or low scanning speeds, when the number of pulses hitting the same spot is high, melting and resolidification occur. The resulting high accumulated fluence leads to an excessive increase in the surface temperature, melting the surrounding area of the irradiated region. The molten material, in the liquid phase, accumulates inside the grooves during the laser processing, preventing the penetration of the laser beam and, consequently, the material ablation (Cunha, Ângela *et al.*, 2022). Indeed, in the most aggressive conditions, molten material accumulated in the grooves, generating ridges instead of grooves.

The composite showed higher depth and width of the textured grooves compared to the monolithic 3Y-TZP. This resulted in a material removal rate up to 10 times higher for the composite. This fact can be explained by the thermal properties of both materials. Alumina has a higher thermal conductivity than zirconia, thus the heat applied by the laser pulse is distributed to the surrounding area, increasing the temperature of a larger area and ablating more material on the composite. Furthermore, the melting points of Al_2O_3 and $SrAl_{12}O_{19}$ are well below that of ZrO_2. This means that the energy required to ablate those materials through thermal mechanisms will be lower, resulting in more material removed (higher material removal rate) for the same level of energy for the composite. On the other hand, 3Y-TZP presented a lower ablation threshold than the composite, with grooves being ablated for lower values of fluence. As stated before, 3Y-TZP has lower heat conductivity than the composite, thus the energy imposed by the laser beam concentrates in a smaller region, which can generate a higher temperature peak than the composite, leading to an earlier ablation. However, the ablation threshold can be also influenced by other material properties, such as the band gap, which determines the laser energy absorption, and the presence of defects on the microstructure. Defects, such as pores, impurities, and grain boundaries, increase the laser absorption, thus they could reduce the ablation threshold (Armbruster; Naghilou; Kautek, 2018). Han et al., who used a femtosecond laser to ablate zirconia and alumina/zirconia composites, attributed the lower ablation threshold of the composites to the higher presence of defects, especially at the grain boundaries (Han *et al.*, 2022a). These contradictions show that the ablation threshold of a material is a complex phenomenon that depends on several thermal and electronic properties of the material, as well as its composition and microstructure. Moreover, for multi-pulse laser ablation (speed < 20 mm/s and/or repetition rate ≥ 10 kHz), the ablation threshold is decreased due to a cumulative effect of the laser-induced thermal energy. Further research should be conducted to understand the relationship between laser threshold ablation and material composition, especially for composites, and how it correlates to the material removal rate.

Laser texturing of zirconia has been extensively studied in the last few years, with different results depending mainly on the pulse duration. For example, Hirota et. al. used a nanosecond laser to texture 3Y-TZP and a Ce-TZP aluminum oxide nanocomposite. In their work, the grooves were successfully ablated, however, signs of melting and oxygen depletion were present, probably due to high heating imparted by the nanosecond laser (Hirota *et al.*, 2019). Indeed, probably due to the oxygen depletion, the surface of the Al_2O_3/Ce-TZP became black. For a more aggressive condition, using a microsecond laser, the damages are even more intense, with the formation of microcracks as well as oxygen depletion and intense melting, for both 3Y-TZP and Al_2O_3/Ce-TZP composite (Noda *et al.*, 2010). High heating from longer pulsed lasers can also cause resolidification and growth of columnar grains parallel to the temperature gradient, which facilitates crack growth towards the material bulk (Dear *et al.*, 2008). Although oxygen depletion can be restored by heating the sample in air, the other defects remain on the material, which is very likely to substantially decrease its mechanical strength. In our work, for the optimal conditions, cracking and melting were not observed. These differences observed in the morphological and structural characteristics of each work can be related to the laser-matter interaction principles behind the pulse duration. For ultrafast laser ablation, the process is based on the surface ionization caused by the very short and intense pulses, resulting in a local transformation of the material into a plasma, which can remove atoms from the solid. This mechanism is called Coulomb explosion and, since the material is removed before any transfer of energy to the surroundings, it is a nonthermal process (Delgado-Ruíz *et al.*, 2011; Wang *et al.*, 2008). However, as the fluence or number of pulses increases, more energy is absorbed by the ionized surface, which can increase the temperature of a deeper surface layer, resulting in a thermal process of phase-explosion, that can lead to defects such as melting and cracking, as observed for the high energy conditions of this work. For longer pulse duration (ns and ms), the lower power and the longer beam-mater contact time cause more energy to be dissipated in the surface before sufficient intensity is reached to generate the surface ionization, favoring the occurrence of melting rather than ablation. The improvement in the surface quality is also reported by other works that used ultra-short pulsed laser to texture zirconia (Delgado-Ruíz *et al.*, 2011; Han *et al.*, 2022a; Parry *et al.*, 2011).

The morphology of the structured grooves, as shown in the SEM micrographs in Figure 3.2 and Figure 3.3, reveals some porosity within the ablated areas, especially for the composite. As the samples were almost fully densified during sintering, these pores can be attributed to the laser treatment, rather than to porosity already present in the bulk material. The mechanism behind the occurrence of porosity can be related to localized explosive vaporization events or localized ablation, which might originate from the inhomogeneity in the bulk material or even localized ablation of the phases with a lower ablation threshold (Müller *et al.*, 2020).

Another concern regarding the laser treatments of zirconia is the possible monoclinic to tetragonal phase transformation due to the heat stresses and strains. However, for fast and ultra-fast pulsed lasers, studies have shown that this phenomenon is not significant, with very little phase change after the laser treatment (Han *et al.*, 2022a; Henriques *et al.*, 2018b). Indeed, laser-treated samples can show even lower monoclinic content than samples treated with the conventional sandblasting technique (Faria *et al.*, 2020).

3.6 CONCLUSION

In this study, laser ablation of 3Y-TZP and the composite $ZA_8Sr_8Ce_{11}$ using a Direct Laser Writing system equipped with an ultra-short pulsed laser (10 ps) working at a wavelength of 532 nm was investigated. The influence of laser pulse energy, pulse repetition rate, and scanning speed on the ablated grooves profile and morphology for both materials was analyzed. The following conclusions can be drawn from this study:

- Both materials can be successfully ablated with almost defect-free and well-defined grooves with a proper selection of laser parameters. On the other hand, insufficient laser energy creates irregular shallow grooves, and excessive energy results in remelting and cracking.
- Fluence, repetition rate, and scan speed can be adjusted to achieve different groove geometry (depth and width). However, the parameters should be carefully chosen to avoid defects.
- The $ZA_8Sr_8Ce_{11}$ composite allowed the fabrication of wider and deeper grooves (up to 30 μm wide and 26 μm deep) using laser texturing in comparison with the traditional 3Y-TZP (up to 12 μm wide and 6 μm deep), resulting also in a material removal rate up to 10 times higher for similar laser parameters.
- These results provide optimistic perspectives on the fabrication of micro-textures of this novel composite that can be further explored to functionalize its surface for biomedical applications, for example.

4 HIGH THROUGHPUT NANOSECOND DIRECT LASER INTERFERENCE PATTERNING OF ZIRCONIA AND ZIRCONIA-BASED COMPOSITE

4.1 ABSTRACT

This work aimed to create micrometric textures on the surface of traditional zirconia and a novel zirconia-based nanocomposite using Direct Laser Interference Patterning (DLIP) and to evaluate their topography, microstructure, wettability, and biological behavior. A nanosecond laser system with a DLIP optical head was employed to produce line-like patterns with a 6 μm periodicity on 3Y-TZP and Ce-TZP/Al_2O_3/$SrAl_{12}O_{19}$ composite using different laser parameters. Confocal Microscopy and Scanning Electron Microscopy were used to analyze the resulting topographies. The effects of laser patterning on surface crystallography, wettability, and biological behavior were also investigated. By adjusting the laser parameters, micropatterns were successfully fabricated on both materials. However, some thermal ablation defects, such as melting, porosity, phase transformation (from tetragonal to monoclinic), and cracking, were observed on the surface. Wettability was enhanced by the laser texturing. Preliminary biological tests indicated that cells grew along the direction of the patterns. These outcomes open new perspectives on the functionalization of zirconia and zirconia-based composites for biological applications using DLIP.

4.2 INTRODUCTION

Zirconia (ZrO_2) has been attracting significant attention in several engineering applications due to its distinct properties, such as high strength, hardness, wear and high-temperature resistance, and biocompatibility. This combination of properties makes it suitable for various high-performance applications, especially in the biomedical field, such as dental implants and joint replacements (Bona; Pecho; Alessandretti, 2015; Chevalier; Gremillard, 2017). Among the different types of zirconia, Tetragonal Polycrystalline Zirconia stabilized with 3% mol of yttria (3Y-TZP) is preferred for orthopedic and dental applications because of its excellent flexural strength (up to 1200 MPa). However, 3Y-TZP is susceptible to low-temperature degradation (LTD), which is a spontaneous phase transformation (from tetragonal to monoclinic) induced by the presence of water, which compromises its mechanical strength in the long term (Lughi; Sergo, 2010). Moreover, 3Y-TZP has a moderate toughness value (6 MPa·√m), which means it is sensitive to the presence of defects, such as pores and cracks, that can significantly affect its mechanical resistance. Therefore, novel zirconia compositions and composites are being developed to improve their mechanical properties and broaden their biomedical applications. For example, zirconia stabilized with ceria (Ce-TZP) present values of toughness up to 20 MPa·√m and significantly reduced susceptibility to LTD (Kohorst *et al.*, 2012). Adding secondary phases to Ce-TZP, such as alumina and aluminate, can further decrease the zirconia grain size and provide an additional toughening mechanism, resulting in nanocomposites with high strength, high toughness, and negligible susceptibility to LTD (Reveron *et al.*, 2017).

The surface characteristics of biomaterials, such as roughness and hydrophilicity, play a crucial role in their biocompatibility and osseointegration. Therefore, researchers are devoting significant efforts to modify their surface and enhance their biological response and adhesion to other materials (Schünemann *et al.*, 2019). Conventional surface treatments, such as machining, grit blasting, and acid etching, aim to increase the surface roughness of implants to improve their mechanical interlocking with the bone/other materials (Buser *et al.*, 1991). However, these treatments can only create random patterns with limited dimensional control. In recent years, laser surface treatments have emerged as a precise and versatile approach for modifying biomaterial surfaces, allowing the fabrication of features with resolution down to an order of a few micrometers. In this process, a laser beam is focused on the workpiece with sufficient energy to remove localized material by melting, dissociation, and/or evaporation (Samant; Dahotre, 2009). Among the laser texturing techniques, a novel process called Direct Laser Interference Patterning (DLIP) has been showing exciting results in the fabrication of controlled periodic micro- and nanotopographies taking advantage of the light interference phenomenon (Guenther *et al.*, 2016; Lasagni *et al.*, 2017). In the DLIP method, the laser beam is split into two or more sub-beams that are superposed on the material surface, forming an interference pattern where the material is ablated at the maxima regions. As the interference pattern's periodicity depends on the laser wavelength and the angle between the sub-beams, features on the sub-micrometer range can be created. By changing these parameters, as well as others, such as laser fluence, number of sub-beams, and polarization, a wide variety of surface topographies can be achieved, including different periodicities, groove depths, and spatial arrangements.

DLIP has been successfully applied in zirconia (Y-TZP and Y-FSZ) to produce controlled microtopographies (Fabris *et al.*, 2019). However, the studies indicate that the laser parameters need to be carefully chosen to avoid surface damage, such as porosity, cracking, and melting. Daniel et al. showed the feasibility of structuring zirconia (Y-FSZ) using DLIP with a UV nanosecond laser. However, in their results, defects related to overheating of the surface, especially porosity and excessive melting, were observed. (Daniel *et al.*, 2008). Roitero et al. also used a UV nanosecond laser to texture 3Y-TZP using the DLIP technique. However, they reported intergranular cracking, directional crystallization, and phase transformation from tetragonal to monoclinic, which reduced the zirconia's mechanical strength (Roitero *et al.*, 2017b, 2018a). Müller et al., on the other hand, used a femtosecond laser to apply the DLIP technique on zirconia, achieving a higher-quality surface, with well-defined grooves. Nevertheless, microcracking and porosity were still present in the ablated areas (Müller *et al.*, 2020). No previous work has used DLIP to texture zirconia-based composites.

This study aims to explore the use of DLIP to produce a controlled micrometric surface pattern on traditional 3Y-TZP and the novel zirconia-based nanocomposite Ce-TZP/Al_2O_3/$SrAl_{12}O_{19}$ using a short-pulsed laser. The effect of laser fluence on the morphology and microstructure of the textured surface was examined for both materials. Moreover, wettability and biological tests were conducted to assess the surface behavior after laser texturing.

4.3 MATERIALS AND METHODS

4.3.1 Substrates fabrication

Commercial powder of zirconia stabilized with 3 mol% yttria (TZ-3YSB Tosoh, Japan) and powder of Ce-TZP/Al_2O_3/$SrAl_{12}O_{19}$ (composition: 84 vol% ZrO_2 (stabilized with 11 mol% CeO_2), 8 vol% Al_2O_3 and 8 vol% $SrAl_{12}O_{19}$; DOCERAM, Germany) were used. For simplicity, the composite will be referred to as $ZA_8Sr_8Ce_{11}$ from now on. The powders were uniaxially pressed in steel dies into discs at a pressure of 100 MPa (3Y-TZP samples) and 70 MPa (composite samples) for 60 s to obtain the green compacts. Then, the 3Y-TZP samples were sintered at 1500 °C for 2h (3Y-TZP) and 1450°C for 1h ($ZA_8Sr_8Ce_{11}$) in a high-temperature furnace (Sinter F-1800 10P, EDG) in air. After sintering, the samples were sanded and polished (down to a grit size of 1 μm diamond particles) to achieve a flat and mirror-like surface. The discs had a final dimension of 16.9 mm in diameter and 1.6 mm thick.

4.3.2 Laser texturing

The laser texturing process was performed using the Direct Laser Interference Patterning (DLIP) method, as illustrated in Figure 4.1. A nanosecond slab-shaped solid-state laser source (Edgewave InnoSlab – IS400–3-GH, Würselen, Germany) with a wavelength of 1064 nm, a pulse width of 10 ns and a maximum output power of 150 W was used in the DLIP system. The repetition rate was fixed at 5 kHz. The DLIP optical head (Fraunhofer IWS/TU Dresden, Germany) splits the laser beam into two symmetrical sub-beams using two prisms, and then overlaps and focuses them on the sample surface with a cylindrical lens (Figure 4.1(a)). This optical setup also elongates the beam geometry, producing a rectangular spot size at the focus position with dimensions of 100 μm in the Y-direction and 5 mm in the X-direction. This optical setup allows a high throughput processing (Lang; Voisiat; Lasagni, 2019). A line-like periodic profile is obtained by using this configuration (Figure 4.1(b)). The periodicity Λ of the pattern (distance between consecutive lines) correlates to the half angle between the sub-beams θ (Figure 4.1(b)) and the laser wavelength λ and it can be calculated according to Equation 4.1. The angle between beams was approximately 10.2° (θ = 5.1°) in this work, resulting in a periodicity of 6 μm.

$$\Lambda = \frac{\lambda}{2\sin\theta} \tag{4.1}$$

High-precision positioning axes (Aerotech, USA) were used to translate the sample relative to the laser beam in the x- and y-directions to structure larger areas, as shown in Figure 4.1(c). The pulse-to-pulse distance (PtPd), which is the distance between two consecutive pulses, controls the movement in the y-direction. The sample also moves in the x-direction by the Hatch distance (Hd), which is the distance between two consecutive lines, to texture larger areas. The PtP_d and H_d also determine the number of pulses hitting the same position, as they can be expressed in terms of pulse overlap. From preliminary tests, the PtP_d was set as 2.5 μm for both materials, and the H_d was 1.36 mm for the 3Y-TZP and 1.59 mm for the $ZA_8Sr_8Ce_{11}$. The texturing strategy consisted firstly of patterning single lines (moving the sample only in the y-direction) and varying the laser fluence between 1.67 J/cm² and 2.72 J/cm² for the 3Y-TZP and 0.65 J/cm² and 1.82 J/cm² for the $ZA_8Sr_8Ce_{11}$. The textured lines were analyzed in terms of morphology and topography. Based on these results, entire areas were textured and subjected to further tests.

Figure 4.1 - (a) Optical setup used on the direct laser interference patterning system; (b) interference pattern created when the two sub-beams overlap with half-angle θ; (c) texturing strategy: the sample is moved on the y-direction by the set pulse-to distance (PtP_d) to texture a line, then the sample is moved on the x-direction by the hatch distance (H_d).

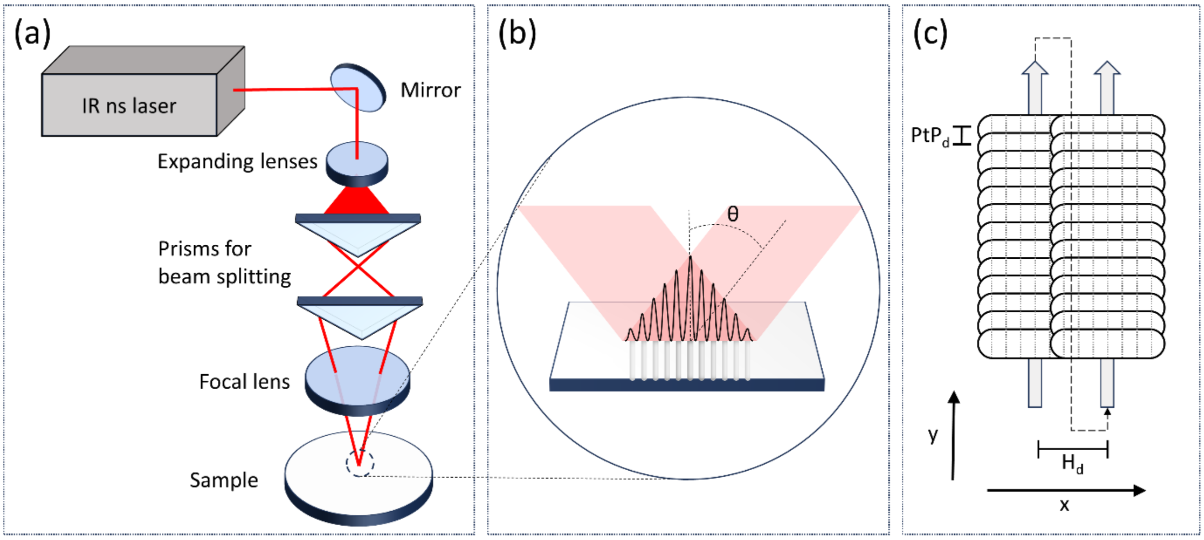

Source: Author.

4.3.3 Morphology and Topography Analysis

The topography of the textured surfaces was analyzed using a confocal microscope (S Neox, Sensofar) equipped with 50x and 150x objectives. The software SensoMAP (Sensofar) was used to process and analyze the topographical data. The morphology and microstructure of the samples were analyzed using a Scanning Electron Microscope (TM3030, Hitachi) at an operating voltage of 15.0 kV.

4.3.4 Crystallographic analysis

The crystallographic phases of the 3Y-TZP and $ZA_8Sr_8Ce_{11}$ before and after laser texturing were determined by X-ray diffraction (XRD) using a Cu-Kα source (Rigaku Miniflex 600). The XRD spectra were obtained over a 2θ range between 10° and 80° with a step size of 0.05° and a scan speed of 5°/min. The main purpose of this analysis was to evaluate the transformation of the metastable tetragonal phase into monoclinic. Therefore, only the fraction between these two phases was calculated, using the Toraya equation (Toraya; Yoshimura; Somiya, 1984).

4.3.5 Wettability

The static water contact angle (WCA) of the textured and polished samples was measured using a drop shape analyzer (Krüss DSA100S) with 4 µl droplets of deionized water placed at the center of each sample. The tangent fitting method was used to calculate the contact angles of the sessile droplets, and the reported values are the average of 9 measurements. WCA was measured both perpendicular and parallel to the textured grooves. The samples were cleaned using compressed air before and between measurements.

4.3.6 Biological analysis

The polished and textured samples of both materials (3Y-TZP and $ZA_8Sr_8Ce_{11}$) were subjected to preliminary biological tests to evaluate their biological behavior and cell growth on different surfaces. One sample of each group was used for the test. The samples were placed in a 12-well plate and sterilized under UV light for 1 h on each side before the experiment. MC3T3-E1 preosteoblast cell line was cultured in cell culture polystyrene flasks using MEM α (Minimum Essential Medium α) supplemented with 10 vol. % fetal bovine serum (FBS; Sigma-Aldrich) and 1 vol. % penicillin/streptomycin (Pen-Strep; Sigma-Aldrich). The cells were incubated at 37°C with a humidified atmosphere of 5% CO_2 until the confluency reached 70-80%. The old medium was discarded, and the cells were washed with phosphate buffer saline (PBS; Gibco). Afterward, trypsin (Life Technology) was used to detach cells from the flask wall. Upon cell detachment, trypsination was inactivated by adding fresh MEM α, and the cell suspension was counted in a hemocytometer by trypan blue exclusion method (Sigma-Aldrich, Germany). The sterilized samples were seeded with 25000 cells each. The cells were grown on the zirconia, composite, and control samples (well plate) for 48 h at 5% CO_2 and 37 °C.

After the specified time interval, cell viability was assessed by using water-soluble tetrazolium salt (WST-8 assay, Sigma Aldrich). WST-8 solution (1 vol%) in MEM α was prepared and added to each type of sample. Optical absorbance was recorded at 450 nm after 4 h of incubation with WST-8.

For the fluorescence microscopic analysis, cells were stained by using Calcein AM (Life Technologies) and DAPI (4',6-diamidino-2- phenylindole) (ThermoFisher, Schwerte, Germany). Calcein AM was prepared in MEM α at a concentration of 4 µL/mL, whereas 1 µL/mL DAPI (4',6-diamidino- 2-phenylindole) was prepared in PBS solution. Before addition of DAPI, cells were fixed by using a fixing solution composed of 1 mM EGTA (Ethylene glycol tetra-acetic acid, Merck, Darmstadt, Germany), 4% (w/v) polyethyleneglycol, 3.7% (w/v) paraformaldehyde (all Sigma Aldrich, Taufkirchen, Germany) and 0.1 M PIPES (Piperazine-N, N'-bis (2- ethanesulfonic acid), Merck, Darmstadt, Germany), dissolved in PBS.

4.4 RESULTS

4.4.1 Single lines texturing

Figure 4.2 shows SEM images of the topography for different values of fluence of the DLIP patterned 3Y-TZP (Figure 4.2(a-c)) and $ZA_8Sr_8Ce_{11}$ (Figure 4.2(d-f)) samples. Periodic line-like structures with a 6 μm period were successfully fabricated for both materials, but their quality and homogeneity depended on the laser fluence. For low values of fluence (e.g., 1.67 J/cm² for 3Y-TZP (Figure 4.2(a)) and 0.65 J/cm² for $ZA_8Sr_8Ce_{11}$ (Figure 4.2(d))), incomplete structures were fabricated, as ablation did not occur over the entire surface. The lower ablation threshold of the composite than the traditional zirconia for multi-pulse ablation can also be inferred from these values of fluence. The pattern was more homogeneous and the periodic distribution of grooves and ridges was clearly visible for moderate levels of fluence, as shown in Figure 4.2(b) and Figure 4.2(e), which correspond to fluences of 2.18 J/cm² and 1.38 J/cm², respectively. For high levels of energy, thermal defects, especially melting, were more evident. For 3Y-TZP at a fluence of 2.72 J/cm², the high heat generated by the ns laser melted the ridges, which solidified inside the grooves, as shown in Figure 4.2(c). Melting and pore formation were also observed for the composite at a fluence of 1.67 J/cm² (Figure 4.2(f)). The material was also ablated from the ridges (at the interference minima) for both materials and all fluences, indicating high heat transfer from the grooves (interference maxima positions) to the surroundings.

Figure 4.2 - Microstructure of the laser textured samples of 3Y-TZP with a fluence of (a) 1.67 J/cm², (b) 2.18 J/cm², and (c) 2.72 J/cm² and $ZA_8Sr_8Ce_{11}$ with (d) 0.65 J/cm², (e) 1.38 J/cm², and (f) 1.67 J/cm².

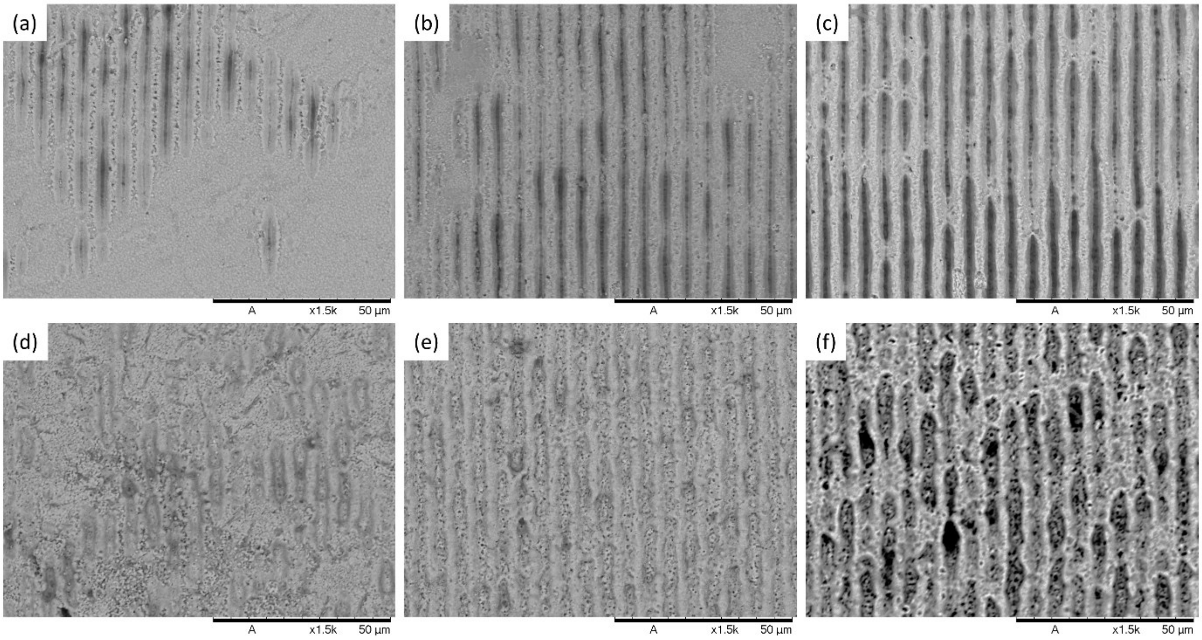

Source: Author.

The average depths of the fabricated grooves for single lines are shown in Figure 4.3. The average depth increased with the fluence of the traditional zirconia. For example, the average depth was 1.4 ± 0.8 µm for 1.67 J/cm², and it increased to 3.2 ± 0.9 µm for 2.72 J/cm². For moderate values of fluence, where fairly homogeneous surfaces were textured, the average depth was approximately 2.0~2.5 µm. A high standard deviation on the depths indicated heterogeneities due to incomplete ablation or resolidified material. Despite the lower ablation threshold, the depths found for the $ZA_8Sr_8Ce_{11}$ composite were mainly lower than the 3Y-TZP. For low fluence (0.65 J/cm²), the average depth was 0.6 ± 0.5 µm, and it increased to 1.4 ± 0.5 µm for a fluence of 1.22 J/cm². For moderate values of fluence, the depths were around 1.0~1.5 µm. However, the average depth decreased with a further increase in fluence, probably due to the melting observed on the SEM images. For example, the average depth was 0.8 ± 0.6 µm when the fluence was 1.82 J/cm². A large standard deviation in the depths was also observed for the composite.

Figure 4.3 - Average depths of the textured grooves when the samples were translated only in the y-direction.

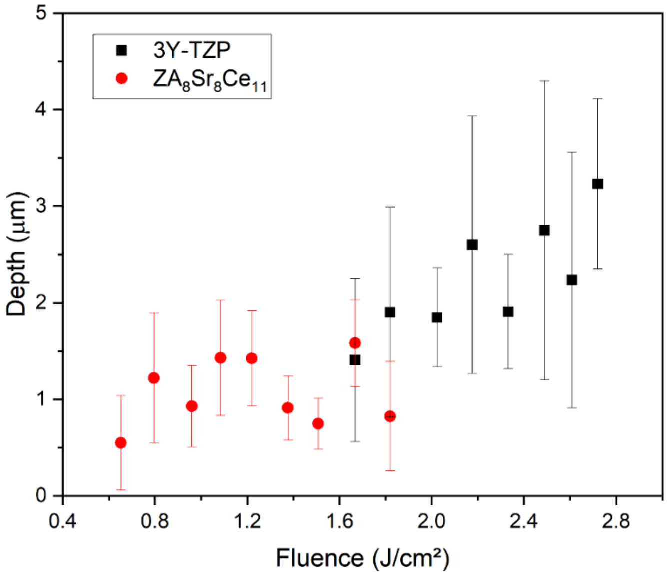

Source: Author.

4.4.2 Area texturing

For the fabrication of larger areas, to texture the entire surface of the samples, several tests were performed varying the values of fluence between 1.08 J/cm² and 1.38 J/cm² and hatch distance (hatch overlap) between 2.065 mm (58.7%) and 0.885 mm (82.3%) for the composite and between 1.82 J/cm² and 2.18 J/cm² and 2.36 mm (52.8%) and 1.18 mm (76.4%) for the 3Y-TZP. The surfaces were successfully textured using all these conditions, presenting similar topography. However, low values of fluence and/or hatch overlap resulted in heterogeneous structures, with regions with more ablation than others, and high fluence and/or hatch overlap caused excessive melting. Therefore, a single condition that resulted in a homogeneous surface was chosen for each material for further tests and analyses. The chosen condition for the $ZA_8Sr_8Ce_{11}$ was a fluence of 1.38 J/cm² and a hatch distance of 1.59 mm (68.1%), and the chosen condition for the 3Y-TZP was a fluence of 2.18 J/cm² and a hatch distance of 1.36 mm (72.9%). The topographies of these conditions are shown in Figure 4.4. The traditional zirconia (Figure 4.4(a) and Figure 4.4(b)) presented a well-defined structure but with thermal defects, such as melting and pores. Similarly, the composite (Figure 4.4(c) and Figure 4.4(d)) also showed a well-defined structure with signs of melting and some porosity. Moreover, cracking was observed in the texture area, as highlighted in Figure 4.4(d), which indicates critical thermal stresses developed during the laser processing.

Figure 4.4 - SEM micrographs of the area textured samples of (a,b) 3Y-TZP with 2.18 J/cm^2 of fluence and hatch distance of 1.36 mm and (c,d) $ZA_8Sr_8Ce_{11}$ with 1.38 J/cm^2 and 1.593 mm. The arrow indicates microcracking.

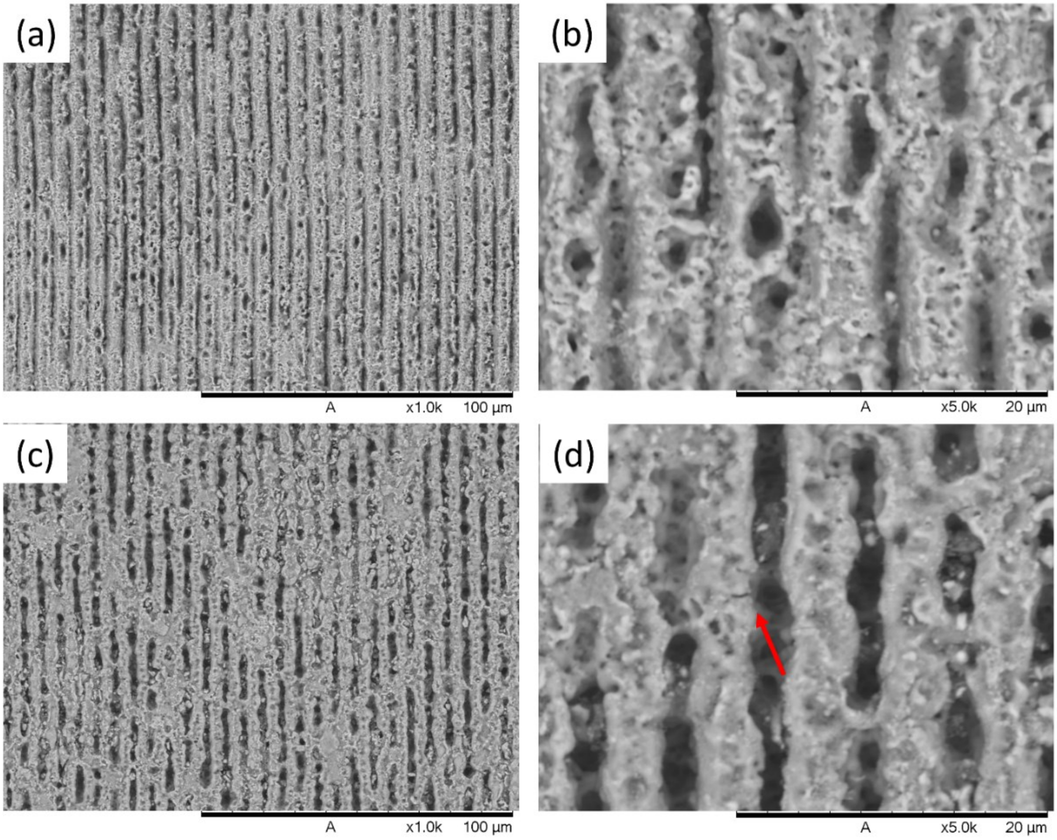

Source: Author.

The topographical data acquired by the confocal microscope, along with a 2D orthogonal profile, is shown in Figure 4.5 for both materials. The 3D images corroborate with the SEM analysis showing that texturing using DLIP can be achieved in 3Y-TZP and $ZA_8Sr_8Ce_{11}$ with a nanosecond laser. However, the images also showed the deleterious effects of the generated heat. On the 3Y-TZP (Figure 4.5(a)), heterogeneity in the depth of the grooves can be noticed, varying from ~100 nm up to more than 1 µm. Some regions also had larger heights on the ridges, which could indicate the accumulation of resolidified material. Similar heterogeneities were found on the composite (Figure 4.5(b)), with groove depths ranging from ~200 nm to 3 µm. The high melting of the composite can also be observed on the confocal images, which showed that the periodic pattern cannot be observed in some regions due to the accumulation of resolidified material inside the grooves. The analyzed surfaces of the traditional zirconia had an average depth of features of 0.78 ± 0.32 µm and roughness (Sq) of 750 nm and the composite presented an average depth of 0.83 ± 0.42 µm and roughness (Sq) of 750 nm. The depth values were much lower than those of single-line texturing, indicating that multi-pass laser tends to ablate more the ridges, decreasing the overall depth of the features.

Figure 4.5 - Topography and orthogonal profile of the area textured samples of (a) 3Y-TZP with 2.18 J/cm² of fluence and hatch distance of 1.18 mm and (b) ZA$_8$Sr$_8$Ce$_{11}$ with 1.38 J/cm² and 1.593 mm.

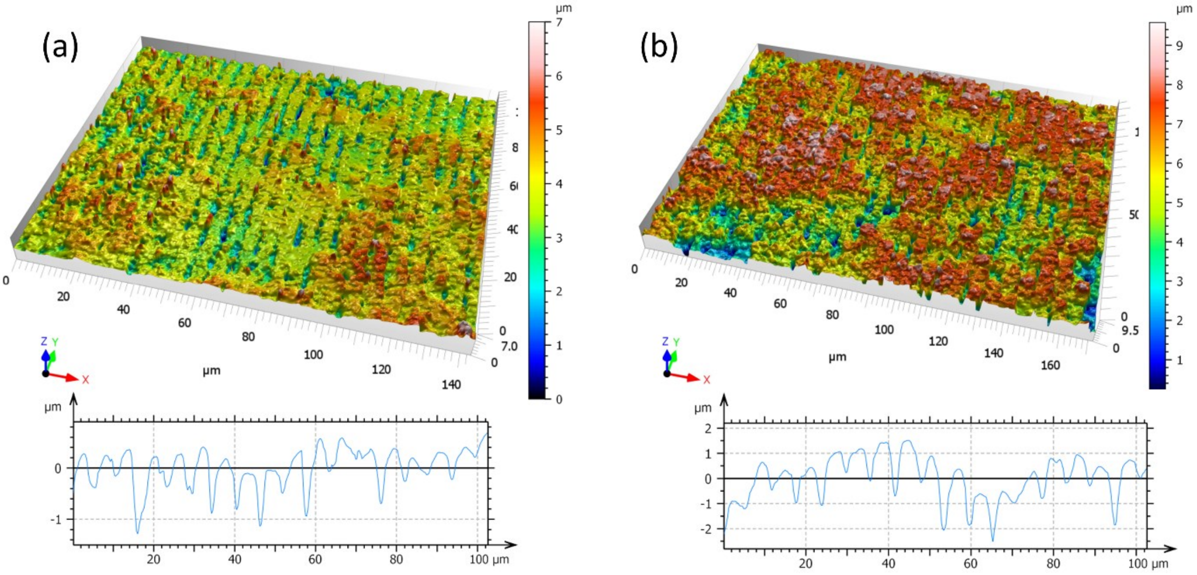

Source: Author.

4.4.3 Crystallographic analysis

The X-ray diffractograms for the zirconia and composite, before and after laser texturing, are shown in Figure 4.6. The letters t and m indicate peaks relative to the tetragonal and monoclinic phase, respectively. While the polished 3Y-TZP sample presented only the tetragonal phase, the textured sample presented small peaks related to the monoclinic phase at 28° and 31°. The Toraya equation revealed that the monoclinic content after laser texturing is 5.5%. On the other hand, the polished samples of ZA$_8$Sr$_8$Ce$_{11}$ showed a monoclinic content of 9.7%, which decreased to only 1.2% after the laser texturing.

Figure 4.6 - X-ray diffractometry of the polished and laser-textured samples for both materials.

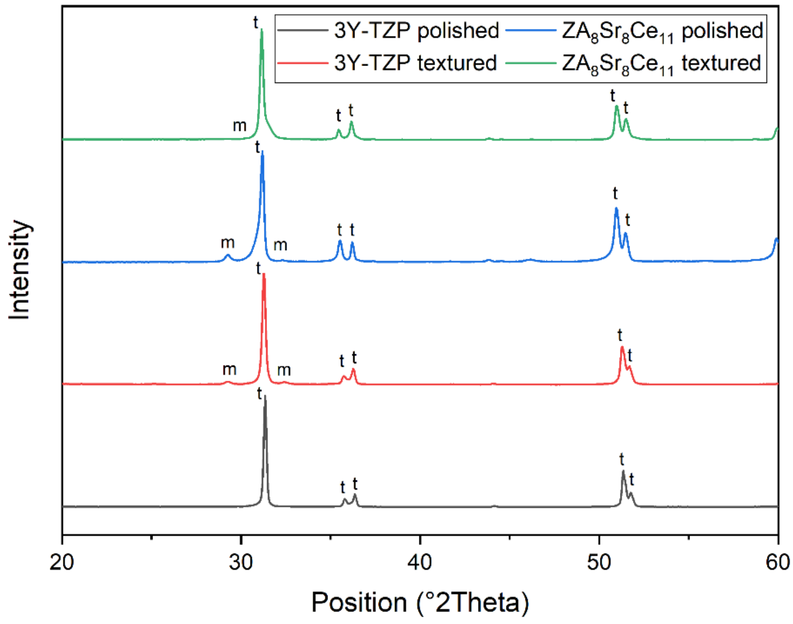

Source: Author.

4.4.4 Wettability

The wettability of the textured samples was evaluated by measuring the water contact angle (WCA) using a Drop Shape Analyser. The WCA measurements were conducted at 1, 10, and 30 days after laser texturing to examine the temporal variation of wettability. Due to the anisotropic properties of the surface, WCA was measured parallel and perpendicular to the textured lines. Figure 4.7 shows the measured WCA values and illustrates the parallel and perpendicular directions on the top-right corner. The polished samples of conventional zirconia and composite presented WCA values of 90.4 ± 2.0° and 84.9 ± 5.1°, respectively, as indicated by the blue and green dashed horizontal lines on the graph. Immediately following texturing, the WCA of both materials decreased significantly, indicating that the surface became hydrophilic. The parallel direction had a slightly lower WCA than the perpendicular direction, especially for 3Y-TZP. A small increase in WCA was observed for all sample groups after 10 days. However, after 30 days, the parallel direction of 3Y-TZP showed a significant increase in WCA, while the other groups had a larger standard deviation and no significant difference from the 10-day measurements. The two materials did not show any significant difference in WCA.

Figure 4.7 - Water contact angle assessed 1, 10, and 30 days after the laser texturing parallel and perpendicular to the grooves. The illustration on the top-right corner shows the parallel (top) and perpendicular (bottom) direction of analysis.

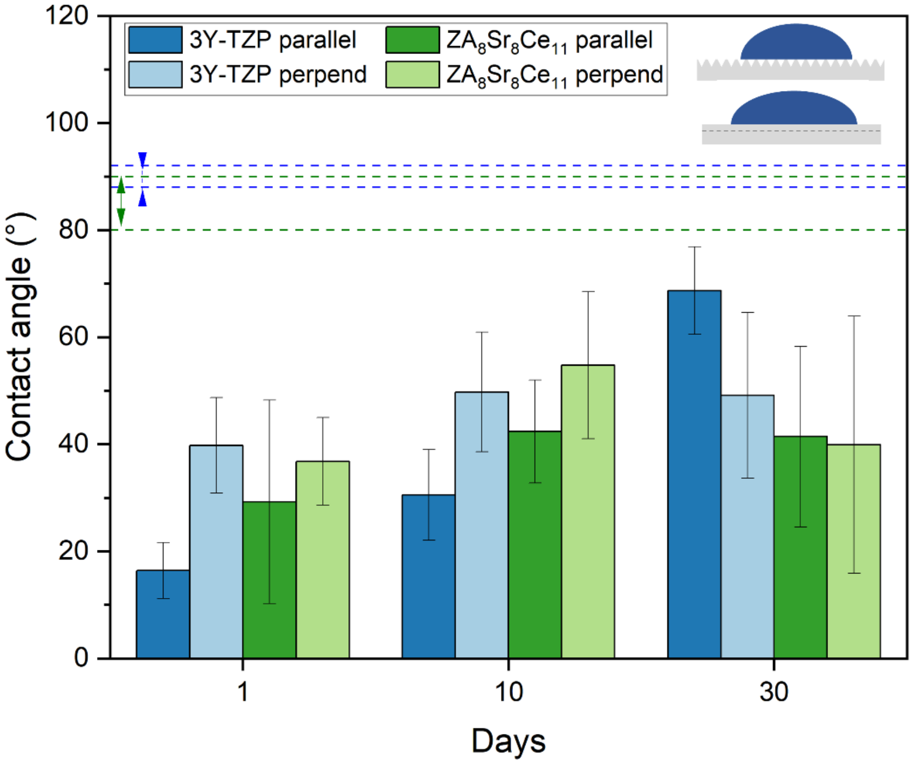

Source: Author.

4.4.5 Biological analysis

Biological tests were performed to assess cell viability after 48 h using a WST-8 solution. All samples exhibited similar cell viability (Figure 4.8). However, the limited number of samples (one per group) prevented the application of Bonferroni or Tukey post hoc tests for statistical comparison. Therefore, further studies with more samples are suggested to evaluate the cell proliferation rates at different time intervals.

Figure 4.8 - Cell viability of MC3T3-E1 cells treated with different investigated samples after 48 h in culture.

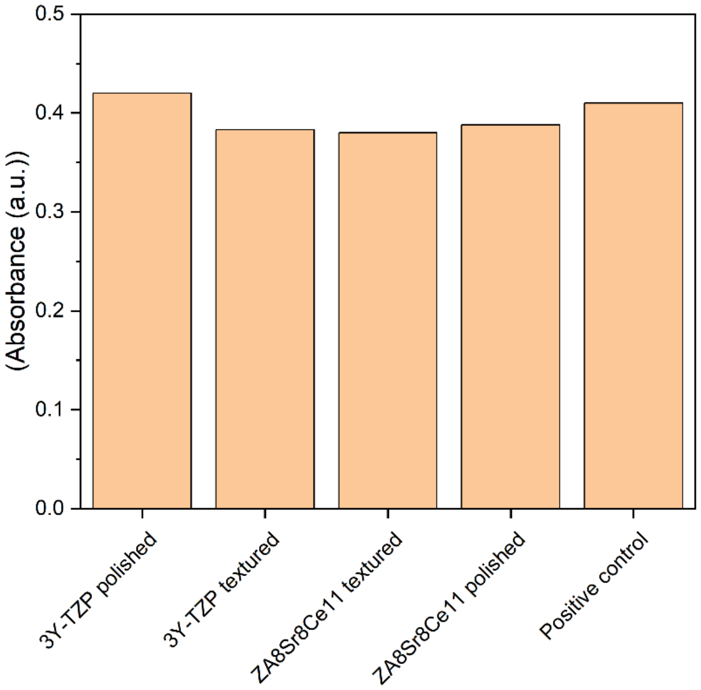

Source: Author.

Moreover, the influence of textured surfaces on the direction of cellular growth was investigated using fluorescence microscopy. The results showed that cells aligned with the grooves on the textured surfaces (Figure 4.9).

Figure 4.9 - Fluorescence microscope images of textured (a) 3Y-TZP and (b) $ZA_8Sr_8Ce_{11}$.

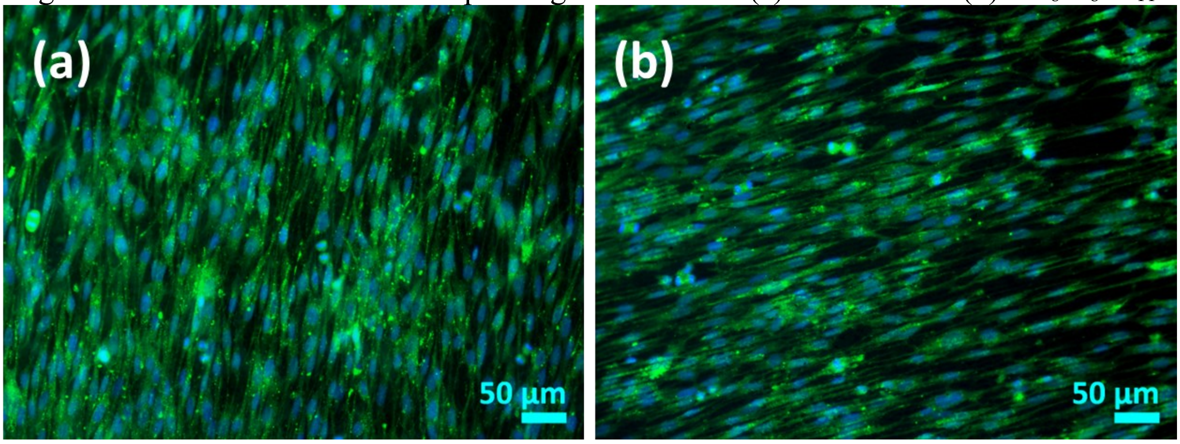

Source: Author

However, on polished samples (Sample 1 and Sample 4) cells were grown in random orientations (Figure 4.10). The well plate, which served as a positive control, exhibited similar cellular behavior as the polished samples.

Figure 4.10 - Fluorescence microscope images of polished (a) 3Y-TZP, (b) $ZA_8Sr_8Ce_{11}$, and (c) positive control.

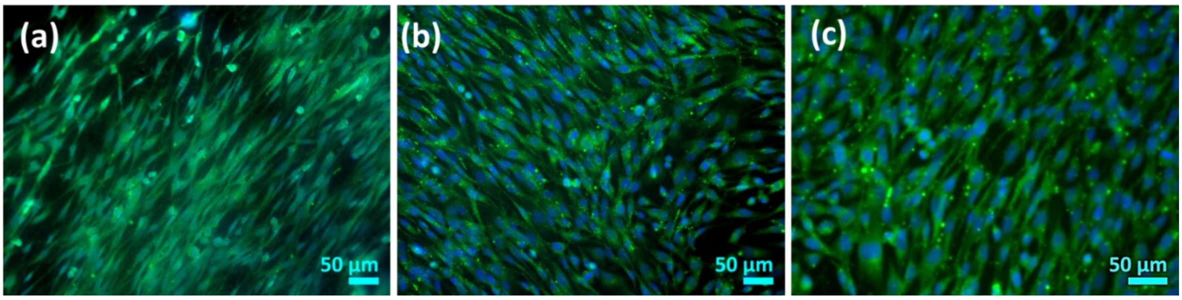

Source: Author.

4.5 DISCUSSION

Direct Laser Interference Patterning was successfully employed to create controlled and well-defined microtextures on the surface of 3Y-TZP and $ZA_8Sr_8Ce_{11}$ ceramics using a nanosecond laser working operating at the infrared wavelength (1064 nm). DLIP is a promising technique for fabricating periodic patterns on the micrometer scale (smaller than conventional laser spot sizes), which can improve surface performance under specific conditions. Single-line texturing experiments (Figure 4.2) demonstrated that selecting appropriate laser parameters is crucial to obtaining a uniform surface and minimizing damage. Low energy can result in incomplete surface ablation (Figure 4.2(a) and (d)), while excessive energy can cause excessive melting and material flow into the structured grooves, disrupting the periodic pattern (Figure 4.2(c) and (f)). Nonetheless, ablation and melting were observed over the entire textured surface, regardless of the fluence, even on the ridges, where the laser intensity should be zero. Two possible mechanisms could explain this phenomenon: (1) heat conduction from the maxima interference regions, increasing the temperature above the melting point over the whole surface, and (2) molten material flow from the high-intensity regions to the surroundings due to high local pressure. Considering the low heat diffusivity of zirconia, the latter seems to be the main cause of the resolidified layer over the surface (Daniel *et al.*, 2008). Comparing the microstructure of 3Y-TZP and $ZA_8Sr_8Ce_{11}$, the fluence required to fully structure the surface was smaller for the composite, indicating a smaller ablation threshold. The composite also showed more melting at higher energy levels. This can explain the fact that despite the lower ablation threshold, lower depths were achieved on the composite for all fluence levels. The molten material, in the liquid phase, can accumulate inside the grooves, reducing their depths, preventing the penetration of the laser beam, and hindering further ablation (Cunha, Ângela *et al.*, 2022). The thermal properties of the two materials could explain their different laser ablation behavior. Alumina, one of the composite constituents, has a higher thermal conductivity than zirconia. This means that the laser energy spreads to the surroundings of the maxima interference regions, which can increase the temperature of the ridges, increasing their ablation and resulting in shallower grooves. Furthermore, the melting points of Al_2O_3 and $SrAl_{12}O_{19}$ are lower than that of 3Y-TZP, which indicates that less energy is required to ablate these materials through thermal mechanisms, resulting in more ablation and melting than 3Y-TZP for the same level of energy. In addition to the composition, microstructural features, such as pores, impurities, and grain boundaries, also can influence the material/laser interaction, increasing energy absorption and ablation rate (Armbruster; Naghilou; Kautek, 2018).

Similar microstructures were achieved when the laser beam was moved in both x- and y-directions to texture the entire areas. However, the increased number of laser pulses hitting the same location led to more melting and a decrease in the average depth of the features for both materials. Moreover, the surface exhibited pores after the laser processing, which were absent in the bulk material. The occurrence of porosity during laser processing can be attributed to localized explosive vaporization or ablation, which may be caused by inhomogeneities in the bulk material, such as closed pores or localized ablation of phases with lower ablation threshold (Daniel *et al.*, 2008; Müller *et al.*, 2020). Microcracking was also observed on the composite surface after texturing. Although microcracks were not detected on the 3Y-TZP, they cannot be ruled out due to their small size and low density. Despite the small size, such cracks can nucleate bigger defects under mechanical stress, leading to premature failure. Therefore, $ZA_8Sr_8Ce_{11}$, due to its toughening mechanisms, is more resistant to processing flaws, such as cracks, pores, and even grooves, that can act as stress concentrators. As a consequence, it would be a better option when defects are inevitable. In fact, the mechanical strength of the composite used in this work is not significantly affected by defects with sizes up to ~150 μm, much larger than any induced processing flaw by the DLIP (Chevalier *et al.*, 2020). Hence, the strength variability of the composite textured samples will be lower, resulting in improved reliability and reproducibility.

The defects observed in the laser-textured samples (porosity, melting, and cracking) are related mainly to the high heat generated by the nanosecond pulsed laser. The material removal process of ceramics involves both photothermal and photochemical (nonthermal) effects. For ultrashort pulsed lasers (e.g., pico- and femtosecond), the pulse duration is shorter than the time required for thermal conduction. Therefore, the ablation process is dominated by photochemical effects, which remove material with minimal or no temperature increase. On the other hand, for lasers with longer pulse duration (nanosecond or longer), heat conduction takes place, increasing the surface temperature and removing material by evaporation and ablation due to the recoil pressure of the liquid phase (Daniel *et al.*, 2008; Harai *et al.*, 2023). The photothermal ablation is confirmed by the presence of resolidified material, which implies that the surface temperature exceeded the melting point of zirconia (~2700 °C).

The confocal images and the surface profile (Figure 4.5) revealed some heterogeneity in the textured area, with variation in the average height among different spots. Furthermore, the average depth of the textured grooves exhibited a large standard deviation. These heterogeneities could be related to the energy distribution along the laser spot and thermal changes induced by the laser energy. The temperature increase and the molten layer can alter the thermal and optical properties of the material, which in turn can affect the laser absorption and ablation rate at each subsequent pulse (Thorstensen; Erik Foss, 2012). Thus, due to these complex interactions, the final surface cannot be easily predicted, and defects and heterogeneities are likely to occur. Further tests, with different parameters, such as hatch distance, fluence, or even optical configuration, can be conducted to improve the quality of the textured surface and achieve an optimal balance between the geometry of the fabricated features (depth, width, and periodicity) and homogeneity while avoiding microstructural defects. However, only ultra-short pulsed lasers may be able to achieve a truly homogeneous and defect-free surface.

X-ray diffractometry revealed a 5.5% tetragonal-to-monoclinic phase transformation in the 3Y-TZP after laser texturing, which is lower than the values reported by similar studies (Goyos-Ball *et al.*, 2018; Moura *et al.*, 2017; Roitero *et al.*, 2017b). The heating caused by laser irradiation can impose thermal stresses and microcracking on the material, causing transformation from the metastable tetragonal phase to the monoclinic. On the other hand, the $ZA_8Sr_8Ce_{11}$ exhibited a 9.5% monoclinic content in the polished sample, which decreased to 1.2% after laser texturing. The monoclinic content in the control sample can be attributed to the mechanical stresses generated by the grinding step, which can trigger the tetragonal-to-monoclinic transformation. However, the lower monoclinic content in the textured sample suggests that the laser ablated the monoclinic phase and/or thermally reverted the phase transformation. A high level of monoclinic content can compromise the mechanical performance and long-term reliability of zirconia and zirconia-based composites. However, the phase transformation due to the laser treatment was lower for both materials than usually reported by other traditional surface treatments, such as sandblasting (Faria *et al.*, 2020). Moreover, zirconia, especially 3Y-TZP, is susceptible to low-temperature degradation (LTD), which is a spontaneous tetragonal-to-monoclinic transformation that occurs over time in moist environments (Roitero *et al.*, 2018b). LTD, also known as aging, is an undesirable phenomenon that can cause surface roughening and a reduction in the mechanical properties of zirconia (Chevalier, 2006). On the other hand, the addition of ceria into the zirconia grains as a stabilizer can inhibit the LTD phenomenon. Tests showed that the composite used in this work ($ZA_8Sr_8Ce_{11}$) and similar ones are virtually immune to aging (Reveron *et al.*, 2017). Therefore, although some phase transformation was observed after the laser texturing for the 3Y-TZP, further spontaneous transformation is not expected. To restore the crystallography and the mechanical properties of the material to a certain extent, studies have shown that an annealing thermal treatment (heating up to 1200 °C for 1h) can revert partially the phase transformation and decrease the monoclinic content. This thermal treatment also improves the zirconia resistance to LTD (Moura *et al.*, 2017; Pereira *et al.*, 2020).

The water contact angle measurements revealed a significant decrease in the wettability following laser texturing on both materials, making the surface hydrophilic. Two models are commonly used to describe the interaction between the surface roughness and its wettability: (1) the Cassie-Baxter model, which assumes that air is trapped in the valleys between the surface and the liquid, enhancing the hydrophobicity as roughness increases, regardless of the wetting behavior of the flat surface; and (2) the Wenzel model, which describes the wetting behavior when the liquid fills the valleys, and states that a hydrophobic surface becomes more hydrophobic and a hydrophilic surface becomes more hydrophilic as roughness increases (Cassie; Baxter, 1944; Wenzel, 1936). Therefore, the results obtained in this study suggest that the Wenzel mode occurred on the samples. Secondary surface damage, such as open porosity and nano-droplet formation, also affects the surface roughness and can influence wettability. Besides the surface topography, the wettability is also influenced by the surface free energy, which is directly related to the material's chemical composition. In general, a higher surface free energy is associated with a lower water contact angle. The chemical changes caused by the laser texturing may have also influenced the wettability in this study. For example, an increase in the O_2 content seems to decrease the WCA in partially stabilized zirconia (Hao; Lawrence, 2003). This fact can also explain the slight decrease in the samples' wettability over time. Contamination can cause changes in surface-free energy and wetting behavior (Giannuzzi *et al.*, 2019). Although WCA was measured for only one condition in the present study, other works have demonstrated that wettability behavior is highly dependent on surface texturing characteristics, such as groove depth, width, and orientation (Ji *et al.*, 2020; Pu *et al.*, 2020). The surface can even transition from a hydrophilic state (Wenzel mode) to a hydrophobic one (Cassie-Baxter mode), especially for wider and deeper grooves (Ji *et al.*, 2020). Thus, further tests can be conducted to investigate the influence of different laser-induced topographies (with different groove width, depth, and period values) on the wettability of the material.

The biological tests performed in this study were only preliminary (with only one sample per group), but they provide a promising first insight into the behavior of textured surfaces in biological applications. No significant difference in cell viability was observed between the different materials and surfaces, but the small sample size prevents any definitive conclusion. However, most studies in the literature indicate that laser surface treatment can enhance the adhesion, proliferation, and even differentiation of cells on zirconia surfaces (Cunha, Welson *et al.*, 2022). The nano and micro-scale features can provide more sites for the adhesion of the cells' focal points (Chen *et al.*, 2009). On the other hand, it is evident that cell growth followed the direction of the structured grooves, while the cells grew in random orientations in the polished and control samples. Other studies have reported similar results, with cells preferentially growing in the same direction as the grooves, whether they were structured by laser or machining (Lukaszewska-Kuska *et al.*, 2018; Zwahr *et al.*, 2017). The cells actively sense the topographical features of the surface, which provide contact guidance for their growth, leading to cell alignment along the structures (Fujita; Ohshima; Iwata, 2009). In addition to topography, surface wettability also affects cell attachment. A high surface free energy and increased hydrophilicity can enhance the interaction between the surface and the biological environment, increasing cell adhesion and proliferation (Jiao *et al.*, 2021). Although the wettability was not measured immediately before the biological tests, they were performed more than 30 days after the laser texturing, thus the wetting behavior of the textured samples was likely hydrophilic. Further studies are proposed to evaluate cell viability in multiple samples for more accurate results over different periods and evaluate cell differentiation into the osteogenic path, followed by in vivo analyses.

4.6 CONCLUSION

This work investigated the effects of Direct Laser Interference Patterning (DLIP) on the surface morphology, wettability, and biological behavior of zirconia (3Y-TZP) and a zirconia-based composite (Ce-TZP/Al_2O_3/$SrAl_{12}O_{19}$). Based on the results, the following conclusions can be drawn:

- DLIP successfully created line-like patterns with a spatial period of 6 μm on both materials, resulting in an average feature depth of about ~0.8 μm for the fully textured samples.
- The composite required less energy to reach ablation than the 3Y-TZP, but the latter achieved deeper structures in single-line texturing. Both materials showed evidence of melting and thermal damage, such as cracking and porosity, due to the photothermal mechanism of ablation.
- Laser texturing increased the hydrophilicity for both materials, indicating Wenzel model of wettability.
- Initial biological tests revealed that the textured samples had comparable cell viability to the polished ones, but the cell growth was aligned with the direction of the textured grooves. Therefore, DLIP could be used to guide cell orientation.
- These findings suggest that DLIP is a promising technique for functionalizing zirconia and zirconia-based composites for biomedical applications.

5 MICROMETRIC STRUCTURING OF 3Y-TZP AND CE-TZP/AL_2O_3/$SRAL_{12}O_{19}$ COMPOSITE USING DIRECT LASER INTERFERENCE PATTERNING WITH ULTRA-SHORT PULSED LASER

5.1 ABSTRACT

The development of new materials and surface treatments has been extensively investigated to enhance the biological behavior and reliability of implants. This study aimed to fabricate micropatterns on the surface of two types of zirconia-based ceramics: conventional dental grade zirconia (3Y-TZP) and a novel high-toughness nanocomposite (Ce-TZP/Al_2O_3/$SrAl_{12}O_{19}$) using Direct Laser Interference Patterning (DLIP) with an ultra-short pulsed laser (10 ps). Both materials were successfully textured with line-like patterns with a periodicity of 6 µm and depths ranging from 1 µm to 3 µm, with the nanocomposite requiring lower energy for ablation. The picosecond laser produced homogeneous and well-defined structures with negligible thermal effects. Minor defects (cracks and pores) in the nanoscale were observed in the scanning electron microscope images, which were attributed to the laser processing. X-ray diffractometry revealed only a minor tetragonal to monoclinic transformation for the 3Y-TZP, while the composite exhibited some transformation during the grinding process, which prevented the assessment of phase transformation due to the laser texturing. The micropatterns increased the hydrophobicity of both materials, with water contact angles of 139.3 ± 4.4° and 105.8 ± 13.1° for the 3Y-TZP and the nanocomposite, respectively, compared to 90.4 ± 2.0° and 84.9 ± 5.1° for the polished groups. These results demonstrate the feasibility and potential of DLIP with an ultra-short pulsed laser for creating micropatterns on zirconia-based ceramics with enhanced surface properties.

5.2 INTRODUCTION

Zirconia is a biocompatible ceramic that has been widely applied in orthopedic and dental implants due to its chemical stability, good mechanical properties, and aesthetic appearance (Piconi; Maccauro, 1999; Zhang; Lawn, 2018). The most common form of zirconia for these applications is 3 mol% yttria-stabilized Tetragonal Polycrystalline Zirconia (3Y-TZP), which exhibits remarkable mechanical strength (up to 1200 MPa in flexural tests). However, 3Y-TZP is susceptible to low-temperature degradation (LTD), a phenomenon that involves a spontaneous phase transformation in the presence of water that leads to surface roughening and compromises mechanical reliability (Lughi; Sergo, 2010). Alternatively, ceria-stabilized zirconia (Ce-TZP) has significantly reduced susceptibility to LTD, as well as superior toughness, albeit at the expense of lower strength (Kohorst *et al.*, 2012). To achieve a balance between good toughness, strength, and resistance to LTD, nanometric second phases, such as alumina and aluminates, have been incorporated into Ce-TZP, resulting in composites, such as the Ce-TZP/Al_2O_3/$SrAl_{12}O_{19}$, with an outstanding combination of these properties (Chevalier *et al.*, 2020; Reveron *et al.*, 2017).

In recent years, significant efforts have been devoted to modifying the surface of biomaterials aiming at improving their biological performance. A rough surface is generally desirable, as it provides more surface area to connect to the biological tissue in the osseointegration process, resulting in enhanced primary and long-term stabilization of implants (Buser *et al.*, 1991). Moreover, the surface topography can modulate its wettability, which plays a crucial role in the tissue-implant interaction (Gittens *et al.*, 2014). Additionally, controlled periodic patterns in the nanoscale can influence the orientation, adhesion, migration, and differentiation of cells into osteoblasts (Cunha *et al.*, 2015; Martínez-Calderon *et al.*, 2016). Conventional surface treatments, such as grit-blasting and acid etching, aim at increasing the surface roughness to improve osseointegration. However, these treatments produce only random patterns with limited dimensional control. In contrast, laser processing has emerged as a potential method for surface functionalization of biomaterials due to its high resolution and flexibility, which allows the fabrication of nanoscale patterns in various materials. The laser parameters can be easily modified and optimized to reach the desirable morphologic aspects and biological response (Cunha, Welson *et al.*, 2022). Among the laser techniques, Direct Laser Interference Patterning (DLIP) stands out due to its ability to fabricate controlled periodic micro- and nanotopographies (Lasagni *et al.*, 2017). In this method, the laser beam is split into two or more sub-beams, which are superposed at the material surface to generate an interference pattern where ablation occurs at the maxima. The pattern geometry (e.g., lines, dots, and lamellas) and feature size can be controlled by varying the number of sub-beams, incident angle, beam intensities, polarization, and laser wavelength.

Direct Laser Interference Patterning has been successfully applied in zirconia to produce controlled microstructures. However, most studies used nanosecond pulsed laser, which can induce thermal effects on the surface, resulting in defects such as porosity, melting, and cracking (Daniel *et al.*, 2008; Roitero *et al.*, 2017b). Moreover, the melting and liquid flow can compromise the geometric definition of the structures. The microstructural changes caused by the thermal shock during laser processing can also decrease the zirconia strength and its resistance to LTD (Roitero *et al.*, 2018b, 2018a). In contrast, it has been demonstrated that DLIP processing of zirconia with ultra-short pulsed lasers, in the fs range, can produce a higher quality surface with well-defined structures (clear separation between grooves and ridges), although some porosity and microcracking were also reported (Müller *et al.*, 2020).

This work aims to investigate the fabrication of controlled micrometric texture on the surface of 3Y-TZP zirconia and Ce-TZP/Al_2O_3/$SrAl_{12}O_{19}$ zirconia-based nanocomposite using DLIP technique with a picosecond pulsed laser. The influence of the laser parameters on the surface morphology was studied to achieve a homogeneous surface. Furthermore, the microstructure and wettability of the textured surface were characterized.

5.3 MATERIALS AND METHODS

5.3.1 Materials

The samples were prepared as discs by pressing and sintering the ceramic powders. The present study employed commercially available powders of zirconia stabilized with 3 mol% of Yttria (TZ-3YSB Tosoh, Japan) and the composite Ce-TZP/Al_2O_3/$SrAl_{12}O_{19}$ (composition: 84 vol% ZrO_2 (stabilized with 11 mol% CeO2), 8 vol% Al_2O_3 and 8 vol% $SrAl_{12}O_{19}$, manufactured by DOCERAM, Germany). For convenience, the composite will henceforth be denoted as $ZA_8Sr_8Ce_{11}$. The powders were subjected to uniaxial pressing in cylindrical steel dies at pressures of 100 MPa (3Y-TZP) and 70 MPa ($ZA_8Sr_8Ce_{11}$) for a duration of 60 s to obtain green compacts. The samples were subsequently sintered at 1500 °C for 2 h (3Y-TZP) and 1450 °C for 1 h ($ZA_8Sr_8Ce_{11}$). The sintered samples were then subjected to sanding and polishing (down to a grit size of 1 μm diamond particles) to achieve a flat surface and a mirror-like finish. The final dimensions of the discs were 16.9 mm in diameter and 1.6 mm in thickness.

5.3.2 Laser texturing

The texturing process was carried out using an ultra-short pulsed (10 ps) solid-state Nd:YVO4 laser (PX200, EdgeWave, Germany) emitting a wavelength of 1064 nm, a maximum output power of 10 W, and a fixed repetition rate of 10 kHz. The workstation is equipped with a self-developed DLIP optical head (Fraunhofer IWS/TU Dresden, Germany) which uses a diffractive optical element (DOE) to split the laser beam into two sub-beams. The sub-beams are then parallelized by a prism and overlapped and focused on the sample surface using a converging aspheric lens. This optical setup is illustrated in Figure 5.1(a). A line-like interference pattern is generated within an area of ~60 μm in diameter (Figure 5.1(b)). The periodicity Λ of the generated pattern (distance between consecutive lines) can be calculated according to equation 5.1.

$$\Lambda = \frac{\lambda}{2\sin\theta} \tag{5.1}$$

Where λ is the laser wavelength and θ is the half-angle between the sub-beams, as shown in Figure 5.1(b). In this work, θ was set as ~5.1°, generating a periodicity of 6 μm.

To texture lines or areas bigger than the spot size, the sample is translated in x- and y-direction using high-precision linear stages (Aerotech PRO165-300, USA). The texturing strategy first consisted of moving the sample in the y-direction to texture a line controlling the pulse overlap (Ov). Then the sample is translated in the x-direction controlling the hatch overlap (Ho), as illustrated in Figure 5.1(c). The overlap determines the average number of pulses hitting the same spot. In this work, the overlap was varied between 90% and 99%, the hatch overlap between 40% and 80%, and the laser fluence between 0.49 J/cm² and 0.56 J/cm² for the 3Y-TZP and 0.13 J/cm² and 0.21 J/cm² for the composite.

Figure 5.1 - (a) Optical setup used on the direct laser interference patterning system; (b) interference pattern created when the two sub-beams overlap with half-angle θ; (c) texturing strategy: the sample is moved on the y-direction by a certain distance set by the overlap (Ov) to texture a line, then the sample is moved on the x-direction by the distance set by the hatch overlap (Ho) to texture an area.

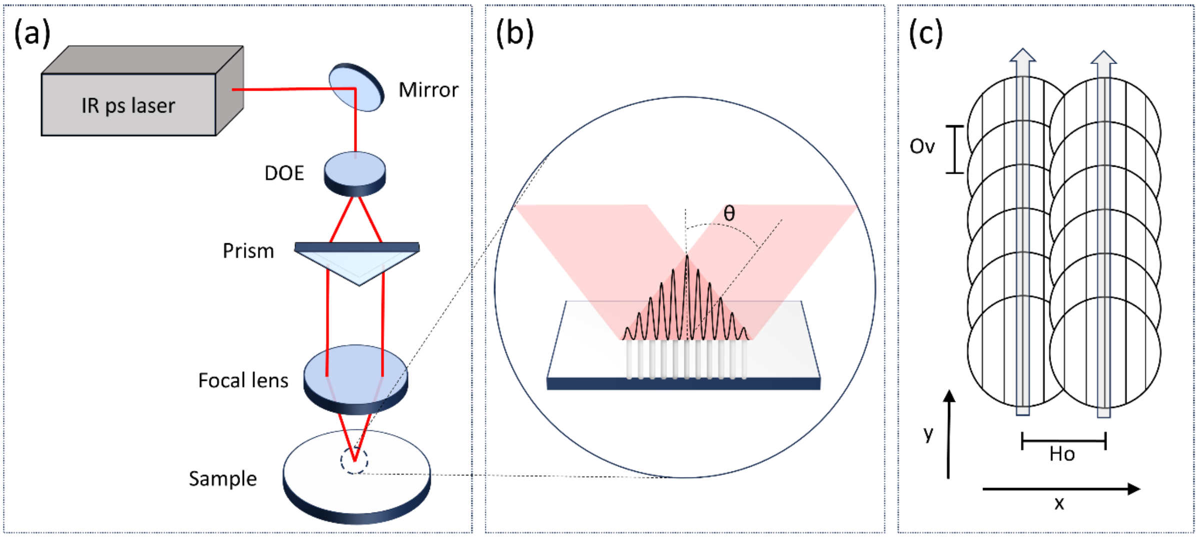

Source: Author

5.3.3 Surface characterization

The morphology and microstructure of the textured samples were analyzed using a Scanning Electron Microscope (SEM) (Hitachi TM-3030, Tokyo, Japan) at an operating voltage of 15.0 kV. To investigate the subsurface, cross-section observations were performed using a Focused Ion Beam/Scanning Electron Microscope workstation (FIB/SEM, NVision 40; Carl Zeiss Microscopy GmbH, Germany), combining a SIINT zeta FIB column (Seiko Instruments Inc. NanoTechnology, Japan) with a Gemini I column. Furthermore, the topography of the textured surfaces was analyzed using a confocal microscope (Sensofar S Neox, Spain) equipped with 50x and 150x objectives, resulting in vertical and lateral resolution of 2 nm and 140 nm, respectively. The representation and quantification of the topographical data were performed using the software SensoMap (Sensofar, Spain).

The crystallographic analysis of the samples (before and after texturing) was performed using an X-ray diffractometer (XRD) equipped with a Cu-Kα source (Rigaku Miniflex 600, Japan). The XRD spectra were acquired over a 2θ range between 10° and 80° at a step size of 0.05° and a scan speed of 5°/min. As this analysis was performed mainly to evaluate the tetragonal to monoclinic phase transformation due to laser texturing, the quantification of both phases was calculated using the Toraya Equation (Toraya; Yoshimura; Somiya, 1984).

The wettability of the polished and textured samples was assessed by measuring the static water contact angle (WCA) using a drop shape analyzer (Krüss DSA100S) depositing 4 µl droplets of deionized water on the sample. WCA was calculated by measuring the contact angle between the surface and the droplets through the tangent fitting method. The reported values are the average of 9 measurements, both perpendicular and parallel to the textured grooves. Measurements were taken in air at room temperature, and the samples were cleaned with compressed air before any measurement.

5.4 RESULTS

The DLIP textured regions on the 3Y-TZP sample, when moved only along the y-axis, are shown in Figure 5.2 for different parameters. A set of lines, with a periodicity (distance between lines) of 6 µm, can be successfully created depending on the amount of deposited energy, which is the result of the chosen fluence and overlap (Ov). The pattern reflects the energy density distribution created by the laser sub-beams interference, where the ablated regions correspond to the energy maxima points when this energy surpasses the material fluence threshold. Due to the Gaussian distribution of the laser beam energy, the center lines tend to have more depth than the border lines, which may not ablate at low fluences. The effect of varying the overlap for a fixed fluence (0.49 J/cm²) is shown in Figure 5.2(a-c). A low overlap (90%) results in incomplete ablation, while a high overlap (>98%) causes excessive material removal on the minima positions of the interference pattern, destroying the ridges. Homogeneous and well-defined grooves, with an average depth of 1.3 µm, could be obtained for an overlap of 96%. Similarly, fixing the overlap at 96%, and decreasing or increasing the laser fluence (Figure 5.2(d) and Figure 5.2(e)) leads to either incomplete line ablation or excessive material removal, respectively. Therefore, for further texturing of entire areas of 3Y-TZP, fluence values around 0.49 J/cm² and overlap values of 96% were used.

Figure 5.2 - Single line texturing of 3Y-TZP with different values of fluence and overlap.

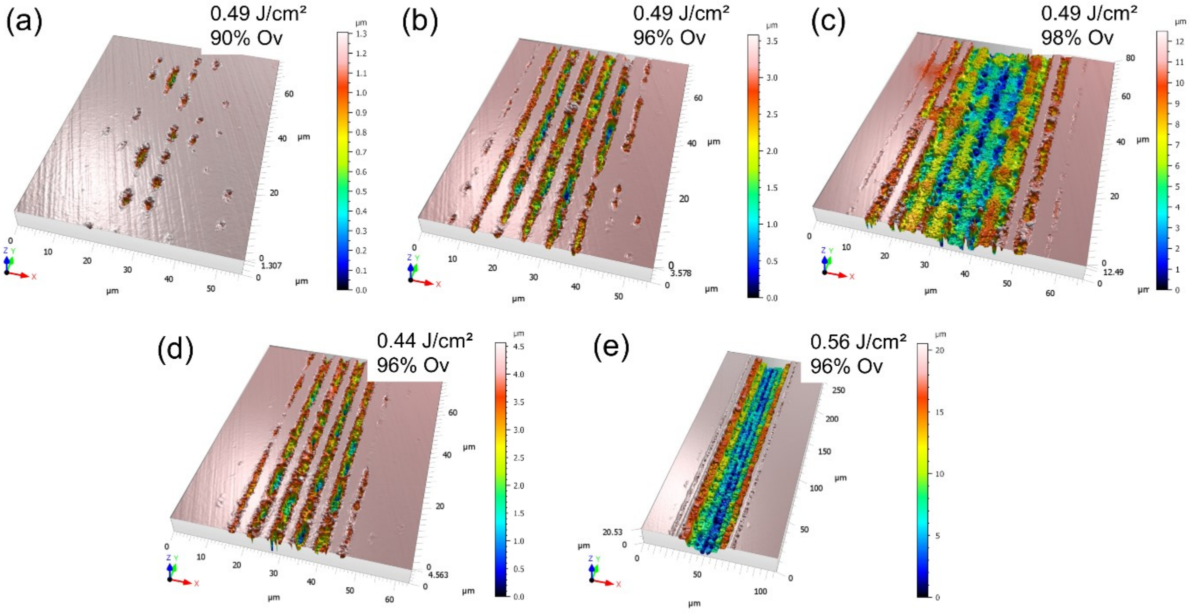

Source: Author.

The laser texturing of $ZA_8Sr_8Ce_{11}$ followed the same trend as the monolithic zirconia, but lower values of fluence were necessary to ablate the material, as shown in Figure 5.3. Fixing the fluence at 0.13 J/cm², the optimal topography is achieved when the overlap is 98%, resulting in homogeneous grooves with depths of about 0.9 µm. Smaller overlaps produced shallow (~150 nm) and poorly defined grooves, while higher overlaps led to inhomogeneous grooves, likely due to melting. Although the objective is to texture entire areas, the fabrication of single lines is important to find a range of optimal parameters for the DLIP technique.

Figure 5.3 - Single line texturing of ZA$_8$Sr$_8$Ce$_{11}$ with different values of overlap.

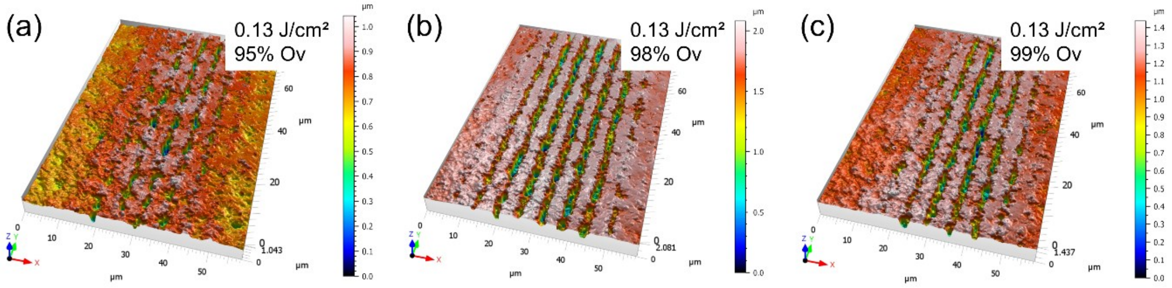

Source: Author

Assuming the values of laser fluence and overlap from the previous section, entire areas could be textured by moving the samples also on the X-direction. The hatch overlap (Ho) value must be chosen such that the textured lines always overlap with the previous grooves. This means that the sample must move in the X-direction by a multiple of the periodicity (6 µm). Considering the laser beam diameter (60 µm), Ho can only assume values that are multiples of 10%. Figure 5.4 shows the influence of hatch overlap (a-c) and fluence (d-f) on the textured surfaces of 3Y-TZP. For low values of hatch overlap (>40%), the texture was inhomogeneous due to the Gaussian nature of the laser beam, resulting in areas with different ablation levels, even with a high overlap (99%). A fairly homogeneous surface, with average depths between 2.5 µm (for Ho = 70%) and 2.8 µm (for Ho = 80%), was obtained by increasing the Ho to at least 70%. When the hatch overlap was fixed at 80% and the overlap reduced to 96%, more homogeneous and well-defined structures could be obtained for a low fluence (0.35 J/cm²), with an average depth of 3.2 µm. Higher fluence values caused some heterogeneities due to melting, resulting in a decreased depth of around 2.0~2.3 µm. Therefore, the surface fabricated with a fluence of 0.35 J/cm², overlap of 96%, and hatch overlap of 80% (Figure 5.4(d)) was selected for further tests.

Figure 5.4 - Area texturing of 3Y-TZP for different values of fluence, pulse-to-pulse overlap (Ov), and hatch overlap (Ho).

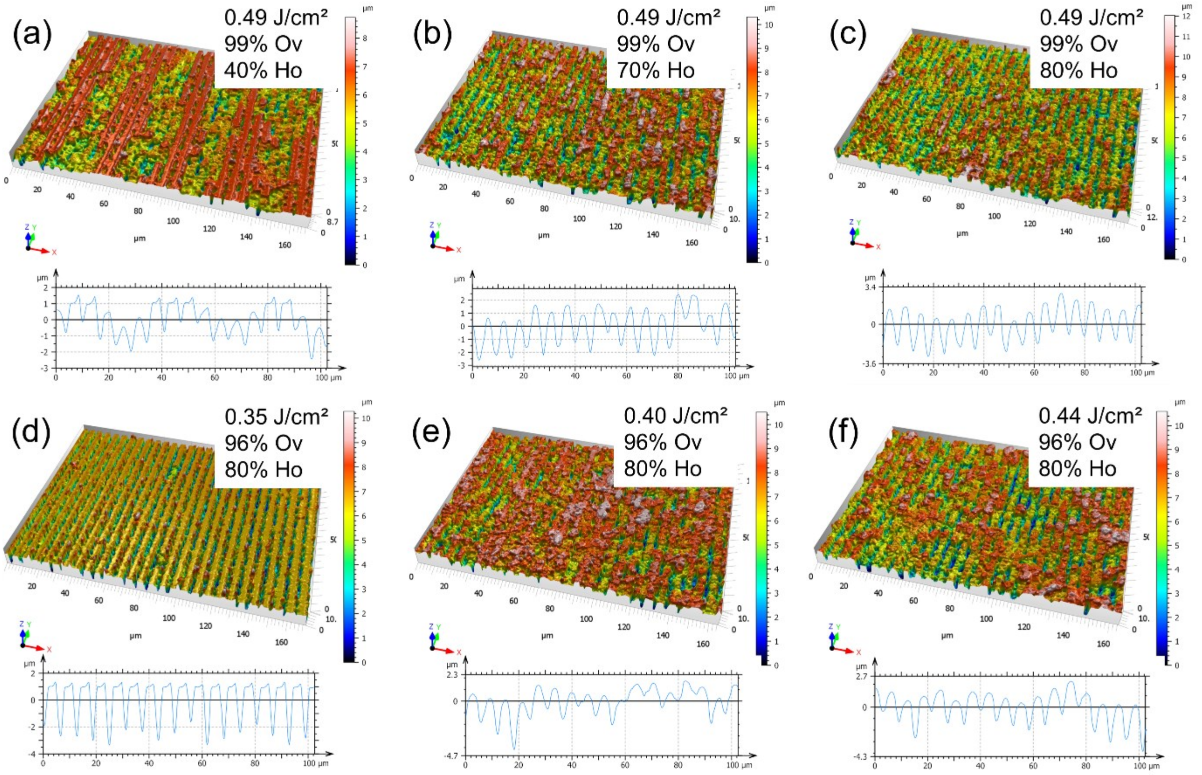

Source: Author.

The surface topography of the composite material followed the same trend as that of the 3Y-TZP, with heterogeneous surfaces obtained for low hatch overlaps (<40%). However, homogeneous structures were achieved by increasing the hatch overlap to 60%. Figure 5.5 shows the well-defined structures obtained for fluences between 0.13 J/cm² and 0.21 J/cm², with a fixed overlap of 98% and a hatch overlap of 60%. The average depth increased proportionally to the fluence for the tested range, unlike the 3Y-TZP, with no sign of melting observed on the topographies The average depth was 0.5 µm for the lowest fluence (0.13 J/cm²), 2.0 µm for the intermediate fluence (0.17 J/cm²), and 2.8 µm for the highest fluence (0.21 J/cm²). The surface structure with 0.21 J/cm², overlap of 98%, and hatch overlap of 60% was selected for further tests, due to its good quality and depth similar to the 3Y-TZP structure.

Figure 5.5 - Area texturing of $ZA_8Sr_8Ce_{11}$ for different values of fluence.

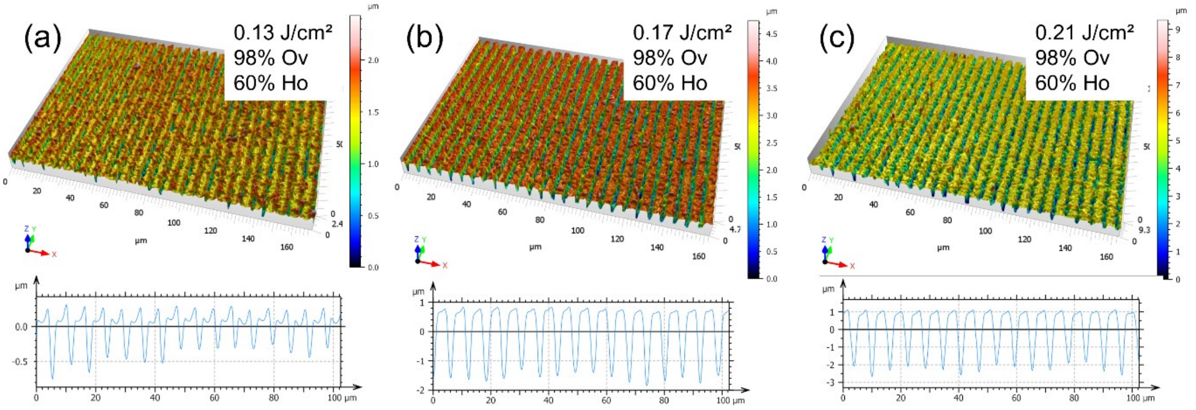

Source: Author.

Figure 5.6 shows the SEM images of the surface morphology and microstructure of the final samples. The morphology appears quite different for both materials, despite the confocal microscopy analysis showing similar topography. The area unaffected by the laser (ridges) is smaller for the 3Y-TZP (Figure 5.6(a)) than for the composite (Figure 5.6(b)). Nevertheless, the morphology of both materials is homogeneous, and no signs of defects, such as cracks and resolidified layer, were observed.

Figure 5.6 - SEM images of the textured surface of (a) 3Y-TZP (fluence 0.35 J/cm², overlap 96%, and hatch overlap 80%) and (b) $ZA_8Sr_8Ce_{11}$ (fluence 0.21 J/cm², overlap 98% and hatch overlap 60%).

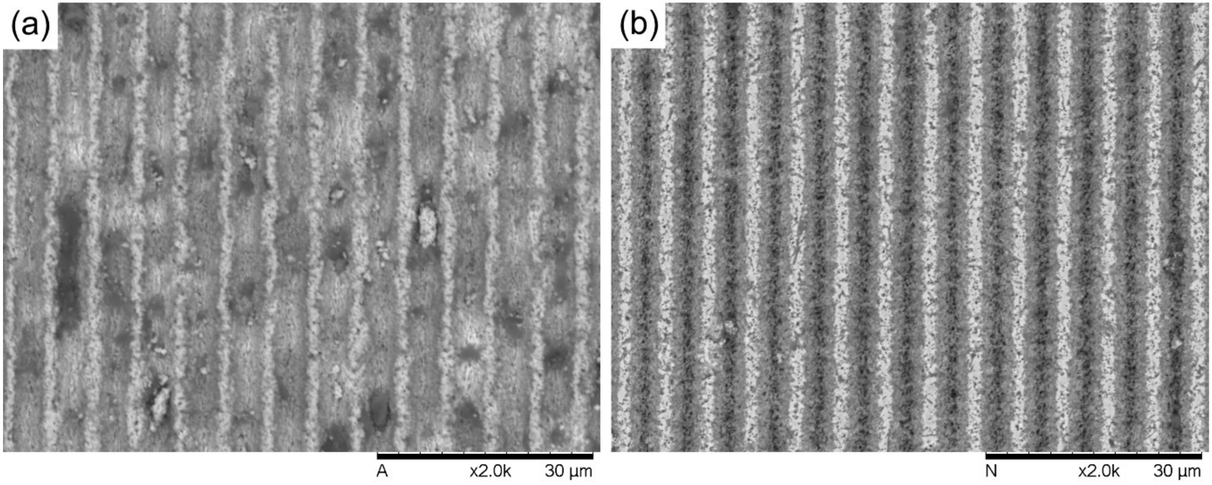

Source: Author.

Figure 5.7 shows SEM images of the cross-sections produced by FIB for the (a) monolithic zirconia and (b) the composite. For both materials, the grains remained equiaxial and approximately the same size as the bulk material, indicating no resolidification or recrystallization layer. Two levels of porosity can be observed on the material: (1) larger pores, which are distributed over the entire material, especially in the composite. Their origin is likely associated with the manufacturing technique used to produce the discs (uniaxial pressing and sintering). And (2) smaller pores, on the nanometric scale, which are located just below the textured surface, as indicated by the red arrows. Some cracks, no longer than a few hundred nanometers, could also be observed on the surface. Irregularities on the textured surface, in the format of open pores, can be noticed in the cross-section images.

Figure 5.7 - Cross-section SEM images of the textured (a) 3Y-TZP and (b) $ZA_8Sr_8Ce_{11}$ samples.

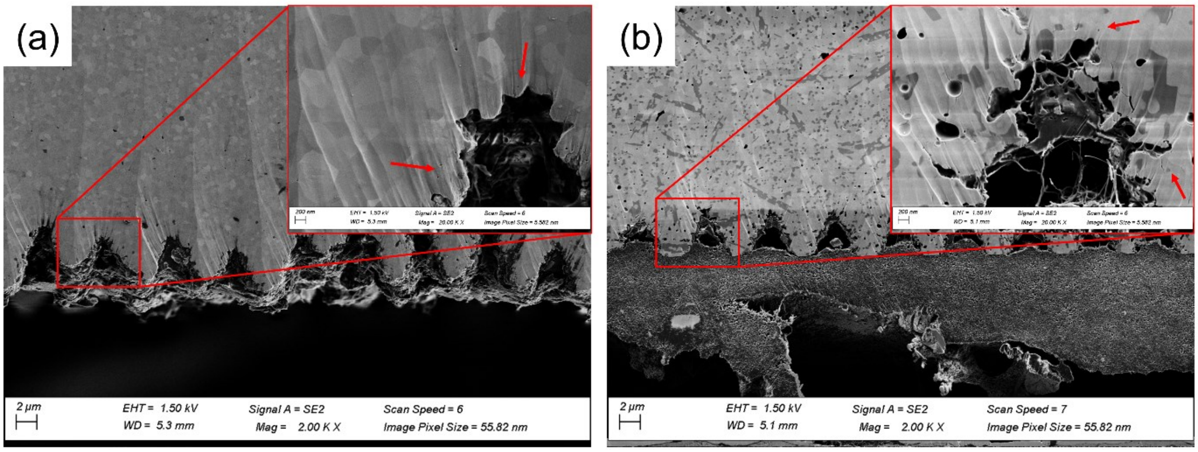

Source: Author.

The X-ray diffractograms for the zirconia and the composite, before and after the laser texturing, are shown in Figure 5.8. The letters t and m indicate peaks relative to the tetragonal and monoclinic phase, respectively. The polished sample of 3Y-TZP presented only diffraction peaks related to the tetragonal phase, but small peaks related to the monoclinic phase appeared after the laser texturing at 29° and 31°. By the Toraya equation, the calculated monoclinic content of the textured sample was 3.9%. On the other hand, the $ZA_8Sr_8Ce_{11}$ polished sample showed a calculated monoclinic content of 9.7%, while the textured sample presented 15.5% of monoclinic content.

Figure 5.8 - Diffractometry of the analysed samples.

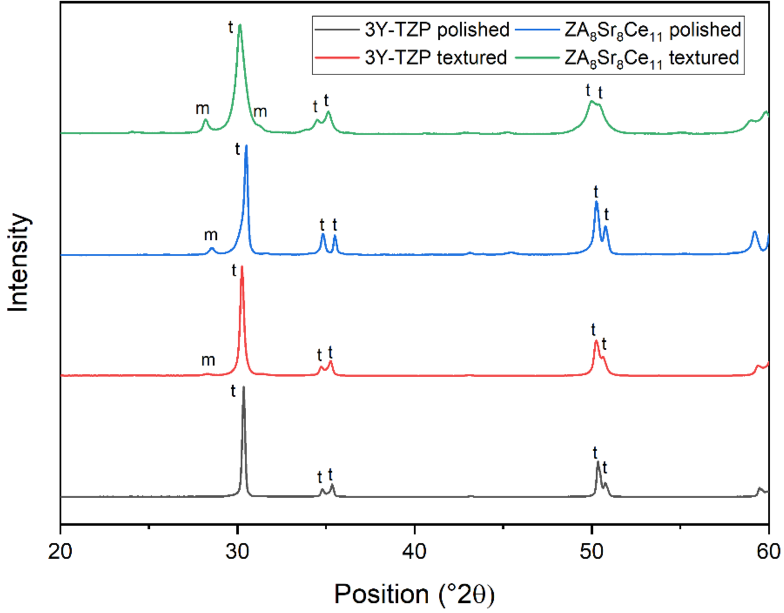

Source: Author

The water contact angle (WCA) was used to assess the wettability of the polished and textured samples, which were prepared by laser texturing within three days before the measurement. A drop-shape analyzer was employed to determine the WCA of the samples. The control group (polished samples) of the 3Y-TZP and the $ZA_8Sr_8Ce_{11}$ exhibited a WCA of 90.4 ± 2.0° and 84.9 ± 5.1°, respectively, indicating a slight hydrophilic surface. In contrast, the laser-textured samples of both materials showed a significant increase in WCA, reaching 139.3 ± 4.4° for the traditional zirconia and 105.8 ± 13.1° for the composite, suggesting a hydrophobic surface. The WCA was measured parallel and perpendicular to the textured lines, but no significant difference was observed between the two directions. Therefore, the average values reported here represent the combined results of both measurements. Additionally, the WCA measurements were repeated after 15 days of the texturing, but no significant change was observed. Figure 5.9 illustrates this behavior, showing the WCA analysis for one sample of 3Y-TZP and composite before and after laser texturing.

Figure 5.9 - Water contact angle analysis of 3Y-TZP and $ZA_8Sr_8Ce_{11}$ before and after laser texturing.

3Y-TZP polished

$ZA_8Sr_8Ce_{11}$ polished

3Y-TZP textured

$ZA_8Sr_8Ce_{11}$ textured

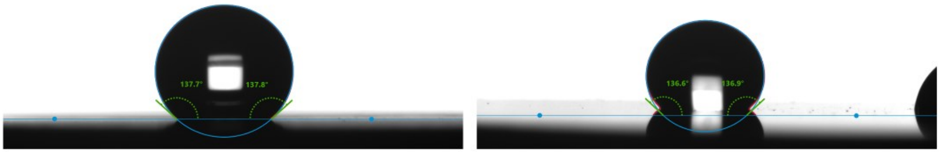

Source: Author.

5.5 DISCUSSION

Line-like micrometric well-defined textures were successfully produced on the surface of 3Y-TZP and $ZA_8Sr_8Ce_{11}$ using the Direct Laser Interference Patterning technique equipped with a picosecond (10 ps) laser working at the infrared wavelength (1064 nm). The influence of the laser parameters, namely laser fluence, pulse overlap, and hatch overlap, on the morphology of the fabricated periodic structures was systematically investigated. The influence of laser texturing on the surface microstructure and wettability was also studied.

The texturing process consisted of two steps: first, single lines were textured by moving the sample in only one direction, using different laser parameters to select the optimal ones; second, entire areas were textured by moving the sample also in the x-direction, using the optimal parameters. The laser parameters, namely fluence, and overlap, affected the depth and definition of the structures. While insufficient energy (low overlap and/or fluence) resulted in shallow and incomplete structures (Figure 5.4(a) and Figure 5.5(a)), excessive energy caused the ablation of the ridges, at the laser interference minima, decreasing the definition of the pattern lines (Figure 5.4(c) and (e)). The optimal parameters produced homogeneous and well-defined patterns, with lines ablated only at the interference maxima, while the minima regions remained intact. To create a uniform structure over the entire area, the consecutive lines had to be close enough to compensate for the Gaussian nature of the laser beam. Otherwise, grooves with different depths would be formed throughout the area, as shown in Figure 5.4(a), which could also be useful for creating hierarchical structures (El-Khoury *et al.*, 2020). In general, the depth of the grooves increased with higher energy levels. However, if excessive energy is applied, either by high fluence or high overlap, the material can melt, accumulating inside the grooves, preventing further laser ablation, and decreasing their overall depth (Cunha, Ângela *et al.*, 2022).

Comparing both materials, the composite demanded less energy to achieve complete texturing, indicating a smaller ablation threshold. This difference was attributed to the different thermal properties of the materials, which affected their response to thermal ablation. The composite constituents, alumina (Al_2O_3) and strontium aluminate ($SrAl_{12}O_{19}$), have lower melting points than the zirconia, indicating that less energy is required to ablate these materials. Other material properties can also influence the ablation threshold, such as band gap, which determines the laser energy absorption, and the presence of defects, such as pores, impurities, and grain boundaries, which increases the laser absorption (Armbruster; Naghilou; Kautek, 2018). For instance, Han et al. compared the ablation of zirconia and alumina/zirconia composites and attributed the lower ablation threshold of the composite to the higher presence of defects (Han *et al.*, 2022a).

The microstructure images obtained by the SEM confirmed the homogeneity and good quality of the fabricated surface. The surface showed no evidence of microcracking or resolidification. The grooves and ridges were well-defined, and their width was consistent across the surface. A similar microstructure was reported in another study that used a femtosecond laser-based DLIP system to texture zirconia (Müller *et al.*, 2020). However, it contrasts with other reports that used DLIP systems with nanosecond lasers to texture zirconia. In those studies, the grooves were shallow and incomplete, and the ablated (grooves) and unablated (ridges) areas were not clearly distinguished due to the melting of the entire surface (Daniel *et al.*, 2008; Roitero *et al.*, 2017a). These morphological differences could be attributed to the different laser-matter interactions and ablation mechanisms for ultra-short (ps) and short-pulse lasers (ns). For ultra-short pulsed laser (pulse duration in the picosecond range or shorter), as used in the present work, the ablation is based on the surface ionization induced by very short and intense pulses. This results in a local conversion of the material into a plasma, which extracts atoms from the solid (Coulomb explosion) (Delgado-Ruíz *et al.*, 2011; Wang *et al.*, 2008). Since the pulse duration, and hence the ablation process, is shorter than the time required for thermal conduction, the material is removed without any heat transfer to the surrounding regions. However, if the fluence or the number of pulses per spot is too high, more energy is absorbed by the ionized surface, which can increase the local temperature and cause thermal ablation processes. These processes can be accompanied by thermal defects, such as cracking and melting. Therefore, it is essential to carefully select the laser processing parameters even for ultra-short pulsed lasers to avoid such issues. On the other hand, for short pulse duration (nanosecond or longer), more energy is dissipated on the surface due to the longer laser-matter interaction time. This results in a sharp increase in surface temperature and the removal of material by evaporation and ablation due to the recoil pressure of the liquid phase (Daniel *et al.*, 2008; Harai *et al.*, 2023).

The microstructure of both materials was analyzed using cross-sectional SEM images. The laser texturing process had negligible thermal effects on the microstructure of both materials, and the grains remained equiaxial without any substantial defects such as cracks. However, irregularities, in the format of open pores, were observed on the surface of the textured grooves. These pores are likely due to localized explosive vaporization in inhomogeneities in the bulk material (Müller *et al.*, 2020). Pores were also observed in the bulk material, but their formation is not related to the laser technique, but rather introduced during the manufacturing process (pressing and sintering). On the other hand, nanoporosity was also observed just below the textured surface, which can be attributed to the laser processing. Due to the optical penetration of the laser beam, overheating can occur in the subsurface and create additional pores (Daniel *et al.*, 2008). This microstructure contrasts with another study that reported a heat-affected zone on zirconia when textured with a ns laser, where intergranular cracking, porosity, directional recrystallization, and a recast layer were evident (Roitero *et al.*, 2017b). Again, the mainly athermal ablation mechanism of ultra-short pulsed lasers allowed the texturing of zirconia and zirconia-based composite without imposing substantial damage to their microstructure. On the other hand, XRD analyses showed some tetragonal to monoclinic transformation after the laser texturing for the 3Y-TZP. This indicates that the temperature increase imposed by the laser was high enough to cause the phase transformation directly (by exceeding the temperature threshold for the t→m transformation) or indirectly (by inducing thermal stresses). Since the monoclinic content after laser texturing is very low (3.9%), it should not significantly alter the material's mechanical strength (Alghazzawi *et al.*, 2012). On the other hand, the polished composite exhibited a 9.7% content of monoclinic phase, which can be attributed to the mechanical stresses induced by the grinding step, which can trigger the phase transformation. The fact that the composite requires less energy to occur the t→m transformation explains the higher monoclinic content in comparison to the 3Y-TZP (Chintapalli *et al.*, 2013). After the laser texturing, the monoclinic content increased to 15.5%. Not only the laser texturing may have caused the increase in the monoclinic phase, but also the manual grinding process, which can generate slightly different amounts of monoclinic phase in different samples. Therefore, crystallographic analysis should be conducted to draw an appropriate conclusion regarding phase change due to laser texturing in $ZA_8Sr_8Ce_{11}$. Thermal residual stresses, which may have caused the phase transformation, can also accelerate the low-temperature degradation (LTD) of zirconia. LTD is a spontaneous transformation from tetragonal to monoclinic that can occur in the presence of water molecules (Roitero *et al.*, 2018b). LTD can lead to surface roughening and a decrease in the mechanical strength of zirconia, impairing its long-term performance (Chevalier; Cales; Drouin, 1999). In this context, studies have shown that zirconia stabilized with ceria and its composites are much more resistant to LTD (Kohorst *et al.*, 2012). Indeed, the composite used in this work is practically immune to this phenomenon (Reveron *et al.*, 2017). Despite some phase transformation, the monoclinic content in the samples in this study was well below that observed in traditional zirconia surface treatments, such as sandblasting (up to 40%) and zirconia textured with ns laser (up to 10%) (Pereira *et al.*, 2020; Roitero *et al.*, 2017b). Phase transformation is negligible in shorter pulsed lasers (femtosecond, for instance) (Carvalho *et al.*, 2020; Garófalo *et al.*, 2022).

Laser texturing induced hydrophobicity in the samples, as evidenced by the high water contact angles of 139.3 ± 4.4° for 3Y-TZP and 105.8 ± 13.1° for $ZA_8Sr_8Ce_{11}$. This phenomenon can be attributed to the Cassie-Baxter model, which postulates that air pockets are formed between the liquid and the surface due to the increased roughness of the textured features (Cassie; Baxter, 1944). However, hydrophobicity is undesirable for implant applications, since it hinders cell adhesion and osseointegration, which are enhanced by hydrophilic surfaces (Ohtsu *et al.*, 2015). Therefore, further optimization of the laser parameters is needed to modify wettability by changing the geometry of the textured features, such as depth, width, periodicity, and pattern (Ji *et al.*, 2020; Lang; Voisiat; Lasagni, 2019; Pu *et al.*, 2020). These factors can influence the wettability of the surface by altering the mode of liquid-solid interaction from Cassie-Baxter to Wenzel, where the liquid fills the grooves and makes the surface more hydrophilic (Wenzel, 1936). This result contrasts to the WCA measurements of the previous chapter, which demonstrated that ns laser texturing enhances wettability, despite the similar groove size and periodicity. Two effects could have caused such difference: the surface energy, as discussed at Chapter 4, and the surface topography. Open pores and cracks, as observed on the surfaces treated by the ns laser, can exert capillary forces on the liquid, enhancing the wettability.

5.6 CONCLUSION

In this work, the fabrication of micrometric patterns on zirconia (3Y-TZP) and a novel zirconia-based nanocomposite (Ce-TZP/Al_2O_3/$SrAl_{12}O_{19}$) using the Direct Laser Interference

Patterning method with an ultra-short pulsed laser was evaluated. The influence of the laser texturing on the surface microstructure and wettability was also studied. The following conclusions can be drawn from this study:

- Homogeneous and well-defined line-like patterns with a periodicity of 6 μm were successfully produced for both materials.
- The depth of the fabricated structures could be tailored by varying the laser fluence or overlap, reaching depths up to 3 μm. To achieve the same depth, the composite required less energy.
- Cracks and pores only in the nanometer scale could be observed as a result of the laser texturing, much smaller than other defects reported for lasers with longer pulses.
- Laser texturing of 3Y-TZP caused a slight increase in the monoclinic content of 3Y-TZP to ~4%, in contrast to the polished sample that showed no sign of monoclinic phase. On the other hand, the polished sample of $ZA_8Sr_8Ce_{11}$ exhibited a remaining amount of monoclinic phase from the grinding and polishing process (~10%), and the increased value of the textured sample (~15%) can be attributed both at the laser texturing and the manual grinding process.
- The laser texturing increased the water contact angle of the samples, turning them into hydrophobic. For biological applications, a hydrophilic surface is preferable, thus the size of the fabricated features should be tailored to enhance the wettability.

6 INFLUENCE OF LASER PATTERNING ON THE MECHANICAL STRENGTH OF 3Y-TZP AND CE-TZP-BASED NANOCOMPOSITE

6.1 ABSTRACT

Direct Laser Interference Patterning (DLIP) is a fast and accurate technique to produce periodic micrometric features on the surface of ceramic dental implants, but it can induce microstructural damage. The aim of this work was to investigate the effects of DLIP on the surface and mechanical properties of dental grade zirconia (3Y-TZP) and a novel ceria-stabilized zirconia-based nanocomposite (Ce-TZP/Al_2O_3/$SrAl_{12}O_{19}$). An infra-red nanosecond laser source was employed to produce the periodic pattern on the surface of pressed and sintered discs. The samples were also subjected to accelerated aging and mechanical cycling protocols that simulate a life span of 10 years of clinical use. The surface topology and morphology, the cross-sectional microstructure, and the crystallographic changes of the textured region were analyzed using confocal microscopy, scanning electron microscopy, and X-ray diffractometry, respectively. Linear structures with a 6 µm periodicity were successfully produced on both materials using DLIP. The results showed that DLIP induced defects and heterogeneities on the surface and subsurface of both materials, such as variability in the groove depth, recrystallized layer, microcracking, and porosity. DLIP also triggered some tetragonal to monoclinic transformation on 3Y-TZP, which was further enhanced by aging or mechanical cycling. Conversely, DLIP reduced the monoclinic content on the composite surface, which remained stable after the post-treatments. Although no significant reduction in the flexural strength was observed on the 3Y-TZP laser textured samples, they presented a lower standard deviation, indicating higher reliability. On the other hand, DLIP reduced the flexural strength of the composite by about 40%, which could be attributed both to the laser-induced defects and the removal of the compressive layer formed during the polishing process. Flexural strength of both materials was not significantly affected by the mechanical cycling and accelerated aging. Therefore, DLIP is a feasible method to create micrometric patterns on zirconia and zirconia-based composites, but it requires careful optimization to minimize the detrimental effects on their mechanical performance.

6.2 INTRODUCTION

Tetragonal zirconia polycrystal stabilized with 3 mol% of yttria (3Y-TZP) is a ceramic oxide that has been extensively studied and used in the biomedical field due to its excellent mechanical strength (up to ~1500 MPa), chemical stability, biocompatibility, and aesthetics (Chevalier, 2006). The addition of yttria as an oxide stabilizer induces a metastable tetragonal phase in zirconia, which can transform to monoclinic under stress, resulting in a volumetric expansion that generates compressive stresses at the crack tips. This phenomenon hinders crack growth and results in its high toughness (~6 MPa√m) compared to other traditional ceramics. Furthermore, zirconia exhibits a similar osseointegration rate and lower bacterial adhesion compared to titanium, which is considered the "gold standard" in orthopedic and dental implants (Depprich *et al.*, 2008; Nascimento *et al.*, 2014). However, dental grade zirconia (3Y-TZP) is susceptible to low-temperature degradation (LTD), a spontaneous phase transformation (from tetragonal to monoclinic) that occurs in humid environments and can lead to surface roughening and strength degradation (Lughi; Sergo, 2010). Furthermore, despite its high toughness relative to other ceramics, 3Y-TZP still shows a brittle fracture behavior and a large variability in the strength values, requiring the use of statistical failure approaches (Chevalier *et al.*, 2020).

Surface modification of biomaterials has been extensively studied to enhance their biological behavior. Conventional surface treatments of implants, such as acid etching and sandblasting, aim to increase their roughness and create a mechanical anchorage with the bone tissue, improving their primary and long-term stability (Buser *et al.*, 1991). However, these treatments allow only the fabrication of random features with low-dimensional control, while recent studies suggest that controlled patterns in the micro- and nanometer range can optimize surface wettability, guide cell growth, and decrease bacterial attachment (Quinn *et al.*, 2020; Soon *et al.*, 2016). In this context, laser technology has emerged as a promising tool to improve the antibacterial and osseointegration properties of implants, due to its high resolution, repeatability, and flexibility, enabling the fabrication of patterns with different sizes (from micro- to nanometer scale) on various materials. Among the laser techniques, Direct Interference Laser Patterning (DLIP) takes advantage of the light interference phenomenon to generate periodic micro- and nanopatterns in a single-step process (Lasagni *et al.*, 2017). In this technique, the laser beam is split into two or more sub-beams, which are superposed on the material surface, creating an interference pattern that depends on the number of sub-beams, the angle between them, and their polarization. For instance, a line-like intensity distribution can be obtained for two sub-beams, where ablation occurs mainly at the intensity maxima, resulting in a periodic texture of lines. DLIP is a well-established method to functionalize metallic surfaces, but studies on the patterning of ceramic materials and its influence on their mechanical reliability are still scarce (Fabris *et al.*, 2019; Mulko; Soldera; Lasagni, 2022). The effect of DLIP on the mechanical and aging behavior of dental-grade zirconia has been investigated by Roitero et al. (Roitero *et al.*, 2018b, 2018a). They reported that DLIP can reduce the mechanical strength and resistance to LTD due to the damage, such as cracking and phase transformation, caused by laser texturing. The thermal damage induced by short-pulsed lasers (nanosecond or longer) results in recrystallization of the surface and intergranular cracking, as well as melting and residual stresses (Roitero *et al.*, 2017b). Only when using an ultra-short pulsed laser (picosecond or shorter), DLIP can produce well-defined structures with minor damage on the zirconia surface, such as some porosity and microcracking (Henriques *et al.*, 2023a, 2023b; Müller *et al.*, 2020). In addition to the direct damage to the mechanical strength, the ablated grooves and possible microcracks caused by the laser energy can also offer a path for water to penetrate the subsurface and accelerate aging. Residual stresses produced by the laser thermal load can also accelerate the aging process (Wei; Gremillard, 2018). Although it also has been demonstrated that mechanical cycling does not significantly influence the mechanical strength of polished zirconia (Borchers *et al.*, 2010), the presence of preexisting defects, such as those induced by the laser processing, can nucleate cracks and potentialize the effects of mechanical cycling. Cyclic loading can result in accumulated plastic damage, phase transformation, and slow subcritical crack growth (Chevalier; Olagnon; Fantozzi, 1999; Studart *et al.*, 2007).

In recent years, novel high-toughness ceramic-based composites have been developed to withstand high stresses even in the presence of major defects. Ceria-stabilized zirconia (Ce-TZP) undergoes a large amount of stress-induced phase transformation, and when combined with immiscible second and third phases that inhibit grain growth and enhance toughness by bridging/crack-deflection, it achieves an outstanding balance between mechanical strength and high toughness (Chevalier *et al.*, 2020; Reveron *et al.*, 2017). In a recent study, a composite consisting of 84 vol% Ce-TZP, 8 vol% Al_2O_3, and 8 vol% $SrAl_{12}O_{19}$ was shown to surpass 1 GPa of mechanical strength and 10 MPa√m of toughness (Reveron *et al.*, 2017). Indeed, with such high toughness, the ductility and strength of the material is not significantly affected by processing defects with size up to 150 μm (Chevalier *et al.*, 2020). Furthermore, Ce-TZP-based composites are virtually immune to LTD (Kohorst *et al.*, 2012). These characteristics make them promising candidates in structural applications, including orthopedic and dental implants, especially when their manufacturing process imposes defects.

The objective of this study is to investigate the effect of laser texturing using DLIP on the mechanical strength of dental grade zirconia and the novel nanocomposite Ce-

TZP/Al_2O_3/$SrAl_{12}O_{19}$. Biaxial flexural tests were conducted before and after mechanical cycling and simulated aging. The microstructure of the textured surfaces was also examined to correlate the measured mechanical strength with the changes induced by the laser texturing and the presence of defects.

6.3 MATERIALS AND METHODS

6.3.1 Samples fabrication

This study employed commercial zirconia powder doped with 3mol% yttria (TZ-3YSB Tosoh, Japan) and the composite Ce-TZP/Al_2O_3/$SrAl_{12}O_{19}$ (composition: 84 vol% ZrO_2 (stabilized with 11 mol% CeO_2), 8 vol% Al_2O_3 and 8 vol% $SrAl_{12}O_{19}$; DOCERAM, Germany). For the sake of simplicity, this composite material will be denoted as $ZA_8Sr_8Ce_{11}$ from now on. Using steel dies, the powders were subjected to uniaxial pressing to shape them into discs, applying a pressure of 100 MPa for 3Y-TZP samples and 70 MPa for composite, each for 60 seconds, to produce the initial green compacts. Subsequently, the samples were subjected to sintering at temperatures of 1500°C for 2 hours (3Y-TZP) and 1450°C for 1 hour ($ZA_8Sr_8Ce_{11}$), conducted within a high-temperature furnace (Sinter F-1800 10P, EDG) under ambient air conditions. After sintering, the samples were ground and polished with diamond particles down to a grit size of 1 µm to achieve a smooth and flat surface. The final dimension of the sintered discs was 16.9 mm in diameter and 1.6 mm thick.

6.3.2 Laser texturing

The samples were textured using a DLIP workstation (Fraunhofer IWS/TU Dresden, Germany) equipped with an infra-red (1064 nm) nanosecond slab-shaped solid-state laser source (Edgewave InnoSlab – IS400–3-GH, Würselen, Germany). The laser source has a pulse duration of 10 ns, a repetition rate of 5 kHz, and a maximum output power of 150 W. The DLIP optical head divides the laser beam into two sub-beams using prisms, and overlaps and focuses them on the material surface, as depicted in Figure 6.1A. The optics also elongate the beam geometry, turning it into a rectangular shape with a spot size at the focus position with dimensions of 100 µm in the Y-direction and 5 mm in the X-direction. This configuration produces a line-like periodic pattern, where material is removed at the regions where the energy is maximum (Figure 6.1B). The periodicity Λ of the generated pattern (distance between consecutive lines) can be calculated according to Equation 6.1, which correlates the half angle between the sub-beams θ and the laser wavelength λ. In this study, the beams overlap at an angle of 5.1°, leading to a periodicity of 6 μm.

$$\Lambda = \frac{\lambda}{2\sin\theta} \tag{6.1}$$

The texturing strategy involved moving the sample in the Y-direction to texture a single line, then moving the sample in the X-direction to texture subsequent lines, covering the whole sample, as illustrated in Figure 6.1C. The sample displacement is controlled by high-precision positioning axes (Aerotech, USA). The separation between pulses in the Y-direction (PtPd) was set as 2.5 μm for both materials. For the 3Y-TZP samples, the distance between lines, or hatch distance (Hd), and the fluence were set as 1.18 mm and 2.18 J/cm², respectively. For the composite, the hatch distance was 1.593 mm and the fluence 1.38 J/cm².

Figure 6.1 - Illustration of the (a) DLIP optical setup, (b) the interference region formed under the sub-beams, and (c) the texturing strategy, which consisted of moving the sample in the y-direction by a distance PtPd for each laser pulse until a complete line is textured, then moving the sample in the x-direction by a distance Hd to texture subsequent lines.

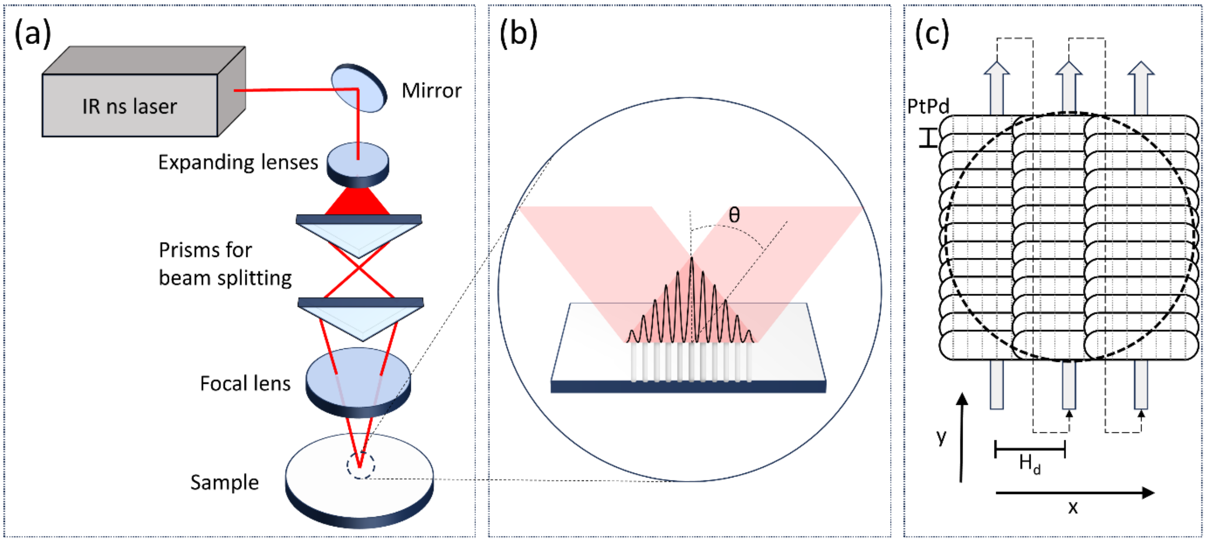

Source: Author.

6.3.3 Surface characterization

The surface morphology and microstructure of the textured samples were examined using a Scanning Electron Microscope (SEM) (Hitachi TM-3030, Japan) at an accelerating voltage of 15.0 kV. Additionally, cross-section analysis was conducted using a Focused Ion Beam/Scanning Electron Microscope workstation (FIB/SEM, NVision 40; Carl Zeiss

Microscopy GmbH, Germany), combining an SIINT zeta FIB column (Seiko Instruments Inc. NanoTechnology, Japan) with a Gemini I column. The average depth of the textured grooves was calculated using the software SensoMap (Sensofar, Spain), based on topographical data acquired by a confocal microscope (Sensofar S Neox, Spain).

6.3.4 Aging and mechanical cycling

The control (polished) and textured samples were divided into three different groups for each material before subsequent tests: (1) no further treatment; (2) accelerated aging; and (3) mechanical cycling. The accelerated aging and mechanical cycling aim to mimic the microstructural damage that dental materials could be subjected to during clinical use. The samples subjected to accelerated aging were exposed to steam at 134 °C under 2 bars for 5 h in an autoclave (Ortosintese AC365, Brazil). In the mechanical cycling groups, the samples were placed in a ball-on-three-balls apparatus (more details in section 6.3.6) and subjected to a vertical load of 50 N for 1,200,000 cycles at a frequency of 1.6 Hz using a mechanical cycling machine (Biocycle – Biopdi, São Carlos/SP, Brazil). These conditions correspond approximately to 10 years under clinical use (Amarante *et al.*, 2020; Kessler *et al.*, 2021).

6.3.5 X-Ray Diffractometry

Crystallographic analyses were performed in one sample of each group using an X-ray diffractometer (XRD) equipped with a Cu-Kα source (Rigaku Miniflex 600, Japan). The XRD spectra were acquired over a 2θ range between 20° and 80° at a step size of 0.05° and a scan speed of 5°/min. The monoclinic fraction in relation to the tetragonal phase was calculated using the Toraya equation (Toraya; Yoshimura; Somiya, 1984), considering the maximum intensity of the peaks.

6.3.6 Mechanical tests

Biaxial flexure strength (BFS) tests were performed in 10 samples of each group using a ball-on-three-balls apparatus, where the sample is supported by three hardened steel balls (arranged 120 degrees apart and forming a 10 mm diameter support circle) and loaded at the center of the top surface by another steel ball. The specimens were loaded using a universal testing machine (Instron-EMIC 23-5S, USA) at a crosshead speed of 1 mm/min until failure. The polished/textured surfaces were positioned to the tensile side (downside). The maximum applied load before failure was recorded and the biaxial flexural strength was calculated according to ISO 6872 (ISO 6872:2015, 2015). According to this standard, the biaxial flexure strength is given by the following equations:

$$\sigma = \frac{-0.2837P(X-Y)}{t^2} \tag{6.2}$$

$$X = (1+\nu)ln\left(\frac{c^2}{R^2}\right) + \left(\frac{1-\nu}{2}\right)\left(\frac{c^2}{R^2}\right) \tag{6.3}$$

$$Y = (1+\nu)\left[1 + ln\left(\frac{a^2}{R^2}\right)\right] + (1-\nu)\left(\frac{a^2}{R^2}\right) \tag{6.4}$$

where σ is the maximum tensile stress (MPa), P is the failure load (N), ν is the Poisson's ratio, R is the radius of the sample, a is the radius of the circle formed by the three supporting balls, and c is the radius of the piston applying the load. The geometric parameters are given in mm.

6.3.7 Statistical analysis

The BFS results were analyzed using two-way ANOVA followed by Tukey test (p=0.05) to detect statistically significant differences and interactions between the groups (polished vs. textured; no post-treatment vs. aging vs. cycling). The Weibull parameter m and the characteristic strength σ_0 were also calculated based on Equation 6.5.

$$P_f(\sigma_c) = 1 - exp\left[-\left(\frac{\sigma_c}{\sigma_m}\right)^m\right] \tag{6.5}$$

Where P_f is the probability of failure for a biaxial stress σ_m. The characteristic strength σ_0 is the strength corresponding to a failure probability of 63.2%, and the parameter m reflects the reliability of the material. Due to the low number of samples (N=10), this analysis won't be able to provide an accurate value of the Weibull parameters, but rather an approximation that can be used to compare the different groups.

6.4 RESULTS

6.4.1 Surface analysis

Line-like periodic structures were successfully fabricated for both materials using the nanosecond laser. Figure 6.2 shows SEM images of the textured surface of the 3Y-TZP (a) and the composite (b). The fabricated structures are well-defined, with a clear distinction between grooves and ridges, but defects associated with the thermal mechanism of ablation, such as melting, are also noticeable. Surface porosity can also be observed, especially in the 3Y-TZP. The structures are also heterogeneous, with resolidified material accumulating over the surface and partially covering some grooves. The morphology of the ridges (at the interference minima) suggested that the temperature exceeded the melting point of both 3Y-TZP and $ZA_8Sr_8Ce_{11}$, resulting in their melting and/or ablation. This implies that the entire surface layer was modified by the laser. The average groove depth measured from the confocal analysis was 0.78 ± 0.32 µm for the 3Y-TZP and 0.83 ± 0.42 µm for the $ZA_8Sr_8Ce_{11}$. The large standard deviation highlights the heterogeneity of the grooves' sizes. The calculated roughness (Sq) was ~750 nm for both materials.

Figure 6.2 - Morphology of the textured samples of (a) 3Y-TZP and (b) ZA8Sr8Ce11.

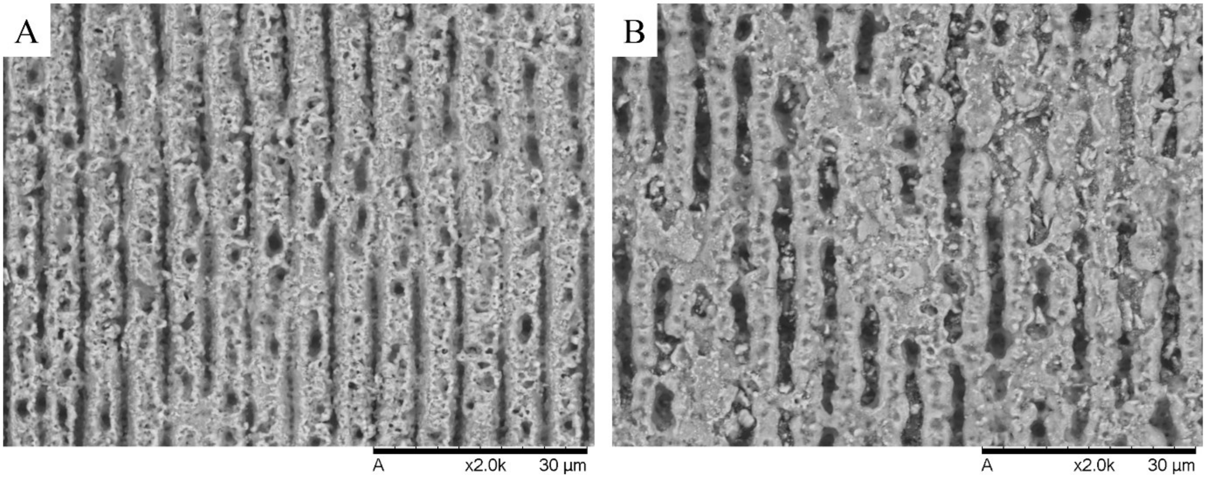

Source: Author.

Figure 6.3 shows the SEM images of the cross-sections produced by the FIB for the monolithic zirconia (a,b) and the composite (b,c). Both materials show heterogeneity in the depth of the fabricated structures, which corroborates with the images from the surface. The bulk of the material is homogeneous and has equiaxial grains, but some porosity can be observed especially for the composite, which can be attributed to the manufacturing process (pressing/sintering). The grains are slightly larger and more elongated perpendicular to the surface just below the textured region, indicating recrystallization. The images also reveal intergranular cracking originating both at the surface and sub-surface of the textured region, mainly orthogonal to the surface. In addition to the porosity found on the bulk material, larger pores can also be observed near the textured surface, which are attributed to the texturing process. These defects are present both in the grooves and ridges.

Figure 6.3 - Cross-section images of the textured surface of the (A, B) 3Y-TZP and (C, D) $ZA_8Sr_8Ce_{11}$. Microcracking, porosity, and recrystallization can be observed on the surface.

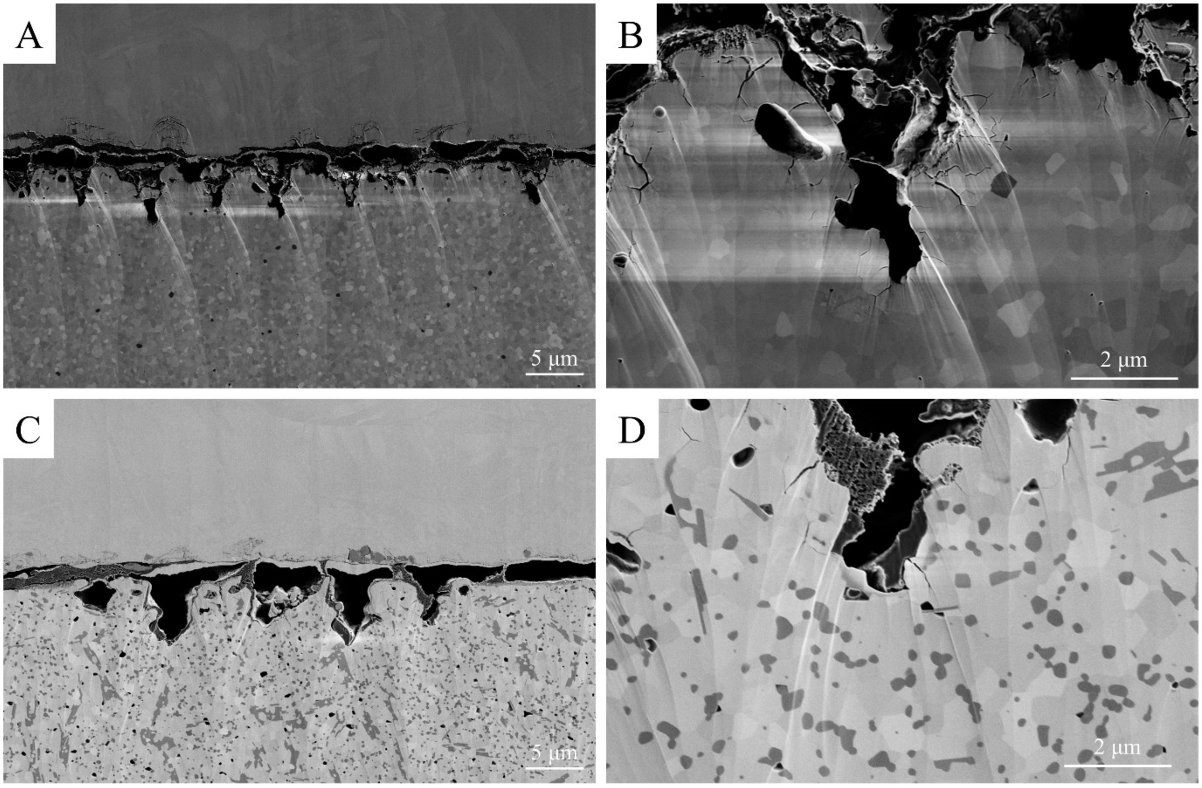

Source: Author.

6.4.2 X-Ray Diffractometry

Figure 6.4 shows the XRD diffractograms of the polished and laser-textured samples with or without post-treatments for both 3Y-TZP and $ZA_8Sr_8Ce_{11}$, where t and m represent tetragonal and monoclinic phase peaks. Regarding the dental-graded zirconia, the polished sample presented no sign of a monoclinic phase before the aging and mechanical cycling tests. However, two small peaks, at ~29° and ~32°, related to the monoclinic phase, could be observed after the treatments, indicating t→m transformation. The laser texturing process also induced some t→m transformation, resulting in a monoclinic content of ~5%. Interestingly, the post-treatments caused a substantial tetragonal to monoclinic transformation, reaching a monoclinic content of 30% after the simulated aging and 18% after the cycling protocol. Regarding the composite, the polished group exhibited some monoclinic content (around 10%), a value that did not change considerably after the mechanical cycling or aging tests. On the other hand, the laser texturing reduced the monoclinic content on the surface to less than 2%. The tetragonal peak at ~31° is also slightly broader for the composite polished samples compared to the textured ones. The simulated aging and fatigue also did not substantially influence the monoclinic content on the composite textured sample. The monoclinic content of all groups calculated by the Toraya equation is shown in Table 6.1.

Figure 6.4 - X-ray diffractograms of all tested groups.

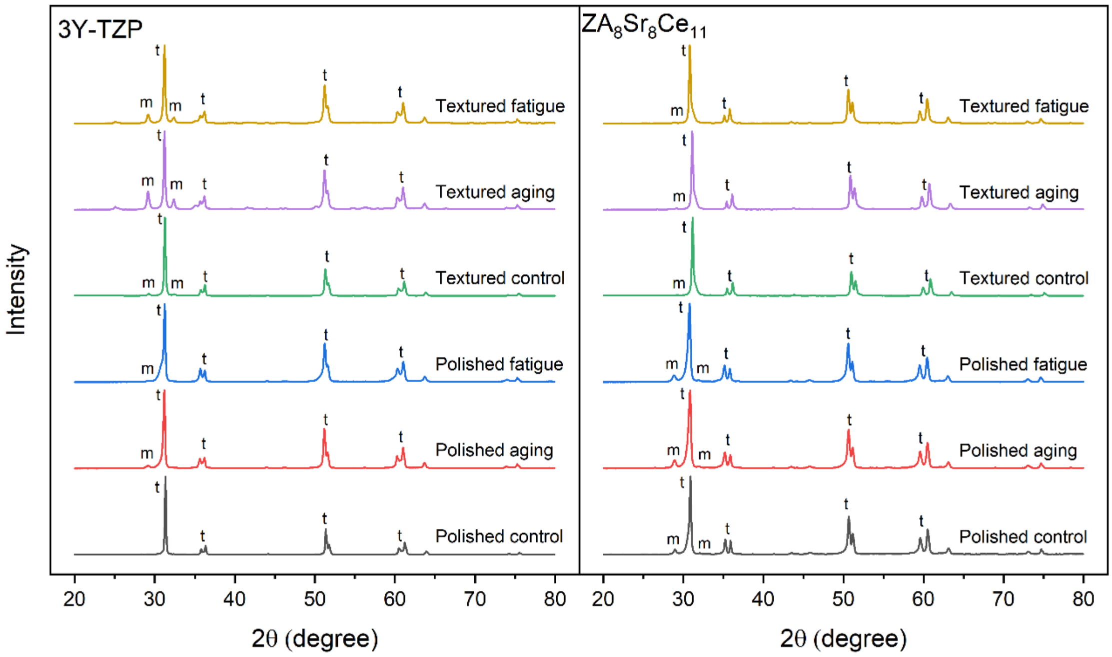

Source: Author.

Table 6.1 - Calculated monoclinic content for all tested groups.

			Monoclinic content (vol.%)
3Y-TZP	Polished	Control	0%
		Aging	4.4%
		Fatigue	1.4%
	Textured	Control	5.4%
		Aging	30.8%
		Fatigue	18.4%
ZA$_8$Sr$_8$Ce$_{11}$	Polished	Control	9.4%
		Aging	12.2%
		Fatigue	10.6%
	Textured	Control	1.4%
		Aging	2.5%
		Fatigue	1.3%

Source: Author.

6.4.3 Mechanical tests

The results from the biaxial flexural strength tests are summarized in Figure 6.5(a) and Figure 6.5(b) for the monolithic zirconia and the composite, respectively. Although the XRD showed some phase transformation on zirconia after the fatigue and aging tests, they did not significantly influence the biaxial strength. The statistical analysis also showed no influence of the laser texturing on the average biaxial strength. However, the standard deviation is much smaller after the laser texturing, i.e., the samples fractured with similar values of stress. This fact can be confirmed by calculating the Weibull modulus *m*, which measures the variability in strength (higher *m* means lower variability). The polished groups presented values of *m* around 4~6, while for the textured groups, *m* increased up to 20. On the other hand, the laser texturing caused a 35~40% decrease in the flexural strength of the composite discs, which was statistically significant. However, as in the 3Y-TZP samples, a smaller variability was observed on the textured samples, which presented a Weibull modulus of around ~20, in contrast to a value of ~5 for the polished groups. Statistical analysis also showed no significant influence of the post-treatment on the mechanical strength of the composite.

Figure 6.5 - Average flexural strength and standard deviation for all tested groups of the 3Y-TZP (a) and the ZA$_8$Sr$_8$Ce$_{11}$ (b).

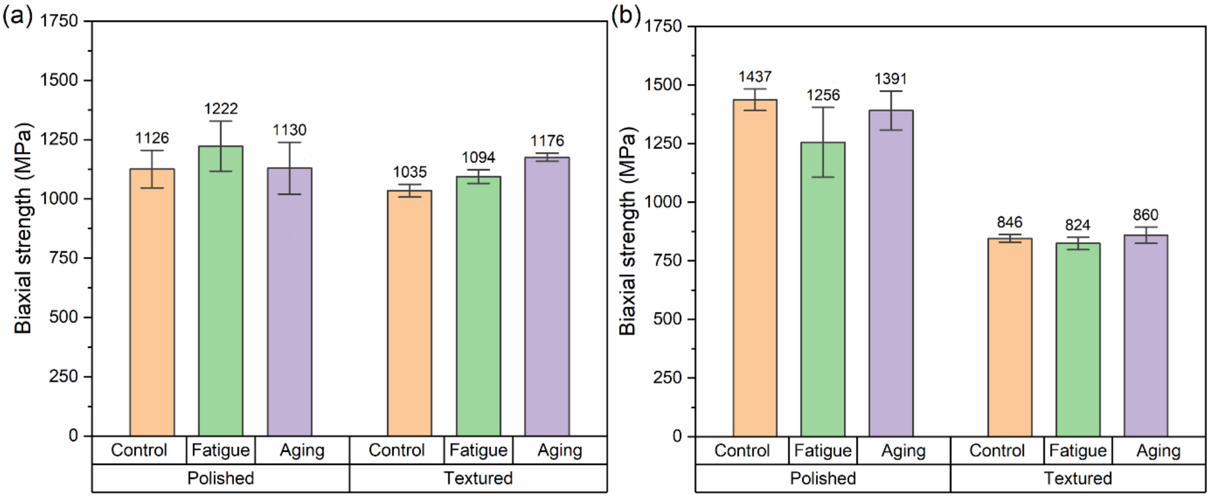

Source: Author

6.5 DISCUSSION

This study demonstrated that Direct Laser Interference Patterning with a nanosecond laser can be applied to create micrometric features on the surface of 3Y-TZP and ZA$_8$Sr$_8$Ce$_{11}$ without causing significant microstructural damage and affecting their mechanical strength. Line-like grooves with an average depth of ~0.8 μm and periodicity of 6 μm were fabricated over the entire sample for both materials in a fast-manufacturing process. In comparison, the conventional Direct Laser Writing technique would require a complex optical setup to focus the laser beam in such small spots, and the processing time and cost would be significantly increased (Stark *et al.*, 2019).

Laser texturing of zirconia with nanosecond or longer pulsed laser is often associated with thermal damage on the surface due to its mechanism of ablation. Short-pulsed lasers (ns or longer) remove material mainly by photothermal ablation, where the material is heated and evaporated or ablated by the recoil pressure of the liquid phase (Daniel *et al.*, 2008). However, heating also causes thermal defects, such as recrystallization, remolten later, and microcracking, as observed in the SEM images. The cross-section images revealed the microstructural changes induced by the DLIP in the zirconia and composite samples. The grains in the first surface layer were slightly larger and more elongated than those in the bulk, indicating that the surface underwent melting and recrystallization. Intergranular microcracking, with lengths of less than ~1 μm, was also observed in the surface and sub-surface. Microcracking can be attributed to high local stresses generated by the steep thermal gradient caused by the laser, and they are often found in the laser processing of zirconia (Jing *et al.*, 2020; Morales *et al.*, 2023; Parry *et al.*, 2008). Furthermore, the porosity observed on the surface and sub-surface of both materials can be attributed to localized evaporation or ablation of inhomogeneities in the bulk material, such as closed pores or phases with lower ablation threshold (Müller *et al.*, 2020). Similar microstructural defects were found in a similar study that used a UV nanosecond DLIP to texture zirconia (Roitero *et al.*, 2017b), however, the present study showed a higher definition of the textured grooves.

The XRD analyses confirmed some phase transformation from tetragonal to monoclinic after the laser texturing in the 3Y-TZP sample. Monoclinic transformation can be associated with thermal residual stresses developed during the laser treatment and high local stresses at the microcracks tip (Chevalier *et al.*, 2009). However, the monolithic zirconia remained predominantly tetragonal, with only 5% of monoclinic content, a value lower than other conventional surface treatments, such as sandblasting, that can present up to 40% of monoclinic phase (Pereira *et al.*, 2020). A higher degree of t→m transformation (up to 10%) was reported in other works using nanosecond laser to texture zirconia (Pereira *et al.*, 2020; Roitero *et al.*, 2017b), while lower content of monoclinic phase is usually achieved only using shorter pulses (femtosecond laser) (Delgado-Ruíz *et al.*, 2011). The aging and fatigue protocols caused only a small amount of tetragonal to monoclinic transformation on the polished 3Y-TZP sample. The polished surface, due to its lower surface area in contact with the water steam and absence of surface defects, such as microcracks, has an increased resistance to LTD. On the other hand, the post-treatments substantially increased the monoclinic fraction of the textured samples. Regarding the aging, two factors could have contributed to the accelerated phase transformation: (1) the textured samples have a higher surface area, which means that more material is exposed to water molecules and susceptible to phase transformation; and (2) the microcracks, observed in the cross-section images, offer pathways to water to penetrate the subsurface, meaning that more layers of material can be reached by water molecules and transformed into monoclinic phase. Furthermore, high stresses are developed at the tip of these microcracks when load is applied, even for low forces as used during the cycling tests, which can trigger phase transformation. On the other hand, the $ZA_8Sr_8Ce_{11}$ samples presented a different behavior. The polished samples showed some (~9%) monoclinic content, which can be related to tetragonal to monoclinic phase transformation occurring during the mechanical stresses of grinding (Muñoz-Tabares *et al.*, 2011). Despite undergoing similar grinding and polishing conditions as the 3Y-TZP samples, Ce-TZP-based nanocomposites have a higher transformability under applied stress, which could have resulted in a higher monoclinic content (Chintapalli *et al.*, 2013). Furthermore, the polished samples presented broader tetragonal peaks, which can be related to compressive stresses induced by the polishing (De Souza *et al.*, 2020). Nonetheless, the laser texturing decreased the monoclinic content on the surface, indicating that the transformed layer was partially removed, and only a small amount (~2%) of the monoclinic phase either remained from the grinding process or was transformed by the laser processing. Although the aged samples for both polished and textured conditions presented a slightly higher amount of monoclinic phase, their increase might be not due to only the treatments. The manual process of grinding/polishing can result in slightly different amounts of monoclinic phase in different samples, thus more samples should be tested to draw an appropriate conclusion. However, the fact is that the post-treatments on the textured surface had a much smaller influence on the monoclinic content than in the monolithic zirconia, highlighting the excellent crack propagation and LTD resistance of the composite (Benzaid *et al.*, 2008).

According to the Griffith failure criteria, brittle materials such as zirconia tend to fracture when the stress intensity factor K, defined as $K = \sigma Y \sqrt{\pi a}$, exceeds the fracture toughness K_{IC} at any crack-like flaw. In this equation, σ is the applied stress, Y is the crack geometric factor, generally on the order of unity for most situations, and a is the crack size. As the material volume of dense ceramic materials presents a random distribution of flaws, the recorded failure stresses of each sample from the same group are slightly different, following a Weibull distribution. The laser texturing induced three types of geometric modifications on the surface that act as flaws and may have influenced the strength of the materials: (1) the textured grooves; (2) microcracking around the grooves; and (3) porosity generated by the laser or by enlargement of preexisting pores. These defects produced by the laser had a relatively uniform distribution and size on the surface, which resulted in a smaller range of strength values for each group. Despite the low number of samples for each group (N=10), the calculated Weibull parameter *m* varied from 4~6 for the polished groups up to ~20 for the textured groups, indicating higher reliability when the laser patterning is applied. For the 3Y-TZP, no significant change in the mechanical strength was observed after the laser texturing, which implies that the severity of the defects generated by the laser was comparable to those from the polished surfaces. In contrast, the flexural strength of $ZA_8Sr_8Ce_{11}$ textured samples decreased significantly by ~40% after the laser texturing. In addition to the defects induced by the laser texturing, another factor that could have influenced this result is a potential compressive layer generated by the laser, as previously discussed. The compressive layer absorbs part of the tensile load and hinders crack propagation, increasing the mechanical strength of the material (De Souza *et al.*, 2020). In fact, other studies reported the flexural strength of pressed and sintered $ZA_8Sr_8Ce_{11}$ was around 800 MPa, which is similar to the values observed in the textured samples (Chevalier *et al.*, 2020; Reveron *et al.*, 2017). Therefore, it is not possible to quantify the effect of laser texturing on the mechanical strength and reliability of the composite, as there is another simultaneous phenomenon.

The mechanical strength of the textured samples was not affected by the microstructural changes induced by aging and mechanical cycling, especially the tetragonal-to-monoclinic (t→m) transformation. Similar results were reported by Alghazzawi et al., who found no significant difference in strength between aged 3Y-TZP samples with ~21% monoclinic phase and control samples with ~2% monoclinic phase (Alghazzawi *et al.*, 2012). Borchers et al. also investigated the effect of different conditions, such as mechanical cycling and aging, on the strength of 3Y-TZP and observed that the increase in monoclinic content induced by these procedures did not compromise its mechanical resistance (Borchers *et al.*, 2010). This can be attributed to the fact that the phase transformation occurs predominantly at the surface of fully dense zirconia, where the volume expansion can be accommodated by the free surface, resulting in negligible internal stresses (Chevalier; Gremillard; Deville, 2007). If the transformation zone does not penetrate the bulk of the material, the bulk properties are not affected. Aging becomes more detrimental to the mechanical properties when water molecules can reach the bulk of the material, through open porosity or cracking, for instance, causing phase transformation also in the internal surfaces, which can generate internal stresses. Although the XRD analysis revealed that the laser texturing increased the surface area exposed to water and thus enhanced the phase transformation, it did not significantly reduce the material strength. Therefore, the texture and associated microcracks are not deep enough to extend the transformation zone into the bulk of the material and affect its strength.

Other works also showed no influence of mechanical cycling, in both dry and wet environments, in the flexural strength of Y-TZP, even using higher loads (>80 N) than the present study (50 N) (Curtis; Wright; Fleming, 2006; Pittayachawan *et al.*, 2007). The hypothesis that either the microstructural changes and defects caused by the laser texturing could accelerate crack growth during mechanical cycling and negatively affect the zirconia strength was not confirmed. Thus, the DLIP should not impair the mechanical reliability of zirconia/zirconia-based nanocomposites dental implants considering a life span of 10 years. However, further tests could be conducted by combining mechanical cycling in a wet environment, which is a critical condition for zirconia, leading to subcritical crack growth. This phenomenon occurs when crack propagation happens at stresses lower than the threshold for crack growth due to the interaction of water molecules with the ceramic bonds at the crack tips (Chevalier; Olagnon; Fantozzi, 1999). Consequently, the repeated loading of zirconia in a wet environment could potentially lead to earlier failure at a significantly lower stress.

6.6 CONCLUSION

The influence of Direct Laser Interference Patterning using an infra-red nanosecond laser on the microstructure and mechanical strength of dental-grade zirconia (3Y-TZP) and a novel zirconia-based nanocomposite (Ce-TZP/Al_2O_3/$SrAl_{12}O_{19}$) was evaluated in this study. The effect of accelerated aging and mechanical cycling on the polished and textured samples was also studied. The following conclusions can be drawn from this study:

- Line-like patterns with a periodicity of 6 μm and an average depth of approximately 0.8 μm were successfully fabricated for both materials using the DLIP technique.
- The microstructural analysis revealed defects related to the thermal mechanism of ablation in the textured samples, such as a recrystallization layer, intergranular cracks with less than 1 μm, and porosity in the sub-surface.
- X-ray diffractometer analysis revealed that laser texturing causes a slight increase in the monoclinic content on 3Y-TZP (~5%), however, it accelerated the tetragonal to monoclinic transformation when the sample was subjected to aging or mechanical cycling. On the other hand, laser texturing of the $ZA_8Sr_8Ce_{11}$ composite decreased the

monoclinic content remaining from the polishing process, and it was not significantly affected by the post-treatments.

- This study showed that DLIP did not affect the flexural strength of 3Y-TZP significantly, but it improved its reliability by reducing the standard deviation. However, laser texturing reduced the flexural strength of the composite by about 40%, which can be attributed to both laser-induced defects and the removal of a compressive layer generated by the polishing process. The post-treatments (aging and cycling) did not significantly affect the mechanical strength of both materials.
- These findings demonstrated that DLIP is a viable method to create micrometric patterns on the surface of zirconia and zirconia-based composites without inducing substantial damage and affecting their mechanical reliability, even when subjected to clinical conditions.

7 GENERAL CONCLUSIONS

This thesis examined the influence of laser texturing on the surface characteristics, microstructure, mechanical behaviour and biological performance of conventional zirconia 3Y-TZP and the zirconia-based nanocomposite Ce-TZP/Al_2O_3/$SrAl_{12}O_{19}$. Two laser techniques were employed: direct laser writing (DLW) and direct laser interference patterning (DLIP). Additionally, the DLIP technique was compared using two laser sources: a nanosecond (ns) laser and a picosecond (ps) laser. Within its limitations, the main findings of this study are:

- Laser texturing is a viable method to create controlled grooves on the surface of zirconia-based ceramics, which can enhance their biological response. The grooves can be tailored in terms of shape, size, spacing and orientation by adjusting the laser parameters and technique. However, the parameters should be carefully selected to avoid defects caused by insufficient or excessive energy, such as heterogeneities, melting, phase transformation and cracking.
- The parametric study conducted using the DLW technique with a ps laser allowed the comparison between both materials regarding laser interaction and effects. Regardless the material, well-defined and defect-free grooves were successfully ablated with proper selection of laser parameters. The composite allowed the fabrication of wider and deeper grooves (up to 30 µm wide and 26 µm deep) compared to the traditional zirconia (up to 12 µm wide and 6 µm deep) for the studied conditions, leading to a material removal rate up to 10 times higher. However, the 3Y-TZP presented ablation for lower energy levels. Despite using an ultra-short pulsed laser source, defects related to thermal ablation, such as melting and cracking, were observed for high values of fluence or number of pulses hitting the same spot.
- Direct Laser Interference Patterning with a picosecond laser results in a more homogeneous and defectless textured surface compared with a ns laser. The ps laser produces smoother grooves with less pores, cracks and recast layers, which can reduce the risk of fatigue and premature failure. Conversely, the nanosecond laser resulted in defects related to thermal mechanisms of ablation, such as resolidified material and cracking. Despite having similar grooves depth and periodicity, the texture generated by the nanosecond enhanced the wettability, while the picosecond laser increased the hydrophobicity. Differences on the surface morphology, such as the presence of pores and cracks, and chemistry could have caused the distinct behavior. Nonetheless, regardless of the pulse duration and the material, DLIP was able to produce

homogeneous micrometric periodic patterns without large defects or significant phase transformation with periodicity of 6 μm and depths of ~1 μm.

- Laser texturing does not significantly affect the mechanical resistance of traditional zirconia. The flexural strength of the textured samples is comparable to those of the untextured ones, indicating that the laser-induced defects are negligible. Moreover, the strength standard deviation of the samples decreased after laser texturing, indicating higher reliability. The texturing also accelerated tetragonal to monoclinic transformation when the samples were exposed to aging or mechanical cycling, but this phenomenon did not influence their mechanical strength. On the other hand, laser texturing reduced the flexural strength of the composite by about 40%, which can be attributed to both laser-induced defects and removal of a compressive layer generated by the polishing process. A decrease on the monoclinic content was observed on the composite after laser texturing, but further phase transformation was not observed after cycling and aging, which also did not affect its mechanical strength.

The results of this study provide valuable insights into the optimization of laser texturing parameters and techniques for zirconia ceramics, as well as the understanding of the underlying mechanisms and the implications for the material performance. The outcomes of this research can contribute to the development of novel and improved zirconia-based implants with enhanced biocompatibility and reliability.

7.1 FUTURE WORK

Based on the results presented in this thesis, the following research ideas are proposed to further investigate the effect of laser micro-patterning on the microstructure, mechanical reliability and biological response of zirconia and zirconia-based nanocomposites:

- Optimization of the geometry of the ultra-short (ps) pulsed laser textured features to enhance the surface wettability. The picosecond laser source produced a more homogeneous surface and less microstructural defects in comparison to the nanosecond laser, however it reduced the wettability, which is undesirable for implants. Changing the size of the fabricated features can alter the wetting behavior and optimize it for biological applications. After enhancing the wettability, further biological and mechanical tests can also be performed on the ultra-short textured samples to verify the influence of the homogeneous and well-defined patterns, in contrast to heterogeneous surface textured by the nanosecond laser.

- Further investigation on the effects of laser texturing on the mechanical strength of the $ZA_8Sr_8Ce_{11}$ composite. The present study indicated that, besides the laser processing, the grinding and polishing step could have affected the microstructure, generating a compressive layer that increased the mechanical strength of the control group. A thermal treatment to achieve stress relief or even recrystallization can be performed to homogenize the microstructure of all samples, and isolate the effects from the laser texturing. A fractography study can also be performed in both composite and 3Y-TZP to understand how the laser texturing can affect the fracture origin. Furthermore, a larger number of samples (at least 30) could be tested to provide an accurate Weibull analysis and estimation of Weibull parameter m.
- Investigation on the biological response of laser patterned surfaces. Although a preliminary test (present on Chapter 4) showed that cells align to texture direction, it was not possible to properly quantify the surface influence on cell viability. Therefore, further tests should be conducted in a higher number of samples. Furthermore, the geometry and size of the fabricated textures may be varied to achieve an optimized biological response, whether to increase cell adhesion and proliferation, to prevent biofilm formation, or to induce cell differentiation, for instance. Laser sources with different pulse durations can also be tested. DLIP could also be combined with other surface functionalization techniques, such as coating with bioactive materials, to further improve the biological response for biomedical applications.

REFERENCES

ABU RUJA, Mahmood; DE SOUZA, Grace M.; FINER, Yoav. Ultrashort-pulse laser as a surface treatment for bonding between zirconia and resin cement. **Dental Materials**, [*s. l.*], v. 35, n. 11, p. 1545–1556, 2019.

ALAMRI, Sabri; LASAGNI, Andrés Fabián. Development of a general model for direct laser interference patterning of polymers. **Optics Express**, [*s. l.*], v. 25, n. 9, p. 9603–9616, 2017.

ALBREKTSSON, T.; JOHANSSON, C. Osteoinduction, osteoconduction and osseointegration. **European Spine Journal**, [*s. l.*], v. 10, n. 0, p. S96–S101, 2001.

ALGHAZZAWI, Tariq F.; LEMONS, Jack; LIU, Perng-Ru; ESSIG, Milton E.; BARTOLUCCI, Alfred A.; JANOWSKI, Gregg M. Influence of Low-Temperature Environmental Exposure on the Mechanical Properties and Structural Stability of Dental Zirconia. **Journal of Prosthodontics**, [*s. l.*], v. 21, n. 5, p. 363–369, 2012.

AMARANTE, José Eduardo Vasconcellos; SOARES PEREIRA, Marcos Venícius; DE SOUZA, Grace Mendonça; PAIS ALVES, Manuel Fellipe R.; SIMBA, Bruno Galvão; SANTOS, Claudinei dos. Effect of hydrothermal aging on the properties of zirconia with different levels of translucency. **Journal of the Mechanical Behavior of Biomedical Materials**, [*s. l.*], v. 109, p. 103847, 2020.

ARMBRUSTER, Oskar; NAGHILOU, Aida; KAUTEK, Wolfgang. The Role of Defects in Pulsed Laser Matter Interaction. *In*: ADVANCES IN THE APPLICATION OF LASERS IN MATERIALS SCIENCE. Cham: Springer, 2018. v. 274, p. 39–61.

AURÉLIO, Iana L.; MARCHIONATTI, Ana Maria E.; MONTAGNER, Anelise F.; MAY, Liliana G.; SOARES, Fabio Z.M. Does air particle abrasion affect the flexural strength and phase transformation of Y-TZP? A systematic review and meta-analysis. **Dental Materials**, [*s. l.*], v. 32, n. 6, p. 827–845, 2016.

BAN, Seiji; SATO, Hideo; SUEHIRO, Yasuhiko; NAKANISHI, Hideo; NAWA, Masahiro. Biaxial flexure strength and low temperature degradation of Ce-TZP/Al2O3 nanocomposite and Y-TZP as dental restoratives. **Journal of Biomedical Materials Research Part B: Applied Biomaterials**, [*s. l.*], v. 87B, n. 2, p. 492–498, 2008.

BANERJEE, R.; NAG, S.; FRASER, H.L. A novel combinatorial approach to the development of beta titanium alloys for orthopaedic implants. **Materials Science and Engineering: C**, [*s. l.*], v. 25, n. 3, p. 282–289, 2005.

BÄUERLE, Dieter. **Laser Processing and Chemistry**. 4th. ed. Berlin, Heidelberg: Springer Berlin Heidelberg, 2011.

BENZAID, Rajaa; CHEVALIER, Jerome; SAÂDAOUI, Malika; FANTOZZI, Gilbert; NAWA, Masahiro; DIAZ, Luis Antonio; TORRECILLAS, Ramon. Fracture toughness, strength and slow crack growth in a ceria stabilized zirconia–alumina nanocomposite for medical applications. **Biomaterials**, [*s. l.*], v. 29, n. 27, p. 3636–3641, 2008.

BERGER, Jana; ROCH, Teja; PISTILLO, Nicola; LASAGNI, Andrés Fabián. Multiple-beam laser patterning on aluminum oxide, zirconium oxide, and hydroxyapatite ceramic materials using a microlens array. **Journal of Laser Applications**, [*s. l.*], v. 28, n. 4, p. 042003, 2016.

BIGGS, Manus Jonathan Paul; RICHARDS, R. Geoff; DALBY, Matthew J. Nanotopographical modification: a regulator of cellular function through focal adhesions. **Nanomedicine: Nanotechnology, Biology and Medicine**, [*s. l.*], v. 6, n. 5, p. 619–633, 2010.

BISCHOFF, Christian; VÖLKLEIN, Friedemann; SCHMITT, Jana; RÄDEL, Ulrich; UMHOFER, Udo; JÄGER, Erwin; LASAGNI, Andrés Fabián. Design and Manufacturing Method of Fundamental Beam Mode Shaper for Adapted Laser Beam Profile in Laser Material Processing. **Materials**, [*s. l.*], v. 12, n. 14, p. 2254, 2019.

BOHINC, Klemen; DRAŽIĆ, Goran; FINK, Rok; ODER, Martina; JEVŠNIK, Mojca; NIPIČ, Damijan; GODIČ-TORKAR, Karmen; RASPOR, Peter. Available surface dictates microbial adhesion capacity. **International Journal of Adhesion and Adhesives**, [*s. l.*], v. 50, p. 265–272, 2014.

BOLLENL, Curd M.L.; LAMBRECHTS, Paul; QUIRYNEN, Marc. Comparison of surface roughness of oral hard materials to the threshold surface roughness for bacterial plaque retention: A review of the literature. **Dental Materials**, [*s. l.*], v. 13, n. 4, p. 258–269, 1997.

BONA, Alvaro Della; PECHO, Oscar E.; ALESSANDRETTI, Rodrigo. Zirconia as a dental biomaterial. **Materials**, [*s. l.*], v. 8, n. 8, p. 4978–4991, 2015.

BORCHERS, Lothar; STIESCH, Meike; BACH, Friedrich-Wilhelm; BUHL, Josef-Christian; HÜBSCH, Christoph; KELLNER, Tim; KOHORST, Philipp; JENDRAS, Michael. Influence of hydrothermal and mechanical conditions on the strength of zirconia. **Acta Biomaterialia**, [*s. l.*], v. 6, n. 12, p. 4547–4552, 2010.

BOYAN, Barbara D.; DEAN, David D.; LOHMANN, Christoph H.; COCHRAN, David L.; SYLVIA, Victor L.; SCHWARTZ, Zvi. The Titanium-Bone Cell Interface In Vitro: The Role of the Surface in Promoting Osteointegration. *In*: TITANIUM IN MEDICINE. Heidelberg: Springer Berlin, 2001. p. 561–585.

BRÅNEMARK, P.-I.; BREINE, U.; ADELL, R.; HANSSON, B. O.; LINDSTRÖM, J.; OHLSSON, Å. Intra-Osseous Anchorage of Dental Prostheses: I. Experimental Studies. **Scandinavian Journal of Plastic and Reconstructive Surgery**, [*s. l.*], v. 3, n. 2, p. 81–100, 1969.

BROWN, Matthew S; ARNOLD, Craig B. **Laser Precision Microfabrication**. Heidelberg: Springer Berlin Heidelberg, 2010. (Springer Series in Materials Science). v. 135

BUSER, D.; SCHENK, R. K.; STEINEMANN, S.; FIORELLINI, J. P.; FOX, C. H.; STICH, H. Influence of surface characteristics on bone integration of titanium implants. A histomorphometric study in miniature pigs. **Journal of Biomedical Materials Research**, [*s. l.*], v. 25, n. 7, p. 889–902, 1991.

CARVALHO, Angela; GRENHO, Liliana; FERNANDES, Maria H; DASKALOVA, Albena; TRIFONOV, Anton; BUCHVAROV, Ivan; MONTEIRO, Fernando J. Femtosecond laser microstructuring of alumina toughened zirconia for surface functionalization of dental implants. **Ceramics international**, [*s. l.*], v. 46, n. 2, p. 1383–1389, 2020.

CASSIE, A. B. D.; BAXTER, S. Wettability of porous surfaces. **Transactions of the Faraday Society**, [*s. l.*], v. 40, p. 546, 1944.

CHEN, J.; ULERICH, J.P.; ABELEV, E.; FASASI, A.; ARNOLD, C.B.; SOBOYEJO, W.O. An investigation of the initial attachment and orientation of osteoblast-like cells on laser grooved Ti-6Al-4V surfaces. **Materials Science and Engineering: C**, [*s. l.*], v. 29, n. 4, p. 1442–1452, 2009.

CHEVALIER, Jérôme. What future for zirconia as a biomaterial?. **Biomaterials**, [*s. l.*], v. 27, n. 4, p. 535–543, 2006.

CHEVALIER, Jérôme; CALES, Bernard; DROUIN, Jean Michel. Low-Temperature Aging of Y-TZP Ceramics. **Journal of the American Ceramic Society**, [*s. l.*], v. 82, n. 8, p. 2150–2154, 1999.

CHEVALIER, Jérôme; GREMILLARD, Laurent. Zirconia as a Biomaterial ☆. *In*: COMPREHENSIVE BIOMATERIALS II. [*S. l.*]: Elsevier, 2017. v. 1, p. 122–144.

CHEVALIER, Jérôme; GREMILLARD, Laurent; DEVILLE, Sylvain. Low-Temperature Degradation of Zirconia and Implications for Biomedical Implants. **Annual Review of Materials Research**, [*s. l.*], v. 37, n. 1, p. 1–32, 2007.

CHEVALIER, Jérôme; GREMILLARD, Laurent; VIRKAR, Anil V.; CLARKE, David R. The Tetragonal-Monoclinic Transformation in Zirconia: Lessons Learned and Future Trends. **Journal of the American Ceramic Society**, [*s. l.*], v. 92, n. 9, p. 1901–1920, 2009.

CHEVALIER, Jérôme; LIENS, Aléthéa; REVERON, Helen; ZHANG, Fei; REYNAUD, Pascal; DOUILLARD, Thierry; PREISS, Laura; SERGO, Valter; LUGHI, Vanni; SWAIN, Mike; COURTOIS, Nicolas. Forty years after the promise of «ceramic steel?»: Zirconia-based composites with a metal-like mechanical behavior. **Journal of the American Ceramic Society**, [*s. l.*], v. 103, n. 3, p. 1482–1513, 2020.

CHEVALIER, Jérôme; LOH, Joel; GREMILLARD, Laurent; MEILLE, Sylvain; ADOLFSON, Erik. Low-temperature degradation in zirconia with a porous surface. **Acta Biomaterialia**, [*s. l.*], v. 7, n. 7, p. 2986–2993, 2011.

CHEVALIER, Jérôme; OLAGNON, Christian; FANTOZZI, Gilbert. Subcritical Crack Propagation in 3Y-TZP Ceramics: Static and Cyclic Fatigue. **Journal of the American Ceramic Society**, [*s. l.*], v. 82, n. 11, p. 3129–3138, 1999.

CHICHKOV, B. N.; MOMMA, C.; NOLTE, S.; ALVENSLEBEN, F.; TÜNNERMANN, A. Femtosecond, picosecond and nanosecond laser ablation of solids. **Applied Physics A Materials Science & Processing**, [*s. l.*], v. 63, n. 2, p. 109–115, 1996.

CHINTAPALLI, Ravi Kiran; MARRO, Fernando Garcia; JIMENEZ-PIQUE, Emilio; ANGLADA, Marc. Phase transformation and subsurface damage in 3Y-TZP after sandblasting. **Dental Materials**, [*s. l.*], v. 29, n. 5, p. 566–572, 2013.

ĆORIĆ, Danko; MAJIĆ RENJO, Marijana; ĆURKOVIĆ, Lidija. Vickers indentation fracture toughness of Y-TZP dental ceramics. **International Journal of Refractory Metals and Hard Materials**, [*s. l.*], v. 64, p. 14–19, 2017.

CUNHA, Ângela; BARTOLOMEU, Flávio; SILVA, Filipe; TRINDADE, Bruno; CARVALHO, Óscar. Influence of Laser Parameters on the Texturing of 420 Stainless Steel. **Materials**, [*s. l.*], v. 15, n. 24, p. 8979, 2022.

CUNHA, Welson; CARVALHO, Oscar; HENRIQUES, Bruno; SILVA, Filipe S.; ÖZCAN, Mutlu; SOUZA, Júlio C. M. Surface modification of zirconia dental implants by laser texturing. **Lasers in Medical Science**, [*s. l.*], v. 37, n. 1, p. 77–93, 2022.

CUNHA, Alexandre; ELIE, Anne Marie; PLAWINSKI, Laurent; SERRO, Ana Paula; BOTELHO DO REGO, Ana Maria; ALMEIDA, Amélia; URDACI, Maria C.; DURRIEU, Marie Christine; VILAR, Rui. Femtosecond laser surface texturing of titanium as a method to reduce the adhesion of Staphylococcus aureus and biofilm formation. **Applied Surface Science**, [*s. l.*], v. 360, p. 485–493, 2016.

CUNHA, Alexandre; ZOUANI, Omar Farouk; PLAWINSKI, Laurent; BOTELHO DO REGO, Ana Maria; ALMEIDA, Amélia; VILAR, Rui; DURRIEU, Marie-Christine.

Human mesenchymal stem cell behavior on femtosecond laser-textured Ti-6Al-4V surfaces. **Nanomedicine**, [*s. l.*], v. 10, n. 5, p. 725–739, 2015.

CURTIS, Andrew R.; WRIGHT, Adrian J.; FLEMING, Garry J.P. The influence of simulated masticatory loading regimes on the bi-axial flexure strength and reliability of a Y-TZP dental ceramic. **Journal of Dentistry**, [*s. l.*], v. 34, n. 5, p. 317–325, 2006.

DAHOTRE, Narendra B.; HARIMKAR, Sandip P. **Laser Fabrication and Machining of Materials**. 1. ed. Boston, MA: Springer US, 2008.

DANIEL, Claus; ARMSTRONG, Beth L.; HOWE, Jane Y.; DAHOTRE, Narendra B. Controlled evolution of morphology and microstructure in laser interference-structured zirconia. **Journal of the American Ceramic Society**, [*s. l.*], v. 91, n. 7, p. 2138–2142, 2008.

DANIEL, Claus; DRUMMOND, James; GIORDANO, Russell A. Improving flexural strength of dental restorative ceramics using laser interference direct structuring. **Journal of the American Ceramic Society**, [*s. l.*], v. 91, n. 10, p. 3455–3457, 2008.

DE AZA, A. H.; CHEVALIER, J.; FANTOZZI, G.; SCHEHL, M.; TORRECILLAS, R. Crack growth resistance of alumina, zirconia and zirconia toughened alumina ceramics for joint prostheses. **Biomaterials**, [*s. l.*], v. 23, n. 3, p. 937–945, 2002.

DE SOUZA, Raisa Hintz; KAIZER, Marina R.; BORGES, Carolina Elisa Pereira; FERNANDES, Ana Beatriz Franco; CORRER, Gisele Maria; DIÓGENES, Alysson Nunes; ZHANG, Yu; GONZAGA, Carla Castiglia. Flexural strength and crystalline stability of a monolithic translucent zirconia subjected to grinding, polishing and thermal challenges. **Ceramics International**, [*s. l.*], v. 46, n. 16, p. 26168–26175, 2020.

DEALLER, S. F. Electrical phenomena associated with bones and fractures and the therapeutic use of electricity in fracture healing. **Journal of Medical Engineering & Technology**, [*s. l.*], v. 5, n. 2, p. 73–79, 1981.

DEAR, Fraser C.; SHEPHARD, Jonathan D.; WANG, Xin; JONES, Julian D. C.; HAND, Duncan P. Pulsed Laser Micromachining of Yttria-Stabilized Zirconia Dental Ceramic for Manufacturing. **International Journal of Applied Ceramic Technology**, [*s. l.*], v. 5, n. 2, p. 188–197, 2008.

DELGADO-RUÍZ, Rafael Arcesio; ABBOUD, Marcus; ROMANOS, Georgios; AGUILAR-SALVATIERRA, Antonio; GOMEZ-MORENO, Gerardo; CALVO-GUIRADO, Jose Luis. Peri-implant bone organization surrounding zirconia-microgrooved surfaces circularly polarized light and confocal laser scanning microscopy study. **Clinical Oral Implants Research**, [*s. l.*], v. 26, n. 11, p. 1328–1337, 2015.

DELGADO-RUÍZ, Rafael Arcesio; CALVO-GUIRADO, Jose Luis; MORENO, Pablo; GUARDIA, Javier; GOMEZ-MORENO, Gerardo; MATE-SÁNCHEZ, Jose Eduardo; RAMIREZ-FERNÁNDEZ, Piedad; CHIVA, Fernando. Femtosecond laser microstructuring of zirconia dental implants. **Journal of Biomedical Materials Research Part B: Applied Biomaterials**, [*s. l.*], v. 96B, n. 1, p. 91–100, 2011.

DELGADO-RUÍZ, Rafael Arcesio; GOMEZ MORENO, Gerardo; AGUILAR-SALVATIERRA, Antonio; MARKOVIC, Aleksa; MATE-SÁNCHEZ, Jose Eduardo; CALVO-GUIRADO, José Luis. Human fetal osteoblast behavior on zirconia dental implants and zirconia disks with microstructured surfaces. An experimental *in vitro* study. **Clinical Oral Implants Research**, [*s. l.*], v. 27, n. 11, p. e144–e153, 2016.

DEPPRICH, Rita; ZIPPRICH, Holger; OMMERBORN, Michelle; NAUJOKS, Christian; WIESMANN, Hans Peter; KIATTAVORNCHAROEN, Sirichai; LAUER, Hans Christoph; MEYER, Ulrich; KÜBLER, Norbert R.; HANDSCHEL, Jörg. Osseointegration of zirconia implants compared with titanium: An in vivo study. **Head and Face Medicine**, [*s. l.*], v. 4, n. 1, p. 30, 2008.

DI NISO, Francesca; GAUDIUSO, Caterina; SIBILLANO, Teresa; MEZZAPESA, Francesco Paolo; ANCONA, Antonio; LUGARÀ, Pietro Mario. Role of heat accumulation on the incubation effect in multi-shot laser ablation of stainless steel at high repetition rates. **Optics Express**, [*s. l.*], v. 22, n. 10, p. 12200, 2014.

DUMAS, Virginie; RATTNER, Aline; VICO, Laurence; AUDOUARD, Eric; DUMAS, Jean Claude; NAISSON, Pierre; BERTRAND, Philippe. Multiscale grooved titanium processed with femtosecond laser influences mesenchymal stem cell morphology, adhesion, and matrix organization. **Journal of Biomedical Materials Research - Part A**, [*s. l.*], v. 100, n. 11, p. 3108–3016, 2012.

ELIAS, Carlos Nelson; MEIRELLES, Luiz. Improving osseointegration of dental implants. **Expert Review of Medical Devices**, [*s. l.*], v. 7, n. 2, p. 241–256, 2010.

EL-KHOURY, Mikhael; ALAMRI, Sabri; VOISIAT, Bogdan; KUNZE, Tim; LASAGNI, Andrés Fabián. Fabrication of hierarchical surface textures using multi-pulse direct laser interference patterning with nanosecond pulses. **Materials Letters**, [*s. l.*], v. 258, p. 126743, 2020.

EZHILMARAN, V.; VIJAYARAGHAVAN, L.; VASA, N. J.; KRISHNAN, Sivarama. Influence of pulse width in laser assisted texturing on moly-chrome films. **Applied Physics A**, [*s. l.*], v. 124, n. 2, p. 167, 2018.

FABRIS, Douglas; LASAGNI, Andrés Fabián; FREDEL, Márcio C; HENRIQUES, Bruno. Direct Laser Interference Patterning of Bioceramics: A Short Review. **Ceramics**, [*s. l.*], v. 2, n. 4, p. 578–586, 2019.

FARIA, D; MADEIRA, S; BUCIUMEANU, M; SILVA, F S; CARVALHO, O. Novel laser textured surface designs for improved zirconia implants performance. **Materials Science & Engineering C**, [*s. l.*], v. 108, p. 110390, 2020.

FERNANDEZ-YAGUE, Marc A.; ABBAH, Sunny Akogwu; MCNAMARA, Laoise; ZEUGOLIS, Dimitrios I.; PANDIT, Abhay; BIGGS, Manus J. Biomimetic approaches in bone tissue engineering: Integrating biological and physicomechanical strategies. **Advanced Drug Delivery Reviews**, [*s. l.*], v. 84, p. 1–29, 2015.

FUJITA, Satoshi; OHSHIMA, Masahiro; IWATA, Hiroo. Time-lapse observation of cell alignment on nanogrooved patterns. **Journal of The Royal Society Interface**, [*s. l.*], v. 6, n. suppl_3, 2009.

GAHLERT, M.; ROEHLING, S.; SPRECHER, C. M.; KNIHA, H.; MILZ, S.; BORMANN, K. In vivo performance of zirconia and titanium implants: A histomorphometric study in mini pig maxillae. **Clinical Oral Implants Research**, [*s. l.*], v. 23, n. 3, p. 281–286, 2012.

GALLO, Jiri; HOLINKA, Martin; MOUCHA, Calin. Antibacterial Surface Treatment for Orthopaedic Implants. **International Journal of Molecular Sciences**, [*s. l.*], v. 15, n. 8, p. 13849–13880, 2014.

GAO, Chengde; PENG, Shuping; FENG, Pei; SHUAI, Cijun. Bone biomaterials and interactions with stem cells. **Bone Research**, [*s. l.*], v. 5, n. 1, p. 17059, 2017.

GARÓFALO, Stephanie Assimakopoulos; WEHNER, Martin; DOHRN, Andreas; BILANDŽIĆ, Marin Dean; ROOS, Christian; WIERICHS, Richard Johannes; MEYER-LUECKEL, Hendrik; ARANHA, Ana Cecilia Corrêa; ESTEVES-OLIVEIRA, Marcella. Increasing dental zirconia micro-retentive aspect through ultra-short pulsed laser microstructuring: study on flexural strength and crystal phase characterization. **Clinical Oral Investigations**, [*s. l.*], v. 26, n. 1, p. 939–955, 2022.

GARVIE, R. C.; HANNINK, R. H.; PASCOE, R. T. Ceramic steel?. **Nature**, [*s. l.*], v. 258, n. 5537, p. 703–704, 1975.

GIANNUZZI, Giuseppe; GAUDIUSO, Caterina; DI MUNDO, Rosa; MIRENGHI, Luciana; FRAGGELAKIS, Fotis; KLING, Rainer; LUGARÀ, Pietro Mario; ANCONA, Antonio. Short and long term surface chemistry and wetting behaviour of stainless steel with

1D and 2D periodic structures induced by bursts of femtosecond laser pulses. **Applied Surface Science**, [*s. l.*], v. 494, p. 1055–1065, 2019.

GITTENS, Rolando A.; SCHEIDELER, Lutz; RUPP, Frank; HYZY, Sharon L.; GEIS-GERSTORFER, Jürgen; SCHWARTZ, Zvi; BOYAN, Barbara D. A review on the wettability of dental implant surfaces II: Biological and clinical aspects. **Acta Biomaterialia**, [*s. l.*], v. 10, n. 7, p. 2907–2918, 2014.

GOYOS-BALL, Lidia; PRADO, Catuxa; DÍAZ, Raquel; FERNÁNDEZ, Elisa; ISMAILOV, Arnold; KUMPULAINEN, Tero; LEVÄNEN, Erkki; TORRECILLAS, Ramón; FERNÁNDEZ, Adolfo. The effects of laser patterning 10CeTZP-Al2O3 nanocomposite disc surfaces: Osseous differentiation and cellular arrangement in vitro. **Ceramics International**, [*s. l.*], v. 44, n. 8, p. 9472–9478, 2018.

GRATHWOHL, Georg; LIU, Tianshun. Crack Resistance and Fatigue of Transforming Ceramics: II, CeO2 -Stabilized Tetragonal ZrO2. **Journal of the American Ceramic Society**, [*s. l.*], v. 74, n. 12, p. 3028–3034, 1991.

GRIFFITH, L. G. Polymeric biomaterials. **Acta Materialia**, [*s. l.*], v. 48, n. 1, p. 263–277, 2000.

GROESSNER-SCHREIBER, Birte; TUANF, Rocky S. Enhanced extracellular matrix production and mineralization by osteoblasts cultured on titanium surfaces in vitro. **Journal of Cell Science**, [*s. l.*], v. 101, n. Pt 1, p. 209–217, 1992.

GUENTHER, Denise; VALLE, Jaoine; BURGUI, Saioa; GIL, Carmen; SOLANO, Cristina; TOLEDO-ARANA, Alejandro; HELBIG, Ralf; WERNER, Carsten; LASA, Inigo; LASAGNI, Andrés F. Direct laser interference patterning for decreased bacterial attachment. *In*: , 2016. (Udo Klotzbach, Kunihiko Washio, & Craig B. Arnold, Org.)**Laser-based Micro- and Nanoprocessing X**. [*S. l.: s. n.*], 2016. p. 973611.

GÜNTHER, D.; SCHARNWEBER, D.; HESS, R.; WOLF-BRANDSTETTER, C.; HOLTHAUS, M. Grosse; LASAGNI, A. F. High precision patterning of biomaterials using the direct laser interference patterning technology. *In*: LASER SURFACE MODIFICATION OF BIOMATERIALS: TECHNIQUES AND APPLICATIONS. [*S. l.: s. n.*], 2016. p. 3–33.

HALLMANN, Lubica; MEHL, Albert; SERENO, Nuno; HÄMMERLE, Christoph H.F. The improvement of adhesive properties of PEEK through different pre-treatments. **Applied Surface Science**, [*s. l.*], v. 258, n. 18, p. 7213–7218, 2012.

HAN, Jide; MALEK, Olivier; VLEUGELS, Jozef; BRAEM, Annabel; CASTAGNE, Sylvie. Ultrashort pulsed laser ablation of zirconia-alumina composites for implant applications. **Journal of Materials Processing Technology**, [*s. l.*], v. 299, p. 117335, 2022a.

HAN, Jide; SAXENA, Krishna Kumar; BRAEM, Annabel; REYNAERTS, Dominiek; CASTAGNE, Sylvie. Influence of material composition on nanosecond pulsed laser micromachining of zirconia-alumina composites. **Procedia CIRP**, [*s. l.*], v. 113, p. 605–610, 2022b.

HAN, Jide; ZHANG, Fei; VAN MEERBEEK, Bart; VLEUGELS, Jozef; BRAEM, Annabel; CASTAGNE, Sylvie. Laser surface texturing of zirconia-based ceramics for dental applications: A review. **Materials Science & Engineering C**, [*s. l.*], v. 123, p. 112034, 2021.

HAO, L.; LAWRENCE, J. Effects of CO2 laser irradiation on the wettability and human skin fibroblast cell response of magnesia partially stabilised zirconia. **Materials Science and Engineering: C**, [*s. l.*], v. 23, n. 5, p. 627–639, 2003.

HARAI, Tomohiro; MIZUTANI, Masayoshi; SHISHIDO, Shunichi; NAKAMURA, Keisuke; OHMORI, Hitoshi; KONNO, Toyohiko J.; KURIYAGAWA, Tsunemoto. Low-temperature degradation of yttria-stabilized zirconia treated with pulsed laser and annealing techniques. **Precision Engineering**, [*s. l.*], v. 80, p. 45–56, 2023.

HASAN, Jafar; CRAWFORD, Russell J.; IVANOVA, Elena P. Antibacterial surfaces: the quest for a new generation of biomaterials. **Trends in Biotechnology**, [*s. l.*], v. 31, n. 5, p. 295–304, 2013.

HENRIQUES, Bruno; FABRIS, Douglas; MESQUITA-GUIMARÃES, Joana; SOUSA, Anne C.; HAMMES, Nathalia; SOUZA, Júlio C.M.; SILVA, Filipe S.; FREDEL, Márcio C. Influence of laser structuring of PEEK, PEEK-GF30 and PEEK-CF30 surfaces on the shear bond strength to a resin cement. **Journal of the Mechanical Behavior of Biomedical Materials**, [*s. l.*], v. 84, p. 225–234, 2018a.

HENRIQUES, Bruno; FABRIS, Douglas; SOUZA, Júlio C.M.; SILVA, Filipe S.; CARVALHO, Óscar; FREDEL, Márcio C.; MESQUITA-GUIMARÃES, Joana. Bond strength enhancement of zirconia-porcelain interfaces via Nd:YAG laser surface structuring. **Journal of the Mechanical Behavior of Biomedical Materials**, [*s. l.*], v. 81, p. 161–167, 2018b.

HENRIQUES, Bruno; FABRIS, Douglas; TUYAMA, Eduardo; MESQUITA-GUIMARÃES, Joana; SILVA, Filipe S.; SOUZA, Júlio C. M.; FREDEL, Márcio. Shear bond strength of PEEK and PEEK-30GF cemented to zirconia or titanium substrates. **Journal of Adhesion Science and Technology**, [*s. l.*], p. 1–12, 2019.

HENRIQUES, Bruno; FABRIS, Douglas; VOISIAT, Bogdan; BOCCACCINI, Aldo R.; LASAGNI, Andrés Fabián. Direct Laser Interference Patterning of Zirconia Using Infra-Red Picosecond Pulsed Laser: Effect of Laser Processing Parameters on the Surface Topography and Microstructure. **Advanced Functional Materials**, [*s. l.*], 2023a.

HENRIQUES, Bruno; FABRIS, Douglas; VOISIAT, Bogdan; BOCCACCINI, Aldo R.; LASAGNI, Andrés Fabián. Fabrication of functional zirconia surfaces using a two-beam interference setup employing a picosecond laser system with 532-nm wavelength: Morphology, microstructure, and wettability. **Journal of the American Ceramic Society**, [*s. l.*], v. 106, n. 12, p. 7189–7193, 2023b.

HENRIQUES, Bruno; HAMMES, Nathalia; SOUZA, Júlio C.M.; ÖZCAN, Mutlu; MESQUITA-GUIMARÃES, Joana; SILVA, Filipe S.; FREDEL, Márcio C.; VOLPATO, Claudia M.; CARVALHO, Óscar. Influence of ns-Nd:YAG laser surface treatment on the tensile bond strength of zirconia to resin-matrix cements. **Ceramics International**, [*s. l.*], v. 46, n. 17, p. 27822–27831, 2020.

HERRERO-CLIMENT, M.; LÁZARO, P.; VICENTE RIOS, J.; LLUCH, S.; MARQUÉS, M.; GUILLEM-MARTÍ, J.; GIL, F. J. Influence of acid-etching after grit-blasted on osseointegration of titanium dental implants: in vitro and in vivo studies. **Journal of Materials Science: Materials in Medicine**, [*s. l.*], v. 24, n. 8, p. 2047–2055, 2013.

HIROTA, Masatsugu; HARAI, Tomohiro; ISHIBASHI, Shinji; MIZUTANI, Masayoshi; HAYAKAWA, Tohru. Cortical bone response toward nanosecond-pulsed laser-treated zirconia implant surfaces. **Dental Materials Journal**, [*s. l.*], v. 38, n. 3, p. 444–451, 2019.

HOLTHAUS, Marzellus Grosse; TRECCANI, Laura; REZWAN, Kurosch. Comparison of micropatterning methods for ceramic surfaces. **Journal of the European Ceramic Society**, [*s. l.*], v. 31, n. 15, p. 2809–2917, 2011.

HOSTAŠA, Jan; PABST, Willi; MATĚJÍČEK, Jiří. Thermal Conductivity of Al2O3–ZrO2 Composite Ceramics. **Journal of the American Ceramic Society**, [*s. l.*], v. 94, n. 12, p. 4404–4409, 2011.

ISO 6872:2015. Dentistry - ceramic materials. **International Organization for Standadization**, [*s. l.*], 2015.

JAVED, Fawad; ROMANOS, George E. The role of primary stability for successful immediate loading of dental implants. A literature review. **Journal of Dentistry**, [*s. l.*], v. 38, n. 8, p. 612–620, 2010.

JI, Min; XU, Jinyang; CHEN, Ming; EL MANSORI, Mohamed. Enhanced hydrophilicity and tribological behavior of dental zirconia ceramics based on picosecond laser surface texturing. **Ceramics International**, [*s. l.*], v. 46, n. 6, p. 7161–7169, 2020.

JIAO, Yang; BROUSSEAU, Emmanuel; NISHIO AYRE, Wayne; GAIT-CARR, Edward; SHEN, Xiaojun; WANG, Xiaoxiang; BIGOT, Samuel; ZHU, Hanxing; HE, Weifeng.

In vitro cytocompatibility of a Zr-based metallic glass modified by laser surface texturing for potential implant applications. **Applied Surface Science**, [*s. l.*], v. 547, p. 149194, 2021.

JING, Xiubing; PU, Zihao; ZHENG, Shuxian; WANG, Fujun; QI, Huan. Nanosecond laser induced microstructure features and effects thereof on the wettability in zirconia. **Ceramics International**, [*s. l.*], v. 46, n. 15, p. 24173–24182, 2020.

KAROUSSIS, Ioannis K.; SALVI, Giovanni E.; HEITZ-MAYFIELD, Lisa J.A.; BRÄGGER, Urs; HÄMMERLE, Christoph H.F.; LANG, Niklaus P. Long-term implant prognosis in patients with and without a history of chronic periodontitis: A 10-year prospective cohort study of the ITI® Dental Implant System. **Clinical Oral Implants Research**, [*s. l.*], v. 14, n. 3, p. 329–339, 2003.

KARUNAKARAN, Esther; MUKHERJEE, Joy; RAMALINGAM, Bharathi; BIGGS, Catherine A. "Biofilmology": a multidisciplinary review of the study of microbial biofilms. **Applied Microbiology and Biotechnology**, [*s. l.*], v. 90, n. 6, p. 1869–1881, 2011.

KESSLER, Andreas; KAPOR, Svetlana; ERDELT, Kurt; HICKEL, Reinhard; EDELHOFF, Daniel; SYREK, Andreas; GÜTH, Jan-Frederik; KÜHNISCH, Jan. Two-body wear and fracture behaviour of an experimental paediatric composite crown in comparison to zirconia and stainless steel crowns dependent on the cementation mode. **Dental Materials**, [*s. l.*], v. 37, n. 2, p. 264–271, 2021.

KLIGMAN, Stefanie; REN, Zhi; CHUNG, Chun-Hsi; PERILLO, Michael Angelo; CHANG, Yu-Cheng; KOO, Hyun; ZHENG, Zhong; LI, Chenshuang. The Impact of Dental Implant Surface Modifications on Osseointegration and Biofilm Formation. **Journal of clinical medicine**, [*s. l.*], v. 10, n. 8, p. 1641, 2021.

KOHORST, Philipp; BORCHERS, Lothar; STREMPEL, Jürgen; STIESCH, Meike; HASSEL, Thomas; BACH, Friedrich Wilhelm; HÜBSCH, Christoph. Low-temperature degradation of different zirconia ceramics for dental applications. **Acta Biomaterialia**, [*s. l.*], v. 8, n. 3, p. 1213–1220, 2012.

LANG, Valentin; VOISIAT, Bogdan; LASAGNI, Andrés Fabián. High Throughput Direct Laser Interference Patterning of Aluminum for Fabrication of Super Hydrophobic Surfaces. **Materials**, [*s. l.*], v. 12, n. 9, p. 1484, 2019.

LANGHEINRICH, Denise; YSLAS, Edith; BROGLIA, Martín; RIVAROLA, Viviana; ACEVEDO, Diego; LASAGNI, Andrés. Control of cell growth direction by direct fabrication of periodic micro- and submicrometer arrays on polymers. **Journal of Polymer Science, Part B: Polymer Physics**, [*s. l.*], v. 50, n. 6, p. 415–422, 2012.

LASAGNI, Andrés F. Laser interference patterning methods: Possibilities for high-throughput fabrication of periodic surface patterns. **Advanced Optical Technologies**, [*s. l.*], v. 6, n. 3–4, p. 265–275, 2017.

LASAGNI, Andrés F.; GACHOT, Carsten; TRINH, Kim E.; HANS, Michael; ROSENKRANZ, Andreas; ROCH, Teja; ECKHARDT, Sebastian; KUNZE, Tim; BIEDA, Matthias; GÜNTHER, Denise; LANG, Valentin; MÜCKLICH, Frank. Direct laser interference patterning, 20 years of development: from the basics to industrial applications. *In*: , 2017. (Udo Klotzbach, Kunihiko Washio, & Rainer Kling, Org.)**Laser-based Micro- and Nanoprocessing XI**. [*S. l.: s. n.*], 2017. p. 1009211.

LAWSON, Simon. Environmental degradation of zirconia ceramics. **Journal of the European Ceramic Society**, [*s. l.*], v. 15, n. 6, p. 485–502, 1995.

LE GUÉHENNEC, L.; SOUEIDAN, A.; LAYROLLE, P.; AMOURIQ, Y. Surface treatments of titanium dental implants for rapid osseointegration. **Dental Materials**, [*s. l.*], v. 23, n. 7, p. 844–854, 2007.

LI, Jian; JI, Lingfei; HU, Yan; BAO, Yong. Precise micromachining of yttria-tetragonal zirconia polycrystal ceramic using 532 nm nanosecond laser. **Ceramics International**, [*s. l.*], v. 42, n. 3, p. 4377–4385, 2016.

LI, Maoyin; TUNCA, Bensu; VAN MEERBEEK, Bart; VLEUGELS, Jef; ZHANG, Fei. Tough and damage-tolerant monolithic zirconia ceramics with transformation-induced plasticity by grain-boundary segregation. **Journal of the European Ceramic Society**, [*s. l.*], v. 43, n. 5, p. 2078–2092, 2023.

LIM, Jung Yul; DONAHUE, Henry J. Cell Sensing and Response to Micro- and Nanostructured Surfaces Produced by Chemical and Topographic Patterning. **Tissue Engineering**, [*s. l.*], v. 13, n. 8, p. 1879–1891, 2007.

LIU, Qiaomu; HUANG, Shunzhou; HE, Aijie. Composite ceramics thermal barrier coatings of yttria stabilized zirconia for aero-engines. **Journal of Materials Science & Technology**, [*s. l.*], v. 35, n. 12, p. 2814–2823, 2019.

LIU, Mingyue; ZHOU, Jianfeng; YANG, Yang; ZHENG, Miao; YANG, Jianjun; TAN, Jianguo. Surface modification of zirconia with polydopamine to enhance fibroblast response and decrease bacterial activity in vitro: A potential technique for soft tissue engineering applications. **Colloids and Surfaces B: Biointerfaces**, [*s. l.*], v. 136, p. 74–83, 2015.

LORUSSO, Felice; NOUMBISSI, Sammy; FRANCESCO, Inchingolo; RAPONE, Biagio; KHATER, Ahmad G. A.; SCARANO, Antonio. Scientific Trends in Clinical Research on Zirconia Dental Implants: A Bibliometric Review. **Materials**, [*s. l.*], v. 13, n. 23, p. 5534, 2020.

LUGHI, Vanni; SERGO, Valter. Low temperature degradation -aging- of zirconia: A critical review of the relevant aspects in dentistry. **Dental Materials**, [*s. l.*], v. 26, n. 8, p. 807–820, 2010.

LUKASZEWSKA-KUSKA, Magdalena; WIRSTLEIN, Przemysław; MAJCHROWSKI, Radomir; DOROCKA-BOBKOWSKA, Barbara. Osteoblastic cell behaviour on modified titanium surfaces. **Micron**, [*s. l.*], v. 105, p. 55–63, 2018.

MARECI, D.; TRINCĂ, L. C.; CĂILEAN, D.; SOUTO, R. M. Corrosion resistance of ZrTi alloys with hydroxyapatite-zirconia-silver layer in simulated physiological solution containing proteins for biomaterial applications. **Applied Surface Science**, [*s. l.*], v. 389, p. 1069–1075, 2016.

MARTÍNEZ-CALDERON, M.; MANSO-SILVÁN, M.; RODRÍGUEZ, A.; GÓMEZ-ARANZADI, M.; GARCÍA-RUIZ, J. P.; OLAIZOLA, S. M.; MARTÍN-PALMA, R. J. Surface micro- and nano-texturing of stainless steel by femtosecond laser for the control of cell migration. **Scientific Reports**, [*s. l.*], v. 6, n. 1, p. 36296, 2016.

MCBEATH, Rowena; PIRONE, Dana M; NELSON, Celeste M; BHADRIRAJU, Kiran; CHEN, Christopher S. Cell Shape, Cytoskeletal Tension, and RhoA Regulate Stem Cell Lineage Commitment. **Developmental Cell**, [*s. l.*], v. 6, n. 4, p. 483–495, 2004.

MCKITTRICK, J.; CHEN, P.-Y.; TOMBOLATO, L.; NOVITSKAYA, E.E.; TRIM, M.W.; HIRATA, G.A.; OLEVSKY, E.A.; HORSTEMEYER, M.F.; MEYERS, M.A. Energy absorbent natural materials and bioinspired design strategies: A review. **Materials Science and Engineering: C**, [*s. l.*], v. 30, n. 3, p. 331–342, 2010.

MESSOUS, Redouane; HENRIQUES, Bruno; BOUSBAA, Hassan; SILVA, Filipe S.; TEUGHELS, Wim; SOUZA, Júlio C. M. Cytotoxic effects of submicron- and nano-scale titanium debris released from dental implants: an integrative review. **Clinical Oral Investigations**, [*s. l.*], v. 25, n. 4, p. 1627–1640, 2021.

MORALES, M.; GARCÍA-GONZÁLEZ, S.; RIEUX, J.; JIMÉNEZ-PIQUÉ, E. Nanosecond pulsed laser surface modification of yttria doped zirconia for Solid Oxide Fuel Cell applications: Damage and microstructural changes. **Journal of the European Ceramic Society**, [*s. l.*], v. 43, n. 8, p. 3396–3403, 2023.

MOURA, C. G.; PEREIRA, R.; BUCIUMEANU, M.; CARVALHO, O.; BARTOLOMEU, F.; NASCIMENTO, R.; SILVA, F. S. Effect of laser surface texturing on primary stability and surface properties of zirconia implants. **Ceramics International**, [*s. l.*], v. 43, n. 17, p. 15227–15236, 2017.

MULKO, Lucinda; SOLDERA, Marcos; LASAGNI, Andrés Fabián. Structuring and functionalization of non-metallic materials using direct laser interference patterning: a review. **Nanophotonics**, [*s. l.*], v. 11, n. 2, p. 203–240, 2022.

MÜLLER, Daniel Wyn; FOX, Tobias; GRÜTZMACHER, Philipp G.; SUAREZ, Sebastian; MÜCKLICH, Frank. Applying Ultrashort Pulsed Direct Laser Interference Patterning for Functional Surfaces. **Scientific Reports**, [*s. l.*], v. 10, n. 1, p. 3647, 2020.

MUÑOZ-TABARES, J.A.; JIMÉNEZ-PIQUÉ, E.; REYES-GASGA, J.; ANGLADA, M. Microstructural changes in ground 3Y-TZP and their effect on mechanical properties. **Acta Materialia**, [*s. l.*], v. 59, n. 17, p. 6670–6683, 2011.

NASCIMENTO, Cássio do; PITA, Murillo Sucena; FERNANDES, Flávio Henrique Nogueira Carriço; PEDRAZZI, Vinícius; DE ALBUQUERQUE JUNIOR, Rubens Ferreira; RIBEIRO, Ricardo Faria. Bacterial adhesion on the titanium and zirconia abutment surfaces. **Clinical Oral Implants Research**, [*s. l.*], v. 25, n. 3, p. 337–343, 2014.

NGUYEN, Lonnissa H; ANNABI, Nasim; NIKKHAH, Mehdi; BAE, Hojae; BINAN, Loïc; PARK, Sangwon; KANG, Yunqing; YANG, Yunzhi; KHADEMHOSSEINI, Ali. Vascularized bone tissue engineering: approaches for potential improvement. **Tissue engineering. Part B, Reviews**, [*s. l.*], v. 18, n. 5, p. 363–82, 2012.

NODA, Makoto; OKUDA, Yuji; TSURUKI, Jiro; MINESAKI, Yoshito; TAKENOUCHI, Yasumi; BAN, Seiji. Surface damages of zirconia by Nd:YAG dental laser irradiation. **Dental Materials Journal**, [*s. l.*], v. 29, n. 5, p. 536–541, 2010.

OHTSU, Naofumi; KOZUKA, Taro; HIRANO, Mitsuhiro; ARAI, Hirofumi. Electrolyte effects on the surface chemistry and cellular response of anodized titanium. **Applied Surface Science**, [*s. l.*], v. 349, p. 911–915, 2015.

PALMERO, Paola; FORNABAIO, Marta; MONTANARO, Laura; REVERON, Helen; ESNOUF, Claude; CHEVALIER, Jérôme. Towards long lasting zirconia-based composites for dental implants. Part I: Innovative synthesis, microstructural characterization and in vitro stability. **Biomaterials**, [*s. l.*], v. 50, p. 38–46, 2015.

PALMQUIST, Anders; LINDBERG, Fredrik; EMANUELSSON, Lena; BRÅNEMARK, Rickard; ENGQVIST, Håkan; THOMSEN, Peter. Biomechanical, histological, and ultrastructural analyses of laser micro- and nano-structured titanium alloy implants: A study in rabbit. **Journal of Biomedical Materials Research - Part A**, [*s. l.*], v. 92, n. 4, p. 1476–1486, 2010.

PARDUN, Karoline; TRECCANI, Laura; VOLKMANN, Eike; STRECKBEIN, Philipp; HEISS, Christian; GERLACH, Juergen W.; MAENDL, Stephan; REZWAN, Kurosch. Magnesium-containing mixed coatings on zirconia for dental implants: Mechanical characterization and in vitro behavior. **Journal of Biomaterials Applications**, [*s. l.*], v. 30, n. 1, p. 104–118, 2015.

PARK, J.; LAKES, R. **Biomaterials**. 3rd. ed. New York, NY: Springer New York, 2007.

PARRY, Jonathan P.; SHEPHARD, Jonathan D.; DEAR, Fraser C.; JONES, Nick; WESTON, Nick; HAND, Duncan P. Nanosecond-Laser Postprocessing of Millisecond- Laser-Machined Zirconia (Y-TZP) Surfaces. **International Journal of Applied Ceramic Technology**, [*s. l.*], v. 5, n. 3, p. 249–257, 2008.

PARRY, Jonathan P.; SHEPHARD, Jonathan D.; HAND, Duncan P.; MOORHOUSE, Colin; JONES, Nick; WESTON, Nick. Laser Micromachining of Zirconia (Y-TZP) Ceramics in the Picosecond Regime and the Impact on Material Strength. **International Journal of Applied Ceramic Technology**, [*s. l.*], v. 8, n. 1, p. 163–171, 2011.

PARVEEZ, Bisma; WANI, M.F. Tribological behaviour of nano-zirconia reinforced iron-based self-lubricating composites for bearing applications. **Tribology International**, [*s. l.*], v. 159, p. 106969, 2021.

PEREIRA, R.S.F.; MOURA, C.G.; HENRIQUES, B.; CHEVALIER, J.; SILVA, F.S.; FREDEL, M.C. Influence of laser texturing on surface features, mechanical properties and low-temperature degradation behavior of 3Y-TZP. **Ceramics International**, [*s. l.*], v. 46, n. 3, p. 3502–3512, 2020.

PICONI, C.; MACCAURO, G. Zirconia as a ceramic biomaterial. **Biomaterials**, [*s. l.*], v. 20, n. 1, p. 1–25, 1999.

PITTAYACHAWAN, Piyapanna; MCDONALD, Ailbhe; PETRIE, Aviva; KNOWLES, Jonathan C. The biaxial flexural strength and fatigue property of Lava^{TM} Y-TZP dental ceramic. **Dental Materials**, [*s. l.*], v. 23, n. 8, p. 1018–1029, 2007.

POPRAWE, Reinhart (org.). **Tailored Light 2**. Berlin, Heidelberg: Springer Berlin Heidelberg, 2011. (RWTHedition).

PU, Zihao; JING, Xiubing; YANG, Chengjuan; WANG, Fujun; EHMANN, Kornel F. Wettability modification of zirconia by laser surface texturing and silanization. **International Journal of Applied Ceramic Technology**, [*s. l.*], v. 17, n. 5, p. 2182–2192, 2020.

QUINN, James; MCFADDEN, Ryan; CHAN, Chi-Wai; CARSON, Louise. Titanium for Orthopedic Applications: An Overview of Surface Modification to Improve

Biocompatibility and Prevent Bacterial Biofilm Formation. **iScience**, [*s. l.*], v. 23, n. 11, p. 101745, 2020.

RAUCHS, G; FETT, T; MUNZ, D; OBERACKER, R. Tetragonal-to-monoclinic phase transformation in CeO2-stabilised zirconia under uniaxial loading. **Journal of the European Ceramic Society**, [*s. l.*], v. 21, n. 12, p. 2229–2241, 2001.

REVERON, Helen; FORNABAIO, Marta; PALMERO, Paola; FÜRDERER, Tobias; ADOLFSSON, Erik; LUGHI, Vanni; BONIFACIO, Alois; SERGO, Valter; MONTANARO, Laura; CHEVALIER, Jérôme. Towards long lasting zirconia-based composites for dental implants: Transformation induced plasticity and its consequence on ceramic reliability. **Acta Biomaterialia**, [*s. l.*], v. 48, p. 423–432, 2017.

ROITERO, E; ANGLADA, M; MÜCKLICH, F; JIMÉNEZ-PIQUÉ, E. Mechanical reliability of dental grade zirconia after laser patterning. **Journal of the Mechanical Behavior of Biomedical Materials**, [*s. l.*], v. 86, p. 257–263, 2018a.

ROITERO, E; LASSERRE, F; ANGLADA, M; MÜCKLICH, F; JIMÉNEZ-PIQUÉ, E. A parametric study of laser interference surface patterning of dental zirconia: Effects of laser parameters on topography and surface quality. **Dental Materials**, [*s. l.*], v. 33, n. 1, p. e28–e38, 2017a.

ROITERO, E; LASSERRE, F; ROA, J.J; ANGLADA, M; MÜCKLICH, F; JIMÉNEZ-PIQUÉ, E. Nanosecond-laser patterning of 3Y-TZP: Damage and microstructural changes. **Journal of the European Ceramic Society**, [*s. l.*], v. 37, n. 15, p. 4876–4887, 2017b.

ROITERO, E; OCHOA, M; ANGLADA, M; MÜCKLICH, F; JIMÉNEZ-PIQUÉ, E. Low temperature degradation of laser patterned 3Y-TZP: Enhancement of resistance after thermal treatment. **Journal of the European Ceramic Society**, [*s. l.*], v. 38, n. 4, p. 1742–1749, 2018b.

SALMINEN, Turkka; HAHTALA, Mikko; SEPPÄLÄ, Ilkka; LAUKKANEN, Pekka; NIEMI, Tapio. Picosecond pulse laser ablation of yttria-stabilized zirconia from kilohertz to megahertz repetition rates. **Applied Physics A**, [*s. l.*], v. 101, n. 4, p. 735–738, 2010.

SAMANT, Anoop N.; DAHOTRE, Narendra B. Laser machining of structural ceramics—A review. **Journal of the European Ceramic Society**, [*s. l.*], v. 29, n. 6, p. 969–993, 2009.

SCHÜNEMANN, Fernanda H.; GALÁRRAGA-VINUEZA, María E.; MAGINI, Ricardo; FREDEL, Márcio; SILVA, Filipe; SOUZA, Júlio C.M.; ZHANG, Yu; HENRIQUES, Bruno. Zirconia surface modifications for implant dentistry. **Materials Science and Engineering C**, [*s. l.*], v. 98, p. 1294–1305, 2019.

SHAH, Furqan A.; THOMSEN, Peter; PALMQUIST, Anders. Osseointegration and current interpretations of the bone-implant interface. **Acta Biomaterialia**, [*s. l.*], v. 84, p. 1–15, 2019.

SINHAMAHAPATRA, Apurba; JEON, Jong-Pil; KANG, Joonhee; HAN, Byungchan; YU, Jong-Sung. Oxygen-Deficient Zirconia (ZrO2−x): A New Material for Solar Light Absorption. **Scientific Reports**, [*s. l.*], v. 6, n. 1, p. 27218, 2016.

SMITH, D C. Dental implants: materials and design considerations. **Int J Prosthodont**, [*s. l.*], v. 6, n. 2, p. 106–117, 1993.

SOON, Ginny; PINGGUAN-MURPHY, Belinda; LAI, Khin Wee; AKBAR, Sheikh Ali. Review of zirconia-based bioceramic: Surface modification and cellular response. **Ceramics International**, [*s. l.*], v. 42, n. 11, p. 12543–12555, 2016.

STADLINGER, B.; HENNIG, M.; ECKELT, U.; KUHLISCH, E.; MAI, R. Comparison of zirconia and titanium implants after a short healing period. A pilot study in minipigs. **International Journal of Oral and Maxillofacial Surgery**, [*s. l.*], v. 39, n. 6, p. 585–592, 2010.

STAIGER, Mark P.; PIETAK, Alexis M.; HUADMAI, Jerawala; DIAS, George. Magnesium and its alloys as orthopedic biomaterials: A review. **Biomaterials**, [*s. l.*], v. 27, n. 9, p. 1728–1734, 2006.

STARK, Tobias; ALAMRI, Sabri; AGUILAR-MORALES, Alfredo I.; KIEDROWSKI, Thomas; LASAGNI, Andrés Fabián. Positive Effect of Laser Structured Surfaces on Tribological Performance. **Journal of Laser Micro/Nanoengineering**, [*s. l.*], v. 14, n. 1, p. 13–18, 2019.

STUDART, André R.; FILSER, Frank; KOCHER, Peter; GAUCKLER, Ludwig J. Fatigue of zirconia under cyclic loading in water and its implications for the design of dental bridges. **Dental Materials**, [*s. l.*], v. 23, n. 1, p. 106–114, 2007.

SWAMI, Vasanthi; VIJAYARAGHAVAN, Vasantha; SWAMI, Vinit. Current trends to measure implant stability. **The Journal of Indian Prosthodontic Society**, [*s. l.*], v. 16, n. 2, p. 124, 2016.

THORSTENSEN, Jostein; ERIK FOSS, Sean. Temperature dependent ablation threshold in silicon using ultrashort laser pulses. **Journal of Applied Physics**, [*s. l.*], v. 112, n. 10, p. 103514, 2012.

TORAYA, Hideo; YOSHIMURA, Masahiro; SOMIYA, Shigeyuki. Calibration Curve for Quantitative Analysis of the Monoclinic-Tetragonal ZrO2 System by X-Ray

Diffraction. **Journal of the American Ceramic Society**, [*s. l.*], v. 67, n. 6, p. C-119-C–121, 1984.

VALLE, Jaione; BURGUI, Saioa; LANGHEINRICH, Denise; GIL, Carmen; SOLANO, Cristina; TOLEDO-ARANA, Alejandro; HELBIG, Ralf; LASAGNI, Andrés; LASA, Iñigo. Evaluation of Surface Microtopography Engineered by Direct Laser Interference for Bacterial Anti-Biofouling. **Macromolecular Bioscience**, [*s. l.*], v. 15, n. 8, p. 1060–1069, 2015.

WANG, Zhejun; SHEN, Ya; HAAPASALO, Markus. Dental materials with antibiofilm properties. **Dental Materials**, [*s. l.*], v. 30, n. 2, p. e1–e16, 2014.

WANG, Xin; SHEPHARD, Jonathan D.; DEAR, Fraser C.; HAND, Duncan P. Optimized Nanosecond Pulsed Laser Micromachining of Y-TZP Ceramics. **Journal of the American Ceramic Society**, [*s. l.*], v. 91, n. 2, p. 391–397, 2008.

WEBSTER, Thomas J. Nano rough micron patterned titanium for directing osteoblast morphology and adhesion. **International Journal of Nanomedicine**, [*s. l.*], p. 229, 2008.

WEI, Chong; GREMILLARD, Laurent. Surface treatment methods for mitigation of hydrothermal ageing of zirconia. **Journal of the European Ceramic Society**, [*s. l.*], v. 39, n. 14, p. 4322–4329, 2019.

WEI, Chong; GREMILLARD, Laurent. The influence of stresses on ageing kinetics of 3Y- and 4Y- stabilized zirconia. **Journal of the European Ceramic Society**, [*s. l.*], v. 38, n. 2, p. 753–760, 2018.

WENZEL, Robert N. Resistance of Solid Surfaces to Wetting by Water. **Industrial & Engineering Chemistry**, [*s. l.*], v. 28, n. 8, p. 988–994, 1936.

WROBLEWSKI, Michael; SINEY, Paul D.; NAGAI, Hagime; FLEMING, Patricia A. Wear of ultra-high-molecular-weight polyethylene cup articulating with 22.225 mm zirconia diameter head in cemented total hip arthroplasty. **Journal of Orthopaedic Science**, [*s. l.*], v. 9, n. 3, p. 253–255, 2004.

YIN, Ling; NAKANISHI, Yoshitaka; ALAO, Abdur-Rasheed; SONG, Xiao-Fei; ABDUO, Jaafar; ZHANG, Yu. A Review of Engineered Zirconia Surfaces in Biomedical Applications. **Procedia CIRP**, [*s. l.*], v. 65, p. 284–290, 2017.

ZHANG, Yu. Overview: Damage resistance of graded ceramic restorative materials. **Journal of the European Ceramic Society**, [*s. l.*], v. 32, n. 11, p. 2623–2632, 2012.

ZHANG, Y.; LAWN, B.R. Novel Zirconia Materials in Dentistry. **Journal of Dental Research**, [*s. l.*], v. 97, n. 2, p. 140–147, 2018.

ZHOU, Hongbo; LI, Chen; ZHOU, Zhenkai; CAO, Ruoyan; CHEN, Yu; ZHANG, Shuseng; WANG, Gang; XIAO, Si; LI, Zhuan; XIAO, Peng. Femtosecond laser-induced periodic surface microstructure on dental zirconia ceramic. **Materials Letters**, [*s. l.*], v. 229, p. 74–77, 2018.

ZWAHR, Christoph; GÜNTHER, Denise; BRINKMANN, Tina; GULOW, Nikolai; OSWALD, Steffen; GROSSE HOLTHAUS, Marzellus; LASAGNI, Andrés Fabián. Laser Surface Pattering of Titanium for Improving the Biological Performance of Dental Implants. **Advanced Healthcare Materials**, [*s. l.*], v. 6, n. 3, p. 1600858, 2017.